Spin-mechanics with micro-particle levitating in a Paul trap

Tom Delord

PSL UNIVERSITÉ PARIS

THÈSE DE DOCTORAT
DE L'UNIVERSITÉ PSL

Préparée à l'ENS Paris

Spin-mechanics with micro-particles levitating in a Paul trap

Soutenue par
Tom Delord
Le 01 Octobre 2019

École doctorale n°564
EDPIF

Spécialité
Quantum physics, Condensed matter, Optics

Composition du jury :

Jean-François ROCH Professeur, Laboratoire Aimé Cotton	*Président*
Markus ARNDT Professor, University of Vienna. Faculty of Physics	*Rapporteur*
Tracy NORTHUP Professor, Institute for Experimental Physics, University of Innsbruck	*Rapporteur*
Samuel DELÉGLISE Chargé de recherche, Laboratoire Kastler Brossel	*Examinateur*
Alexandre TALLAIRE Chargé de recherche, Chimie Paris Tech	*Examinateur*
Gabriel HÉTET Maître de conférence, École Normale Supérieure	*Directeur de thèse*

ENS ÉCOLE NORMALE SUPÉRIEURE | PSL

À ma famille, à mes amis,

"A chaque chose, sa loi: l'éternel diamant doit être sans tache, la création momentanée [...] a le droit d'être légère, bizarre."
Honoré de Balzac

Contents

Acknowledgements

C'est un peu une page de ma vie qui se tourne alors que ce manuscrit s'achève. En dépit de tout ce que la tâche d'un thésard peut comporter de solitaire, c'est aussi surtout un travail qui repose sur les autres, à travers des articles ou thèses, des colloques ou des discussions en salle de manip, au détour d'un couloir ou autour d'un repas. J'ai pu au cours de ma thèse cotoyer nombre de gens admirables, collaborateurs, collègues, amis que j'ai rencontrés ou de longue date, qui m'ont apporté idées, conseils, sagesse ou qui m'ont simplement supporté. Avant de présenter les travaux que j'ai réalisés durant ma thèse, j'aimerais donc leur dire un grand merci.

Tout d'abord, j'aimerai remercier le ministère de l'enseignement supérieur et de la recherche ainsi que l'ENS de Lyon qui m'ont attribué le financement qui m'a permis de réaliser ma thèse. Je souhaite également remercier la direction de l'ENS et plus particulèrement celle du département de physique et de son laboratoire de physique, Jean-Marc Berroir et Jérome Tignon, pour l'excellent cadre que procure l'ENS pour un jeune doctorant.

Parmi toute les personnes avec lesquelles j'ai travaillé et collaborer, je souhaite avant tout remercier mon directeur de thèse Gabriél Hétet. J'ai pris l'habitude de conseiller aux aspirant doctorants de choisir leur équipe et non leur sujet de thèse, c'est ce que j'ai fait en sortant de mon master. J'ai rejoint un projet expérimental qui débutait à peine, mais sans jamais craindre impasses, hésitations ou atermoiement, et cela en grande partie du fait de l'audace et de l'intrépidité que je donne volontier à mon directeur de thèse. Cette confiance de m'a pas déçu, et j'ai également pu profiter lors de ma thèse du fort investissement et des qualités d'expérimentateur de mon directeur de thèse. Pour tout cela, mais aussi pour tout le temps que nous avons partagé, au début "tous seuls", pour la confiance que tu m'as donnée, je t'adresse un très grand MERCI Gabriel !

Mes remerciements vont églament à Paul Huillery, avec lequel j'ai travaillé un peu en tandem lors des deux dernières années de ma thèse. La relation entre un "vieux" thésard et un nouveau postdoc est nécessairement assymétrique, je pense que dans notre cas, Gabriel, toi et moi, nous nous sommes très bien complétés les uns les autres. Nous avons pu compter sur toi, sur ton investissement, sur ton nouveau regard et sur ta capacité à réaliser ce qui nous manquait, parfois sans que nous nous en soyons aperçu ! Je sais que tu n'en doutes pas, mais tu as été un élément clef de l'équipe durant ces deux dernières années et ce fut un plaisir de travailler avec toi.

Je remercie aussi Louis Nicolas, mon "frère de thèse", qui a travaillé sur le projet initial de Gabriel. Même si nos sujets respectifs ne se sont pas toujours prêtés à une forte

collaboration, nous avons partagé bien plus qu'un directeur de thèse ! Merci pour la bonne ambiance en salle de manip et aux labos, pour les bons conseils, les discussions qui aident et pour toutes tes phrases à l'emporte-pièce qui me manqueront !

J'aimerai remercier toute l'équipe d'optique du LPENS, les permanents et chefs, Cristophe Voisin, Yannick Chassagneux, Emmanuel et Phillipe pour leur accueil et leur aide ainsi que tout les thésards, Théo, Christophe, Adrien, Raphaël, Hadrien, Romaric et Antoine qui ont partagé ma vie du labo, toujours dans la bonne humeur et le soutien.
J'ai également eu la chance de collaborer avec des chercheurs remarquables, dont la confiance et l'enthousiasme furent importants pour moi au début de ma thèse. Merci à Vincent et Alexandre notamment.

Je souhaite exprimer ma gratitude envers ma famille et mes proches, pour le soutien et la chaleur qu'ils mont apportés. Je remercie mes parents Yann et Brigitte pour tout ce qu'ils m'ont donné, mes grands parents, notamment pour leur énorme soutien pour mes études. Je remercie mon frère, qui a peut être été le premier, tout jeune, à me faire aimer les maths -rien que ça ! Ma reconnaissance va aussi à Nadia et à ma famille de Paris, mes tantes et mes cousins pour leur accueil et leur soutien. J'ai également été heureux de rencontrer certains de mes plus proches amis lors de ma thèse, merci à Melissa, Julia et Adam pour tout ce qu'ils ont pu m'offrir. Enfin, merci à tout mes amis, proches où lointain, Simon, la bande d'Avignon, de fauchage collectif pour avoir illuminé mes we, mes nuits et mes soirées.

Je remercie les personnels administratifs et techniques du laboratoire, Christine, Didier, Célia, Anne, Catherine qui, à défaut de nous rendre la vie facile nous la rendre plus facile, ce qui n'est pas peu ! Je suis également fort reconnaissant au docteur Aparicio et au professeur Ea des service généraliste et rhumatologie de l'hôpital Lariboisière pour leur sollicitude et leur bienveillance. Leur diagnostique rapide d'une affection qui m'a touché en début de thèse m'a probablement épargné bien plus de souffrances à un moment charnière professionellement.

J'adresse également un grand merci aux personnes qui ont pu me soutenir lors de mes premiers débuts dans le monde de la recherche, qui m'ont beaucoup appris ou inspiré. Un merci particulier à Sébastien et Florian.

Pour finir, je remercie les membres de mon jury de thèse Marcus Arndt, Tracy Northup, Jean-François Roch, Samuel Deléglise et Alexandre Tallaire pour avoir accepté d'évaluer mon travail de thèse. Je suis particulièrement reconnaissant à mes deux rapporteurs Marcus Arndt et Tracy Northup qui ont pris le temps de relire mon manuscrit et fait le déplacement pour ma soutenance.

Introduction

The theory of quantum mechanics was developed to explain a number of inconsistencies that could not be explained by classical mechanics [1–3]. It predicts certain phenomena which are highly counter-intuitive and remained largely controversial for decades, especially since they could not be demonstrated experimentally [4]. With the introduction of appropriate tools like the laser [5], experiments to test these predictions were eventually designed [6]. Such experiments were realized using cascades of single atoms interacting with light [7, 8] and corroborated the theory of quantum mechanics.

In the mean time, the development of ion traps [9] made it possible to confine a single ion in space and study its interaction with light. The quantized motion of a single trapped ion can indeed be controled with a laser using sideband cooling [10], to eventually cool it down to its ground state [11]. Subsequently, laser cooling of neutral atoms was also achieved [12], following the development of magneto-optical traps. These new systems provided a new route to probe the singularities of quantum mechanics. In particular its laws can be used to devise algorithms faster than any classical analog [13]. Trapped ions provide a means to implement these algorithms by building a quantum computer [14]. Such device would here rely on coupling the ion's internal degree of freedom, *eg* its spin, to its quantized motion [15]. For now, these protocols have allowed coupling up to 14 ions together [16].
These protocols can actually be implemented more broadly in any network of two level systems that can be coupled to each other. In particular, a number of systems in the solid-state are now able to perform these protocols with varying efficiency: a non exhaustive list includes impurities in silicon [17] and diamond [18–20], superconducting circuits [21, 22], quantum dots [23] or nuclear spins in molecules [24].

Notwithstanding the progress of these "quantum technologies", a salient issue in our understandings of quantum mechanics is the transition towards classical mechanics for macroscopic objects. The quantum nature of massive particle like electrons was demonstrated early on by matter-wave interferometry experiments [25]. Over time, similar demonstrations were performed with free-falling molecules of increasing sizes [26, 27].
However, the advances in the field of trapped ions provide a new way to probe large objects in the quantum regime: one can envision similar experiments, where the motion of a massive mechanical oscillator is cooled down to its ground state *via* side-band cooling and then prepared in an arbitrary quantum state. This device could be used as a resource for quantum computing, playing the role of a transducer [28–30] or test the boudaries of quantum mechanics [31, 32].
The observation of the effect of light on large mechanical oscillators in fact preceeded laser cooling of trapped ions: in interferometers or cavities, radiation pressure exert a force on

the mirrors and can cool their motion [33]. When this opto-mechanical coupling is strong enough, one can achieve sideband cooling of the mirror's motion to its ground state and from there prepare any arbitrary state [34].
Realizing such experiment with large object is however challenging because the optomechanical coupling is small compared to the lifetime of the mechanical oscillator and of the optical cavity.
To leverage these limitations, there has been a trend to reduce the size of the oscillator to the micron-scale. The mirrors can also be replaced by a photonic structure [35, 36] and one can use low-loss microwave cavities [37, 38].

An alternative scheme is to couple the mechanical oscillator not to light, but to a two level system exhibiting high coherence properties and coherent control. Examples include coupling between a mechanical oscillator and trapped atoms [39] or solid-state systems like a superconducting circuit [40] or the spin of an impurity in a semi-conductor [41]. Most of these systems require a cryogenic environment in order to retain high coherence and lifetime for both the two level system and the mechanical oscillator. In this regard, the electron spin of the nitrogen vacancy (NV) center in diamond is an attractive system, with a long coherence time even at room temperature [18]. Several schemes to couple an NV spin to a mechanical oscillator are beeing pursued [42]. In particular, one can perform a magnetic coupling of the spin to the tip of a nearby mechanical oscillator [43–45]. However, the cooling of a mechanical oscillator using a single NV spin has for now been elusive: for example, in the case of magnetic coupling, a sufficient coupling requires magnetic gradients that are challenging to attain.

Finally, the most direct route to suppress heating of the mechanical oscillator at room temperature is to levitate the mechanical oscillator under high vacuum [46]. Levitation of nano or micro-particles can be carried out with an optical tweezer [47], a Paul trap [48] or a magneto-gravitational trap [49].
The motion of the levitating particle can then be addressed optically by positioning it in a high finesse cavity [50]. One can also apply a feed-back loop to cool down the motion through modulation of the trapping potential itself [51, 52] or by applying an external optical [49, 53] or electric force [54, 55]. A nanosphere levitating in an optical tweezer was recently cooled down to a mean phonon number of 4 and the signature of its quantized motion was clearly observed [56].

These successes have sparked a keen interest in levitating a particle with an internal quantum degree of freedom coupled to its motion. A nano-diamond with a single embedded NV spin is a natural candidate for these experiments. Similarly to what was proposed with a cantilever [43], magnetic coupling between the center of mass of the particle and its spin can be used to realize matter-wave interferometry experiments [57–60], to cool down the diamond's motion [61], to generate arbitrary quantum superposition of its motional state [58] or to interface two NV spins [60].
Nano-diamonds have been levitated in optical tweezers [62–64], in Paul traps [52, 65] or in magneto-Gravitational traps [49]. The main challenge of these experiment is to achieve a high enough single spin coupling, which means generating a magnetic gradient in the order of 10^7 T/m [43] without disrupting the levitated particle. The use of optical tweezers to levitate the diamond is also hampered by the absorption of the trapping beam by the diamond, leading to an increased internal temperature [64, 66, 67].

In this work, we levitate larger diamonds with many embedded NV spins ($\sim 10^4$-10^9) in a Paul trap. The use of a scattering free trap allows us to avoid the strong heating observed with optical tweezers. Further, to leverage the issue of the low single-spin coupling, we turn towards the angular degrees of freedom, which is under increasing scrutiny in levitation experiments [68–72], and more precisely towards libration (angular oscillation) of the levitated particle. In fact, a homogeneous magnetic field allows us to observe a coupling between the librational modes (angular oscillations) of a levitated micro-diamond and an ensemble of embedded NV spins.

In the first chapter we will introduce the field of spin-mechanics: the coupling between a spin and a mechanical oscillator. We will first describe the spin degree of freedom and how it can be studied. We then show how a spin can be coupled to a mechanical oscillator in the case of a single ion in a Paul trap. We finally present systems proposed to achieve a similar coupling with a macroscopic oscillator.

The second chapter focuses on our levitation apparatus, which defines the mechanical oscillator of our experiments. We first study the Paul trap theoretically: we show that for non-isotropic particles it confines not only the center of mass, but also its angular degrees of freedom [73] . We then describe its experimental implementation: first the levitation set-up [74, 75], the detection of the mechanical modes [76, 77] and then its limitations.

In order to take advantage of the NV centers embedded in our levitating diamond, we must combine our trapping scheme with the tools used to control NV spins [74, 75]. In the third chapter, we first recall the basics of these tools before describing the combined trap-spin set-up. We then use NV spins control to monitor the angular stability of a levitating diamond and to show the spins properties are unaffected by the Paul trap.

In this fourth chapter, we use large spins ensemble which results in the observation of a magnetic spin-induced torque applied to a levitating micro-diamond [77]. Further, we detect a back-action of the NV spins unto the motion of the micro-diamond, similar to what has been observed in optomechanics with photons. Thanks to the long lifetime of the NV spins we use this back-action to cool down the motion of a levitating diamond under moderate vacuum. Finally, we give a theoretical description of this spin-mechanical coupling in the quantum regime [73]. In our system, the low frequency ($\sim$ kHz) of the mechanical oscillator and the low coherence time of the NV spins ($\sim$µs) are the main limitations to enter this regime.

In the last chapter, we introduce ferromagnetic particles in our levitation experiment [76]. We first describe theoretically how magnetic forces can indeed be used to substantially enhance the frequency of a micron-scale levitating oscillator. We then present first experiments showing the oscillation of levitating iron-rods at frequencies up to 150 kHz. Finally, hybrid particles composed of both diamond and ferromagnetic parts are levitated. These particles have the potential to reach high mechanical frequencies while NV spins can be used to cool down and control their motion.

Chapter 1

Basics of spin-mechanics

The spin is a magnetic and mechanical property inherent to some elementary particles like *eg* the electron. It gives rise to an intrinsic magnetic moment and angular momentum similar to the orbital spin and angular momentum that is generated by the motion of a charged particle. In this introductory chapter, we will first focus on detection of the spin, starting from its discovery to more refined detection schemes. We will then introduce how it can be coupled to a mechanical oscillator to control its motion in the case of trapped ions. We will finally describe the coupling schemes that have been developed for spin-mechanics with NV spins.

1.1 Spin detection

Intriguingly, the existence and the quantum nature of the spin was first demonstrated by the displacement of a mechanical object. The presence of an intrinsic electron spin was first evidenced in 1915 by the Einstein de Haas [78] and the Barnett effects [79]. Both these experiments make use of the angular momentum associated with the electron spin and the angular momentum conservation: when a piece of solid is magnetized, it slowly rotates to compensate the change of angular momentum of the electrons even though no torque is applied to the object.

In this work we focus on the coupling of the spin to mechanical motion through its magnetic moment under magnetic fields or magnetic gradients. The magnetic moment μ_s of an electron spin is often described using the gyromagnetic ratio of the electron γ_e: $\mu_s = \gamma_e \vec{S}$, where $\vec{S}$ is the spin of the electron.

1.1.1 The Stern-Gerlach experiment

The quantum nature of the spin is most striking in the Stern Gelarch experiment [80]: even if discrete quanta were observed before [81, 82], it evidenced for the first time two distinct quantum states for the magnetic moment of atoms *ie* the spin states.

The Stern Gerlach experiment, developed in 1922 is described in figure 1.1.a). It showed the discretization of the magnetic moment of atoms by observing the deviation of a beam of silver atoms going through a magnetic gradient. Would the magnetic moment of the atoms be a classical quantity, one would expect a continuous range of deviation as a

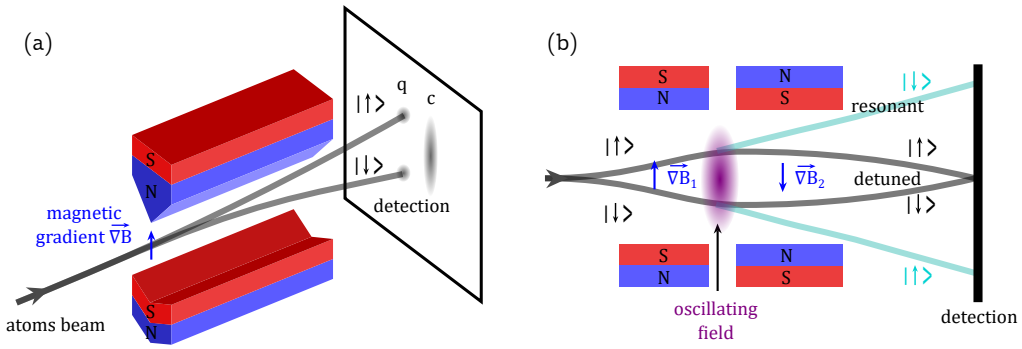

Figure 1.1: a) Stern-Gerlach experiment: a beam of silver atoms passes through a magnetic field gradient. Its deviation, which depends on the magnetic moment of each atom yields a continuous and discrete dispersion in the classical (c) and quantum (q) case respectively. b) First NMR experiment by Isidor Rabi: a beam of atoms is splitted and recombined by two opposite magnetic gradient. If a resonant oscillating field is applied in a region between the two gradients, the spin is flipped and the beams are not recombined.

function of its amplitude. The process actually taking place for each atom is an entanglement between its deviated position and its spin projection along the magnetic field. When its position is measured, only one of the two position-spin states can be obtained.

The Stern Gerlach experiment was later modified by Isidor Isaac Rabi to observe Nuclear Magnetic Resonance (NMR) of LiCl molecules [83]. This experiment is described in figure 1.1.b): a beam of molecules is spread by a magnetic gradient in a first region and recombined by an inverse magnetic gradient in a second region. In-between an oscillating magnetic field is applied. When its frequency is close to the Larmor frequency $\nu = \gamma_e B_0$ where B_0 is the uniform magnetic field between the gradients, the spin -and so the magnetic moment- of each molecule can be inverted. At resonance, this results in a lower recombination of the molecules beams as the deviations due to the gradients add up instead of cancelling. The inversion of the magnetic moment is explained by its precession about the permanent magnetic field and the probability to invert it can be calculated and was shown to follow the so-called Rabi oscillations [84].

1.1.2 Nuclear Mangetic Resonance

Rabi's discovery was followed by its implementation in a solid state system: Bloch explained [85] and observed -simultaneously with Purcell- that this precession induced in solid could be observed macroscopically. Contrary to previous experiments where atoms could not be retained or thermalized, Bloch and Purcell were able to apply a uniform magnetic field strong enough to polarize spin ensembles within a solid. Then, they applied a perpendicular rotating magnetic field for a short time and could observe the magnetic field generated by the precessing spins in a nearby pick-up coil, after the oscillating field was turned off. Indeed, after the excitation the magnetic moment of the nuclear spins are tilted away from their equilibrium point, closer to the transverse plane and they rotate around the permanent magnetic field at their Larmor frequency. This oscillation occurs over a finite timescale due to:

1. thermal fluctuations (*ie* relaxation)

2. inhomogeneities of the permanent magnetic field, which cause the spins not to precess at the same Larmor frequency and dephase from one another.

The nascent field of Nuclear Magnetic Resonance (NMR) was refined in 1950 by Erwin Hahn with the spin echo (or Hahn echo) technique [86]. Instead of a single pulse, two pulses were applied. A first precession can be observed after the first pulse but the signal is lost due to dephasing. However when the second pulse is applied after a free precession time τ, the nuclear spins precession are rephased after a time of 2τ from the first pulse. As we will see later, this technique can be used with NV spins and allows more complex investigations of inhomogeneities and dephasing as well as protecting the NV spins against them.

Since then, NRM has considerably evolved, nowadays applications include imaging (for example, medical) and analysis of molecule to obtain chemical/structural information. Although sensitivity has been improved, the amplitude of the magnetic field generated by the spins scales down with the size of the observed ensemble and constitutes the main limitation to increase resolution of imaging or observation of smaller samples.

1.1.3 Optically detected magnetic resonance

The weak magnetic field that a spin ensemble generates is not the only way to detect it: for example, the discovery of the spin was made through mechanical means. Almost simultaneously to NMR, Electron Paramagnetic Resonance (EPR) was discovered by Yevgeny Zavoisky looking at the absorption of a microwave field by salts.

Its sensitivity dramatically improved when it was combined with optical spectroscopy. In the early days of NMR it was shown that due to spin-dependent lifetime of optically excited states in crystals, spins can be both polarized and read-out through optical means [87]. The high sensitivity of Optically Detected Magnetic Resonance (ODMR) lead, in particular, to the observation of single spins in molecules [88]. Interessingly, single spins can be used as point-like magnetometer [89], or as a quantum memory to store an arbitrary quantum state.

The different systems of single spins in the solid state can be rated on account of their lifetime, decoherence/dephasing rate, read-out fidelity and operating temperature. The Nitrogen-Vacancy (NV) center is an atomic defect in diamond, which stands out due to its stable photoluminescence at room temperature. It further enables optical spin initialization and read-out, while microwave excitation allows transitions from one spin state to another. This led to the observation of a single NV spin at room-temperature in 1997 [90]. NV centers have since been used for nanoscale magnetometry [89, 91, 92] and to perform the first loophole-free Bell inequality test [19].

1.1.4 Magnetic Resonance Force Microscopy

Magnetic Resonance Force Microscopy (MRFM) is an important field to understand the advances in spin-mechanics. Mechanical detection of spins in the solid state (other than ferromagnets) was first realised in 1955 [93]: if one applies not only a strong magnetic field but also a gradient, a force is exerted on the solid when the spins are polarized. However it was only with advancements in Atomic Force Microscopy (AFM) that it sparked interest

to increase the spatial resolution of magnetic resonance imaging.

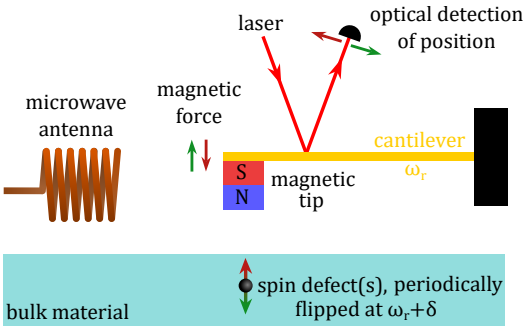

Figure 1.2: a) MRFM basic principle: a force is applied by spin(s) on a magnet positioned at the tip of a cantilever, the spin(s) are periodically flipped using microwave pulses. When the pulse frequency $\omega_r + \delta$ matches the cantilever resonance, displacement of the cantilever can be optically measured using a reflected laser beam.

The basis of Magnetic Resonance Force Microscopy (MRFM) operation is described in figure 1.2.b). A similar cantilever to the one used for AFMs is used as a mechanical oscillator: a mirror (*eg* constituted of a simple metallic coating) is placed on one side of it so its position can be measured through optical interferences of a reflected laser beam, and a ferromagnet tip is added at its extremity. The cantilever is displaced so as to sweep a plane close to the surface of a bulk material containing spins close to its surface. A microwave is then used to flip the spin at the same rate than the resonance of the mechanical oscillator. When the magnetic tip is close to the spin, it exerts a periodic force on the magnetic tip that resonantly excites the cantilever. The displacement of the oscillator can then be optically measured by taking advantage of its high quality factor.

The first MRFM experiment was realized in 1993 [94], it showed nm-scale resolution in 2003 [95] and in 2004 single spin detection was achieved [41]. This last experiment was highly promising: by reproducing this experience with a long lifetime spin (like the spin of an NV center), one could envision using it to both actuate and measure the position of a mechanical resonator (the cantilever). Such coupling can be used to first cool down the resonator's motion and -if it is strong enough- to bring it in a quantum state. Practical limitations however make this experiment particularly challenging: first, in order to obtain a strong enough coupling, the magnetized cantilever must be at a distance of a few tens of nanometers from a single spin[43]. The mechanical oscillator must also be placed at cryogenic temperatures to reduce its heating rate and must have a micron-scale size for a single spin to be able to displace it.

1.2 Trapped ions: an example of quantum harmonic mechanical oscillator

In the Stern-Gerlach experiment, magnetic coupling displaces a free-falling beam of atoms depending on the orientation of their spin. Similarly, one can couple a single spin to a harmonic mechanical oscillator: an object, the position of which is confined in a harmonic

potential. Under the right conditions, this coupling can actually be used to generate a quantum state of the mechanical oscillator. Here we will first describe this coupling in the case of a trapped ion.

A Harmonic Oscillator (HO) can be used to describe any energy minimum -at the first order approximation- and is therefore very pervasive in physics. According to quantum mechanics, the energy states of a HO can be quantized. Observing such quantized state for a mechanical HO however presents challenges, which trapped ions were able to leverage. We will first present the formalism that we use to described the HO in the quantum regime.

1.2.1 Quantum harmonic oscillator with the ladder operators method

The Schrodinger equation for the wavefunction $|\Psi\rangle$ of a particle moving in a harmonic potential in a single dimension reads:

$$\mathrm{i}\hbar\frac{\partial\Psi}{\partial\mathrm{t}} = \hat{\mathrm{H}}\,|\Psi\rangle\,, \tag{1.1}$$

with the following Hamiltonian

$$\hat{\mathrm{H}} = \frac{\hbar^2}{2\mathrm{m}}\,\hat{\mathrm{p}}^2 + \frac{1}{2}\,\mathrm{m}\omega_\mathrm{r}^2\hat{\mathrm{x}}^2, \tag{1.2}$$

where m is the mass of the particle, ω_r the angular frequency of the HO, $\hat{\mathrm{x}}$ and $\hat{\mathrm{p}}$ the operators for the particle's position and momentum respectively. Such equation can be solved with the ladder operator method developed by Paul Dirac [96]. In this method we use the creation $\hat{a}^\dagger$ and annihilation $\hat{a}$ operators to describe the motion of the oscillator:

$$\begin{cases} \hat{x} = a_0\left(\hat{a}^\dagger + \hat{a}\right) \\ \hat{p} = ip_0\left(\hat{a}^\dagger - \hat{a}\right) \end{cases} \text{with} \quad a_0 = \sqrt{\frac{\hbar}{2m\omega_r}}\,, \quad p_0 = \sqrt{\frac{\hbar m\omega_r}{2}}. \tag{1.3}$$

Using these operators the Hamiltonian can be rewritten:

$$\hat{\mathrm{H}} = \omega_\mathrm{r}\left(\hat{\mathrm{a}}^\dagger\hat{\mathrm{a}} + \frac{1}{2}\right). \tag{1.4}$$

Its eigenstates are the so-called Fock states or number states:

$$|\mathrm{n}\rangle = \frac{\left(\hat{\mathrm{a}}^\dagger\right)^\mathrm{n}}{\sqrt{\mathrm{n!}}}\,|0\rangle\,, \tag{1.5}$$

with n a positive integer that describes the number of excitation (phonon) and $|0\rangle$ the HO ground state. Their eigenvalues are : $\omega_\mathrm{n} = \hbar(\mathrm{n} + \frac{1}{2})$.

The creation and annihilation operators as well as the phonon number operator $\hat{\mathrm{N}} = \hat{\mathrm{a}}^\dagger\hat{\mathrm{a}}$ take their name from their action on the Fock states:

$$\begin{aligned} \hat{a}^\dagger\,|n\rangle &= \sqrt{n+1}\,|n+1\rangle \\ \hat{a}^\dagger\,|n\rangle &= \sqrt{n}\,|n-1\rangle \\ \hat{N}\,|n\rangle &= n\,|n\rangle\,. \end{aligned} \tag{1.6}$$

1.2.2 The emergence of trapped ions

Most Mechanical Oscillators (MO) have a high average phonon number at room temperature and do not lend themselves easily to quantum manipulation. Indeed $300k_B/\hbar \sim 7$ THz, which means any oscillator of lower frequency will be in a thermal state at room temperature, that is in a non-coherent superposition of many Fock states. Observing a MO in the quantum regime therefore requires either to cool down the environment so that $k_BT < \hbar\omega$ or to have the MO decoupled or isolated from the environment and a cooling mechanism to displace it from the thermal equilibrium. Once in the ground state one can use reverse the cooling mechanism to create an arbitrary state of higher energy (eg Fock state, superposition state) [34].
Trapped ions were the first system that met this criteria. At high vacuum the center of mass of a trapped ion constitutes a well isolated HO. Then, its motion can be manipulated by using laser or microwave fields to couple its motion to its internal degrees of freedom such as electron orbitals or spins. Single ions were first isolated in a Paul trap in 1980 [97]. The Paul trap was proposed by W. Paul [9]: it uses a dynamical electric potential to confine the ion and eventually earned him the Nobel prize in 1989. Typical electrodes that generate the electric potential are shown in figure 1.3.a). Cooling of ion ensembles was first showed in 1978 with an oscillator cooled to lower than 40K using laser light [10]. The limitation for the achieved temperature was found to be the linewidth of the optical transition compared to the frequency of the MO: the latter must be higher than the former to enable efficient cooling. Such regime is called the Resolved Sideband (RSB) regime and was reached ten years later thereafter enabling ground state cooling of a mercury ion [11]. In the RSB regime one can perform a Rabi oscillation on the sidebands and can not only cool down the MO to its ground state, but also map any superposition state from the electronic states unto a superposition of adjacent phonon states or entangle the MO state with the electronic state [15].

1.2.3 Spin-mechanical coupling

We now take a look at the manipulation of the motion of trapped ion in the quantum regime. We will here only describe a method using magnetic coupling to an electron spin. It should be noted that for trapped ions, the use of laser light and the Doppler effect [98] is actually more common. Coupling to the spin as presented here was proposed later [99] and only recently realized [100]. Still, this method uses a similar formalism and allows us to introduce the coupling we will use to control the motion of levitating micro-diamonds.

We consider the quantized energy of the Center of Mass (CoM) of a trapped ion containing a one halve electron spin. The energy states of the two degrees of freedom are depicted in figure 1.3.b). One can use a magnetic field gradient to couple the spin and the motion of the ion: the energies of the spin states will depends on the position of the ion because of the varying Zeeman effect. The Hamiltonian of this coupled system can be written using the ladder operators:

$$\begin{aligned} H/\hbar = &\ \omega_r \hat{a}^\dagger \hat{a} + \omega_s \hat{S}_z + a_0 \left(\hat{a} + \hat{a}^\dagger\right) G_m \gamma_e \hat{S}_z \\ = &\ \underbrace{\omega_r \hat{a}^\dagger \hat{a}}_{\text{Mechanics}} + \underbrace{\omega_s \hat{S}_z}_{\text{Spin}} + \underbrace{\lambda(\hat{a} + \hat{a}^\dagger)\hat{S}_z}_{\text{Spin-mechanical}} \qquad \text{with} \quad \lambda = G_m \gamma_e a_0, \end{aligned} \tag{1.7}$$

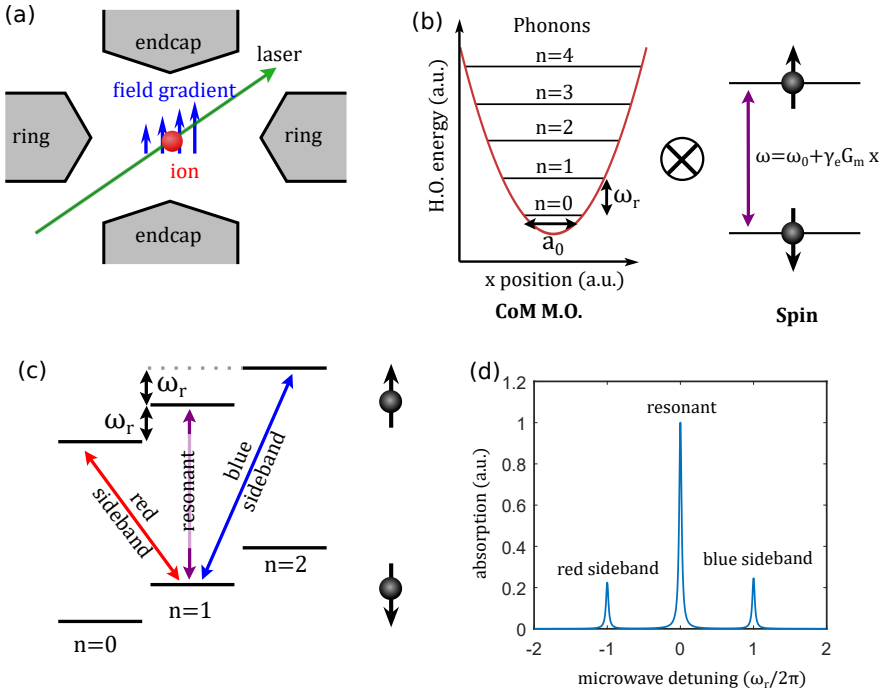

Figure 1.3: a) Cut of the ion trap electrodes: an oscillating voltage is applied between the ring and endcap electrodes, resulting in harmonic confinement for ions at the center of the trap. A magnetic field gradient associated with a microwave field or a laser can be used to control the motion of the ion. b) Left: harmonic oscillator's potential energy (red curve) and the quatized phonon number states (black lines). a_0 is the amplitude of the zero-point fluctuations of the position. Right: two level system (spin one halve), the energy of which depends on the position due to the magnetic gradient and Zeeman effect. c) Dressed states for the two level system and a harmonic oscillator. The electronic transition are addressed by a microwave field, and cross-phonon transition can occur due to the spin-mechanical coupling. d) Absorption spectrum of a trapped ion, the sidebands (generated by the spin-mechanical coupling) result in absorption (creation) of a phonon for the red (blue) sideband.

where $\hat{S}_z$ is the Pauli operator along the B field direction, ω_s is the energy splitting between the spin states at the trap center, G_m the magnetic field gradient and γ_e the gyromagnetic ratio of the electron. The first two terms are the energy of the non-interacting MO and spin while the third describes their magnetic coupling with a rate λ. This latter term corresponds to a Zeeman effect for the spin and to a force applied to the MO.

Because the energy between the spin states ω_s is often much larger than the energy span between two adjacent Fock states ω_r, a microwave usually drives the spin state in order to allow a resonant coupling. In a frame rotating at the frequency of the microwave $\omega = \omega_s - \Delta$, the full Hamiltonian is then:

$$H/\hbar = \omega_r \hat{a}^\dagger \hat{a} + \frac{\Delta}{2}\hat{S}_z + \lambda\left(\hat{a} + \hat{a}^\dagger\right)\hat{S}_z + \frac{\Omega}{2}\hat{S}_x, \tag{1.8}$$

where Ω is the Rabi frequency associated with the microwave drive.

To better capture the effect of the spin-mechanical coupling, we diagonalize the spin-only part of the Hamiltonian in the $|\pm\rangle$ basis:

$$\begin{cases} |+\rangle = & \sin\psi\,|-1/2\rangle + \cos\psi\,|+1/2\rangle \\ |-\rangle = & -\cos\psi\,|-1/2\rangle + \sin\psi\,|+1/2\rangle \end{cases} \quad \text{with} \quad \tan(2\psi) = \frac{\Omega}{\Delta}. \tag{1.9}$$

Writing the spin operators in the $|\pm\rangle$ basis, the Hamiltonian then reads:

$$H/\hbar = \omega_r \hat{a}^\dagger \hat{a} + \omega_\pm \hat{S}_z + \lambda\cos(2\psi)\underbrace{\left(\hat{a}+\hat{a}^\dagger\right)\hat{S}_z}_{\text{longitudinal}} - \lambda\sin(2\psi)\underbrace{\left(\hat{a}+\hat{a}^\dagger\right)\hat{S}_x}_{\text{transverse}}, \tag{1.10}$$

with $\omega_\pm = \sqrt{\Omega^2+\Delta^2}$.

The spin-mechanical coupling is now splitted in two terms that we have named "longitudinal" and "transverse". The longitudinal term corresponds to a spin-dependent force on par with a position dependent Zeeman effect. The transverse term corresponds to an energy exchange between the spin and the MO, it will in practice cause a cooling or heating of the mechanical oscillator.
These two effects will play an important role in the latter work of this thesis but for now we will focus on the transverse term, enabling coherent manipulation of the MO.

1.2.4 Coherent manipulation of the mechanical state

Discarding the longitudinal term we obtain:

$$\begin{aligned} H/\hbar &= \omega_r \hat{a}^\dagger \hat{a} + \omega_\pm \hat{S}_z - \widetilde{\lambda}\left(\hat{a}+\hat{a}^\dagger\right)\hat{S}_x \\ &= \omega_r \hat{a}^\dagger \hat{a} + \omega_\pm \hat{S}_z - \widetilde{\lambda}(\hat{a}+\hat{a}^\dagger)(\hat{S}_+ + \hat{S}_-) \end{aligned} \tag{1.11}$$

with $\widetilde{\lambda} = \lambda\sin(2\psi)$ and where $\hat{S}_+ = \hat{S}_x + i\hat{S}_y$ and $\hat{S}_+ = \hat{S}_x - i\hat{S}_y$ are the raising and lowering operators of the spin. At the spin-mechanical resonance $\omega_r = \omega_\pm$ and under the rotating wave approximation, we eliminate the non-resonant terms of the spin-mechanical term thereby obtaining the Hamiltonian

$$H/\hbar = \omega_r \hat{a}^\dagger \hat{a} + \omega_\pm \hat{S}_z - \widetilde{\lambda}\left(\hat{a}\hat{S}_- + \hat{a}^\dagger \hat{S}_+\right). \tag{1.12}$$

This is the Hamiltonian of the Jaynes–Cummings model. It describes the coherent exchange between spin and phonons which is embodied by coherent oscillations between dressed states of adjacent phonon numbers $|n\rangle\,|-\rangle$ and $|n-1\rangle\,|+\rangle$.
Given one can initialize the spin state in an arbitrary state and if the coupling rate λ is stronger than the decoherence, it allows one to generate any arbitrary quantum state of the mechanical oscillator [34]. Cooling can for example be achieved by polarizing the spin state into the $|-\rangle$ state and tuning a weak driving field ($\Omega \ll \Delta$) red-detuned ($\Delta = -\omega_r$) compared to the resonant spin transition at ω_s. One can similarly heat up the CoM motion with a blue detuned microwave ($\Delta = +\omega_r$). These cooling and heating transitions between adjacent Fock states are shown in figure 1.3.c). Incidently, when these transitions are possible (therefore, out of the ground state) the spin resonance spectrum features two sidebands flanking the resonance at detunings of $\pm\omega_r$, as depicted in figure 1.3.d).

Such a fine control and coupling of these internal (spin, electron) and external (CoM) quantum degrees of freedom [98] led to outstanding prospects. Trapped ions were for example proposed to build quantum computers [14]. The motion of two ions in the same trap is in fact coupled due to the Coulomb force, resulting in collective oscillation modes that can be cooled down [101] and used as a bus to entangle two ions [102]. One therefore obtains a logic gate between the information stored in the internal degrees of freedom of both ions. So far, up to 14 ions have been entangled in a single linear ion trap [16].

1.3 Center of mass spin-mechanics with NV spins

The same spin-mechanical coupling that allows control of an ion's motion can actually be used with a massive mechanical oscillator coupled to a well controlled two level system. The field of opto-mechanics has already achieved impressive results regarding the control of a mechanical oscillator in the quantum regime [35, 37, 38]. However, the use of a two level system offers interesting prospects. In particular, one could transfer the high degree of control, which is now achieved for certain two-level systems in the solid-state, unto the mechanical oscillator.

Figure 1.4.a) depicts the states of a two level system (here, a spin) dressed by the Fock states of a mechanical oscillator. As explained for trapped ions, a strong spin-mechanical coupling allows coherent diagonal transitions between two different spin states and adjacent Fock states. The ability to generate an arbitrary state for the two level system can then be transferred to the state of the mechanical oscillator, if its decoherence and heating rate are slower than the coupling. The NV spin is an attractive system for such scheme because of its long lifetime and coherence time and as it can be fully controlled using optical and microwave fields [90]. Here, we will specifically describe schemes that have been proposed to couple the motion of a mechanical oscillator to an NV spin.

1.3.1 Coupling schemes

Interaction between a two level system and a large mechanical oscillator can be achieved through several means [42]. Here, we focus on the case of the NV center, for which two types of interaction have been used.

Strain coupling

One can first use the intrinsic strain in the diamond crystal to mediate the coupling: figure 1.4.b) depicts a cantilever made of bulk diamond, with a single NV spin embedded in the cantilever. The strain within the crystal actually depends on the position of the cantilever, because the cantilever applies a stress on the diamond as it deforms the crystal.
The strength of this coupling is however small: it has only been observed while applying a strong drive to the mechanical oscillator so that the large amplitude of its oscillations compensates for the low zero-phonon coupling rate. Coherent control of an NV spin was achieved using this method [103, 104] but back-action of the NV spin on the mechanical oscillator has not been observed.

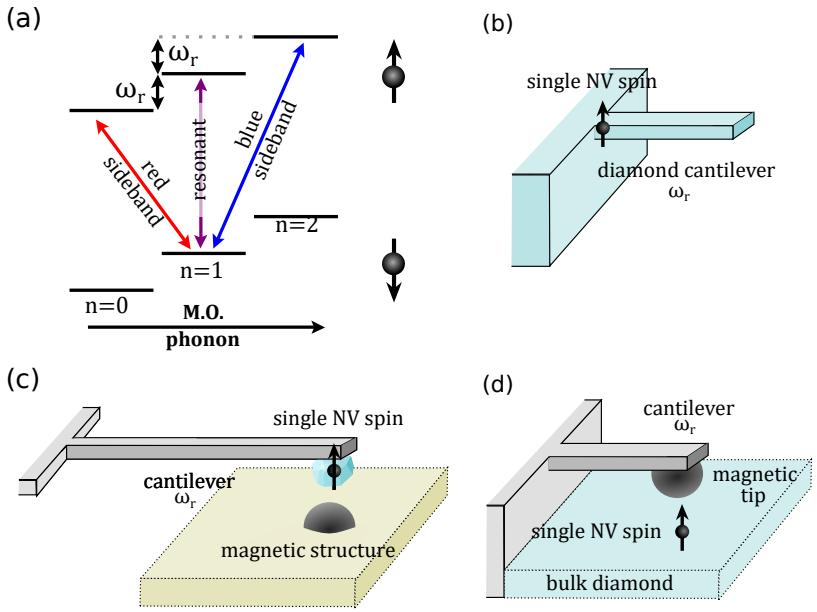

Figure 1.4: a) Spin states dressed by the mechanical oscillator (MO). A microwave magnetic field can be used to either solely change the spin or both the spin and the phonon number with an additive Spin-Mechanical coupling (diagonal arrows). b) Scheme for a strain mediated spin-mechanical coupling. Magnetic spin-mechanical coupling with c) a diamond on a cantilever and d) a magnetized cantilever on top of a bulk diamond, with a shallow single NV spin.

Magnetic coupling

The NV spins can also be coupled to a cantilever through magnetic coupling [43]. Figure 1.4.c) illustrates how one obtains such coupling: a nano-diamond with a single NV spin is positioned at the tip of a cantilever, while a magnetic structure is brought in its close vicinity to generate a strong magnetic gradient G_m. Under these conditions, the Hamiltonian for the NV spin and the mechanical oscillator of frequency ω_r can the be written

$$\begin{aligned} H/\hbar = &\quad \omega_r \hat{a}^\dagger \hat{a} + \omega_s \hat{S}_z + a_0 \left(\hat{a} + \hat{a}^\dagger\right) G_m \gamma_e \hat{S}_z \quad \text{with} \quad a_0 = \sqrt{\frac{\hbar}{2m\omega_r}} \\ = &\quad \omega_r \hat{a}^\dagger \hat{a} + \omega_s \hat{S}_z + \lambda \left(\hat{a} + \hat{a}^\dagger\right) \hat{S}_z \qquad\qquad\qquad \lambda = G_m \gamma_e a_0, \end{aligned} \tag{1.13}$$

where $\hat{S}_z$ is the Pauli operator along the z direction, ω_s the energy splitting between the spin states, γ_e the gyromagnetic ratio of the electron and where $\hat{a}^\dagger$ and $\hat{a}$ are the creation and annihilation operators for the mechanical oscillator. We obtain exactly the same spin-mechanical Hamiltonian than in equation 1.7, which, in particular, enables coherent control of the mechanical oscillator.

However, entering the strong coupling regime, where the spin-mechanical coupling rate is higher than the decoherence rate is challenging. This mainly stems from the high mass of the mechanical oscillator, which reduces the amplitude of the zero-point fluctuations a_0 of the mechanical oscillator. The coupling rate can be increased by maximizing the magnetic gradient: the strong coupling regime could then be reached with magnetic gradients

in the order of 10^7 T/m [43].

The first experiment to observe this coupling was performed with the scheme described in figure 1.4.c) [44, 105]. A magnetic gradient of up to 4.5 10^4 T/m was achieved by positioning a magnetic structure below a nano-diamond attached to a silicon carbide nano-wire. The spin-mechanical coupling allowed for a single NV spin to measure excited oscillations of the nano-wire.
In another experiment, a reversed set-up was used: a magnetized cantilever was approached close to the surface of a bulk diamond where shallow single NV spins were implanted [45]. A magnetic gradient up to 10^5 T/m was achieved and the thermal fluctuation of the mechanical oscillator could be measure by the NV spin. In both experiments, the coupling rate λ did not exceed the Hz range and control of the mechanical oscillator could not be achieved.

1.3.2 Levitated diamonds

An alternative system, which reduces the mass of the mechanical oscillator and suppresses its heating would be to use a levitating nano-diamond as the mechanical oscillator. Such particles, under high vacuum have reached record-high quality factor [46]. The center of mass motion of these levitating particles is usually manipulated using optical [49, 51, 53] or electric forces [54, 55]. Optical measurement of the particle's position enables cooling of its motion through a feed-back loop [53]. Recently, this method allowed the observation of the quantized motion of a levitating silica nano-sphere [56].

Optical tweezers [47] is the most established trapping method and could provide a high enough frequency ($\sim$ 100 kHz) to reach the sideband resolved regime for spin-mechanics with levitating diamonds. Several experiments have therefore been performed where nano-diamonds are levitated in optical tweezers, and embedded NV spins are manipulated through electron spin resonance [62–64].
However, these first experiments were performed under atmospheric pressure and, under vacuum conditions, a strong heating of the diamond was observed [64, 66, 67]. This heating is attributed to absorption of the trapping beam by impurities in the diamond crystal [64, 67, 106]. Although the use of ultra-pure diamonds could partially solve this issue [106], even a few impurities will eventually limit the pressure achievable, given the high optical power used to trap the particle [106]. It should be noted that heating of the internal degrees of freedom was also observed with levitated silica nano-spheres [107], but at a much higher vacuum due to the low absorption of silica at the wavelength of the trapping laser.
Apart from reducing the absorption of the levitated particle, it is also possible to optically cool down the internal degrees of freedom using anti-stokes emission in rare-earth crystals [108, 109]. An interesting development is the realization of such cooling in an optically levitated nano-crystal [110]: if such particle can be efficiently combined with a nano-diamond, it could prevent it from heating under high vacuum.

To prevent a levitating diamond from heating, another scattering-free trap could be employed: optical fields are then only required to control and observe the NV spin, with a much lower intensity than what is used in optical traps. Both Paul traps [65] and magneto-

gravitational traps [49] have shown stable trapping of nano-diamonds. The frequency of the center of mass oscillations in those traps is however for now limited to the kHz range [49, 52], thereby preventing one from attaining the resolved sideband regime.

Spin-mechanics experiments are still possible outside of this regime. In particular, matter wave interferometry experiments have been proposed with a levitating diamond when the trap is turned off or loosened [57, 60]. The general idea is similar to the Stern-Gerlach or Rabi experiments described in section 1.1: a magnetic gradient is used to spatially separate two spin-dependent paths, which are then recombined by applying a π pulse on the NV spin.

Finally, levitation experiments are prone to the use of the angular degrees of freedom. Its investigation was made possible following the levitation of non-spherical particles in Paul traps [68] and optical tweezers [69, 70], in particular, light-driven rotation at MHz frequencies have been observed [69, 70]. As we will see latter in this thesis, the NV spin is in fact well-suited for coupling to the angular degrees of freedom.

Chapter 2

Levitation of micro-particles in a Paul trap

In this thesis, we investigate the coupling of a levitating oscillator with NV spins in diamond. In order to do so, we propose using a Paul trap to levitate micro-diamonds or micro-magnets. It should be noted that our levitation scheme drove us to focus not on the Center of Mass (CoM) of this levitating object but on its angular degrees of freedom. Here, we will first discuss the theory of the Paul trap, in particular how it confines the CoM and the angular degrees of freedom of a charged particle. We then describe the experimental set-up: first the trap itself and then the tools that we use to observe the motion of a levitating particle. We finally present two limitations, which for now impose certain working conditions on the system as it is.

2.1 Confinement of a charged dielectric particle in a Paul trap

Let us first describe the mechanism that allows Paul traps to confine charged particles. We will see that this mechanism, well-established for the CoM of an ion [9, 48, 98] can be extended to the angular degree of freedom of a particle with a macroscopic and anisotropic charge distribution [73].

2.1.1 Confinement of the CoM

Paul traps rely on electric forces to confine ions or charged particles. A simple harmonic electric potential is however not sufficient to confine a particle in all three directions of space. This is evidenced by the Laplace equation for the electric potential $\phi(x, y, y)$

$$\frac{\partial^2\phi}{\partial x^2} + \frac{\partial^2\phi}{\partial y^2} + \frac{\partial^2\phi}{\partial z^2} = 0, \tag{2.1}$$

that shows that if two directions are confined ($eg\ \partial^2\phi/\partial^2 x, \partial^2\phi/\partial^2 y > 0$), the third one is anti-confined ($\partial^2\phi/\partial z^2 < 0$).

A Paul trap circumvents this issue by using an oscillating electric field. A voltage oscillating at a frequency Ω is applied to electrodes in order to generate the electric potential

ϕ in a certain region of space close to the center of the trap $(x, y, z = 0)$:

$$\phi(x, y, z, t) = \frac{V_{ac}\cos(\Omega t) + V_{dc}}{z_0^2}\left(\eta_x x^2 + \eta_y y^2 + \eta_z z^2\right), \tag{2.2}$$

where V_{AC} is the amplitude of the oscillating voltage, V_{DC} a bias voltage, z_0 a characteristic dimension of the electrodes and η_x, $\eta_y > 0$, $\eta_z = -\eta_x - \eta_y$ geometric factors related to the shape of the electrodes. A typical electrodes configuration is a ring associated to endcap electrodes as shown in figure 1.3.a) but many variations are possible [111–113].

Equation of motion for the CoM

For a point-like particle of mass m and charge Q, the equations of motion are then

$$\begin{cases} \ddot{x} + \dfrac{\eta_x Q}{m z_0^2}\left(V_{dc} + V_{ac}\cos(\Omega t)\right) x = 0 \\ \ddot{y} + \dfrac{\eta_y Q}{m z_0^2}\left(V_{dc} + V_{ac}\cos(\Omega t)\right) y = 0 \\ \ddot{z} + \dfrac{\eta_z Q}{m z_0^2}\left(V_{dc} + V_{ac}\cos(\Omega t)\right) z = 0. \end{cases} \tag{2.3}$$

The motion along each direction x, y and z is decoupled and can be written in the so-called dimensionless Matthieu equation:

$$\frac{d^2 u}{d\tau^2} + \left(a_u + 2q_u\cos 2\tau\right) u = 0 \tag{2.4}$$

where $u = x, y, z$ and with the following dimensionless parameters

$$\begin{aligned} \tau &= \frac{\Omega t}{2} \\ a_u &= 4\frac{\eta_u Q V_{dc}}{m z_0^2 \Omega^2} \\ q_u &= 2\frac{\eta_u Q V_{ac}}{m z_0^2 \Omega^2}. \end{aligned} \tag{2.5}$$

This equation can be solved exactly and has two solutions. Given the values of the parameters a_u and q_u only one of the two is possible:

- stable solution: u is bound, oscillates around $u = 0$ with an amplitude related to the initial conditions
- unstable solution: u oscillates around 0 with increasing amplitude.

CoM stability condition

In practice, the particle is often only observed when the motion is stable and is otherwise lost. Its motion is stable when the parameters a and q are within the region defined by the two curves [48]:

$$\begin{cases} a_+ = 1 - q - \dfrac{1}{8}q^2 + \dfrac{1}{64}q^3 - \dfrac{1}{1536}q^4 + \dfrac{11}{35864}q^5 \\ a_- = -\dfrac{1}{2}q^2 + \dfrac{1}{128}q^4 - \dfrac{29}{2304}q^6 + \dfrac{68687}{18874368}q^8. \end{cases} \tag{2.6}$$

This region is drawn in figure 2.1 for the three axes x, y and z in the symmetric case $\eta_x = \eta_y = -\eta_z/2$. Because the particle is only stably trapped if its motion is stable along all axes, the stability region of the particle is the overlap of all three stability regions. In practice one can always find a stability region by tuning the amplitude, bias and frequency of the voltage applied to the trapping electrodes. Note that when one considers levitating solid in finite vacuum, damping has to be taken into account in the equation of motion. This results in Matthieu equations with modified parameters a', q' that usually broadens the region of stable motion [114].

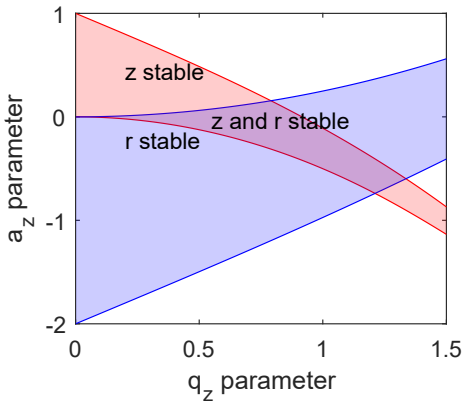

Figure 2.1: Stability diagram for the motion of a trapped ion with a revolution symmetry around the z axis for the trapping potential. Here r corresponds to the x or y coordinates.

Harmonic confinement

Within the stability region, for all three axes $u = x, y, z$ the motion of the particle can be decomposed into two parts with different frequencies [48]:

1. the micromotion: a fast oscillation at frequency Ω
2. the secular or macro-motion: slower oscillations at the frequency ω_u.

The micromotion results directly from the oscillating potential: as long as the particle is not at the center of the trap ($u = 0$), an oscillating electric force is applied to the particle. However since the particle has a finite mass and moves in the potential, the electric force applied to it changes and does not cancel out completely over one period of the micromotion: this results in the secular motion. Under certain conditions ($q \lesssim 0.4$) one can show that the force applied to the particle, averaged over a period of the micromotion, reproduces a harmonic confinement with angular frequency ω_u yielding the secular (or macro) motion of the particle [115].

The position of the CoM of a trapped ion as a function of time is illustrated in figure 2.2.a): the slow oscillation corresponds to the macro-motion while fast oscillations are the micro-motion. The amplitude of the micro-motion depends on the average position of the particle: as it moves further away from the center of the trap, the amplitude of the oscillating electric field increases.

One can therefore consider the particle as being in a harmonic pseudo-potential with:

$$U_{\text{com}}(x,y,z) = \frac{1}{2}m\sum_{u=x,y,z}\omega_u^2 u^2 \qquad \text{with} \quad \omega_{\text{u}} = \sqrt{a_u + \frac{q_u^2}{2}}\Omega. \tag{2.7}$$

Note that in order to have a harmonic potential, the condition $q < 0.4$ and the dependency of the harmonic confinement frequency implies that the AC trap frequency Ω is always higher than the resulting confinement ω_u.

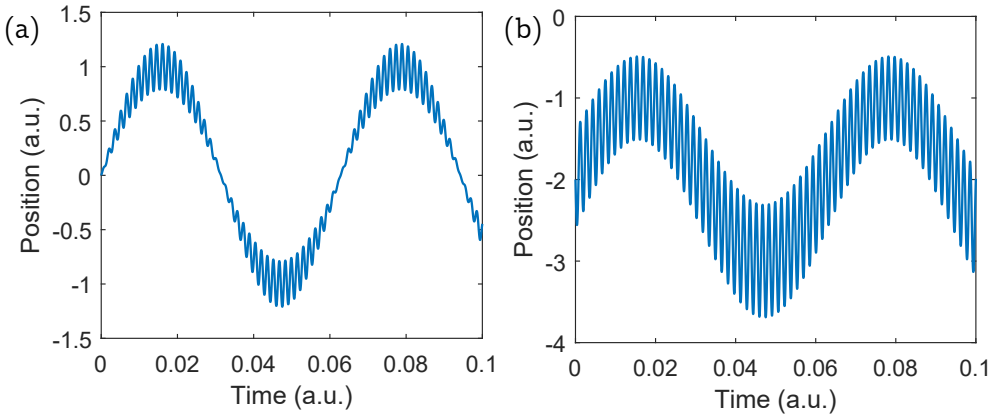

Figure 2.2: Position of the CoM of a trapped ion as a function of time: a) without external forces and b) with a strong force that shifts the center of the trap.

Under ideal conditions, micro-motion will remain small as long as the amplitude of the macro-motion is limited. However, an external force -*eg* gravity for large particles- can shift the center of the trap at a position where the electric field induces a strong micro-motion. Figure 2.2.b) depicts the CoM motion of a charged particle under these conditions: a strong micro-motion occurs even at the center of the trap. In our experiment in particular, the presence of a strong micro-motion is harmful for measurements of the position as it blurs the optical signal that we use (see section 2.4.2).

2.1.2 Confinement of the angular degrees of freedom

Levitating a diamond particle of finite size containing NV centers makes the angular degree of freedom an important issue. It first brings new requirement compared to ions: as we will see later the NV center is not isotropic and its orientation compared to the magnetic field matters and cannot be left randomly rotating. Besides, considering a finite particle with multiple charges means the electric field exerts not only a force to the particle but also a torque.
This situation bears similarities to the collective motion of ions in Paul traps: when two or more ions are trapped in the same trap, Coulomb interaction gives rise to additional modes of motion aside from single ion oscillations. One such mode, the so-called rocking mode is described in figure 2.3.a): the two ions can oscillate out of phase along a direction perpendicular to the axis along which they are trapped. A bigger particle with several charges in fact behaves similarly: the diamond depicted in figure 2.3.b), with only two charges, aligns itself with one axis of the Paul trap and its angular degree of freedom is a confined oscillation mode.

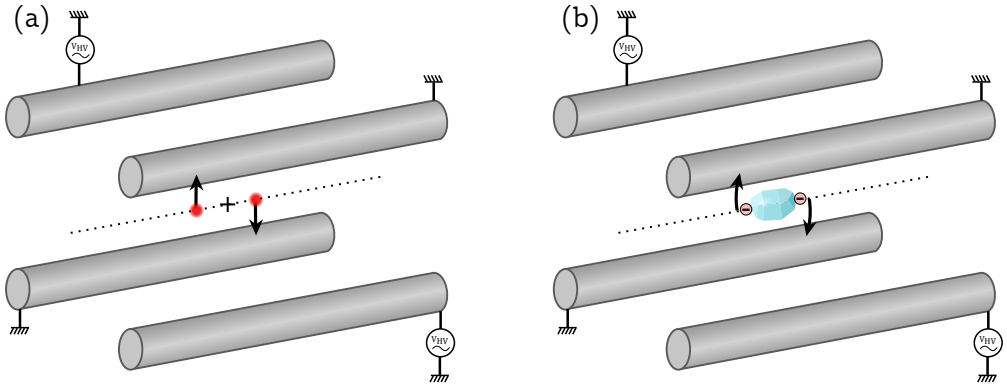

Figure 2.3: a) Ion trap with four rods as electrodes. Two trapped ions are depicted as red dots while a cross indicates the center of the trap for a single ion. The black arrow shows collective motion of the two ions, here a rocking mode. b) Trapped micro-diamond with only two electronic charges, which aligns themselves with one axis of the trap (here the rod axis).

Although the collective motion of ions is well known, and micro-particle with multiple charges were levitated in Paul traps [48] very early (before ions), their angular confinement had, to the best of our knowledge, not yet been studied. In fact, we consider the confinement of the angular degrees of freedom caused by the Paul trap only after observing NV spins in a levitating micro-diamond.

Electric torque and equilibrium position

Let us now consider a particle levitating in a Paul trap, with multiple charges at different positions with respect to the centroid of the charges. Here, we consider that the centroid of charges matches the center of mass and is frozen at the center of the trap: any rotation of the particle happens around both and the total force applied to the particle always cancels out.

The torque applied by the electric field deriving from eq. 2.2 to a charge Q_i at vector position $\overrightarrow{OM}_i$ with coordinates (x_i, y_i, z_i) reads:

$$\vec{M}_i = Q_i \overrightarrow{OM}_i \times \vec{E}(x_i, y_i, z_i) \tag{2.8}$$

$$= \begin{pmatrix} x_i \\ y_i \\ z_i \end{pmatrix} \times Q_i \frac{V(t)\eta_z}{2z_0^2} \begin{pmatrix} (1-\delta)x_i \\ (1+\delta)y_i \\ 2z_i \end{pmatrix} \tag{2.9}$$

$$= \frac{Q_i V(t)\eta_z}{2z_0^2} \begin{pmatrix} y_i z_i \,(3-\delta) \\ x_i z_i \,(3+\delta) \\ x_i y_i \delta \end{pmatrix}, \tag{2.10}$$

where we have defined $\delta = (\eta_y - \eta_x)/\eta_z$ and $V(t) = V_{ac}\cos(\Omega t) + V_{dc}$.

The total torque applied to the particle is the sum of all individual torques for each charge. It reads:

$$\vec{M} = \frac{V(t)\eta_z}{2z_0^2} \sum_i Q_i \begin{pmatrix} y_i z_i \,(3-\delta) \\ x_i z_i \,(3+\delta) \\ x_i y_i \delta \end{pmatrix}. \tag{2.11}$$

It should be noted that there exists at least one orientation of the particle for which this torque cancels out. This can be demonstrated by considering a time-independent electric potential (*ie* $V_{ac} = 0$) with a particle maintained at the center of the trap through another force applied to its center of mass. Here the time-independent electric potential yields a conservative electric torque. At the minimum of the corresponding potential energy, the particle is at its equilibrium and the electric torque cancels out. If the electric potential varies with time as in equation 2.2 the considered orientation is either a minimum or a maximum but remains an equilibrium point -alternating from stable to unstable. When the particle is in this orientation, the coordinates of its charges therefore obey the equation:

$$\sum_i Q_i y_i^{eq} z_i^{eq} = \sum_i Q_i x_i^{eq} z_i^{eq} = \sum_i Q_i x_i^{eq} y_i^{eq} = 0. \tag{2.12}$$

Equations for the Euler angles in the rotating frame

In order to describe the rotation dynamics of the particle within the Paul trap we use a rotating frame (X,Y,Z) with axes fixed to the particle. We choose axes parallel to the trap axes (x,y,z) when the particle is at its equilibrium position in the electric field. When the particle orientation is out of the equilibrium, this frame can be obtained from the laboratory frame (x,y,z) by performing three rotations, pictured in figure 2.4. First the (x,y,z) frame is rotated of ψ around the z axis, the rotated frame (x',y',z') is then rotated of θ around the y' axis giving the (x",y",z") frame, which is finally rotated of ϕ around the x" axis yielding the rotating frame (X,Y,Z). Here, we follow the Tait–Bryan angles (z,y,x) convention for the ψ, θ and ϕ angles.

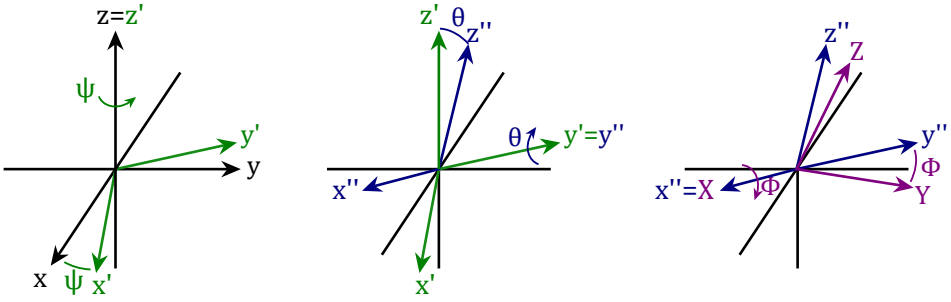

Figure 2.4: Succesion of rotations transforming the trap axes (x,y,z) into the rotating frame (X,Y,Z).

Let us now define the rotation matrices as:

$$R_z(\phi) = \begin{pmatrix} \cos\phi & -\sin\phi & 0 \\ \sin\phi & \cos\phi & 0 \\ 0 & 0 & 1 \end{pmatrix}, R_y(\phi) = \begin{pmatrix} \cos\phi & 0 & \sin\phi \\ 0 & 1 & 0 \\ -\sin\phi & 0 & \cos\phi \end{pmatrix}, R_x(\phi) = \begin{pmatrix} 1 & 0 & 0 \\ 0 & \cos\phi & -\sin\phi \\ 0 & \sin\phi & \cos\phi \end{pmatrix}.$$

The matrix allowing one to obtain the coordinates (X,Y,Z) of the rotating frame from (x,y,z) is then $R(\phi,\theta,\psi) = R_z(\psi)R_y(\theta)R_x(\phi)$ and we have:

$$\begin{pmatrix} X \\ Y \\ Z \end{pmatrix} = R(\phi,\theta,\psi) \begin{pmatrix} x \\ y \\ z \end{pmatrix}. \tag{2.13}$$

We will now rewrite the electric torque in the rotating frame using only coordinates from the rotating frame. This will later be used in the Euler equation but more generally, it allows us to see how the electric torque varies with the orientation of the particle and with intrinsic parameters such as the the geometry of the particle.
In order to do so, we write the electric field as a matrix product of, from right to left: the rotating frame coordinates, a rotation matrix R^{-1} to obtain the x, y, z coordinates from X, Y, Z, a matrix giving the electric field in the fixed frame from the fixed frame coordinates and another rotation matrix R to write the electric field in the rotating frame coordinates. The field in the rotating frame is then:

$$\begin{pmatrix} E_X \\ E_Y \\ E_Z \end{pmatrix} = R\frac{V(t)\eta_z}{2z_0^2}\begin{pmatrix} 1-\delta & 0 & 0 \\ 0 & 1+\delta & 0 \\ 0 & 0 & 2 \end{pmatrix} R^{-1}\begin{pmatrix} X \\ Y \\ Z \end{pmatrix}. \tag{2.14}$$

The total electric torque can then be rewritten as:

$$\vec{M} = \sum_i \frac{Q_i V(t)\eta_z}{2z_0^2}\begin{pmatrix} X_i \\ Y_i \\ Z_i \end{pmatrix} \times \left(A\begin{pmatrix} X_i \\ Y_i \\ Z_i \end{pmatrix}\right) \tag{2.15}$$

$$A = R\begin{pmatrix} 1-\delta & 0 & 0 \\ 0 & 1+\delta & 0 \\ 0 & 0 & 2 \end{pmatrix} R^{-1}. \tag{2.16}$$

It should be noted that the coefficients of the matrix A are a linear combination of X, Y, Z and that because R is orthogonal, A is symmetric *ie* $A^{ij} = A^{ji}$. We also know that because the rotating frame was chosen to be the fixed frame when the particle is at equilibrium we always have $\sum_i Q_i X_i Z_i = \sum_i Q_i X_i Z_i = \sum_i Q_i X_i Y_i = 0$ so all contributions of the cross product but the square coordinates will be eliminated. Using the symmetry of A we finally obtain:

$$\vec{M} = \frac{QV(t)\eta_z}{2z_0^2}\begin{pmatrix} A^{2,3}S_X \\ A^{1,3}S_Y \\ A^{1,2}S_Z \end{pmatrix} \tag{2.17}$$

with $Q = \sum_i Q_i$ and

$$\begin{array}{l} S_X = \sum_i Qi/Q(Y^2 - Z^2) \\ S_Y = \sum_i Qi/Q(Z^2 - X^2) \\ S_Z = \sum_i Qi/Q(X^2 - Y^2). \end{array} \tag{2.18}$$

In eq. 2.17, the coefficients of A depend on the orientation of the rotating frame (*ie* of the particle) and on the geometry of the trap while the S parameters are fixed by the geometry of the particle charges. Here we simplify the coefficients $A^{i,j}$ by discarding terms with mixed Euler angles, in the limit where at least all angles but one are small, we obtain:

$$\left\{ \begin{array}{lll} A^{2,3} = & (3+\delta)\frac{\sin 2\phi}{2} + \mathcal{O}(\theta\psi) + \mathcal{O}(\phi\theta^2) \\ A^{1,3} = & (3-\delta)\frac{\sin 2\theta}{2} + \mathcal{O}(\phi.\psi) + \mathcal{O}(\theta\psi^2) \\ A^{1,2} = & \delta \sin 2\psi + \mathcal{O}(\theta\phi) + \mathcal{O}(\psi\phi^2) + \mathcal{O}(\psi\theta^2) \end{array} \right. . \tag{2.19}$$

Euler equation in the linear approximation

One can obtain the equation of motion for ϕ, θ and ψ using the Euler equation:

$$\boldsymbol{I}.\dot{\vec{\omega}} + \vec{\omega} \times (\boldsymbol{I}\vec{\omega}) = \vec{M}, \tag{2.20}$$

where $\boldsymbol{I}$ is the inertia matrix and $\vec{\omega}$ the angular velocity. In the general case this equation is non-linear: products of different Euler angles arise from the expression of the angular velocity, from the cross product in the Euler equation and from the $A^{i,j}$ coefficients.
Here we do not attempt to solve it exactly: our approach to the problem is to demonstrate we can obtain angular confinement with simplified equations, numerical simulations later showed effective confinement in a more general case [116]. It should be noted that we proceeded while knowing that the orientation of a levitating particle was experimentally stable, and varied with the trap parameters (see section 3.3). We also later confirmed this through observation of the harmonic motion for the three angles of rotation of a levitating particle.
The simplified equations are obtained by discarding the terms with mixed Euler angles and assuming small rotations around the equilibrium position. They can also be obtained in the 2D case, as treated in [73], by considering one rotation frozen (about the Z axis *eg*), a symmetry of the particle about this same axis and that the principal axis of the particle are the trap axes when the particle is at its equilibrium position.

Here we assume that the particle undergoes small rotations along its equilibrium positions and simply discard the terms with mixed Euler angles. A strict mathematical demonstration would therefore require further work to demonstrate that such terms can be neglected. We also assume the principal axes of the particle are the rotating frame axes, which can be justified if the spatial charge and mass distribution are identical or *eg* have the same symmetries.
Under such assumptions, the angular velocity along each axis of the rotating frame is the derivative of the corresponding Euler angle and the Euler equations yield:

$$\begin{cases} I_X\ddot{\phi} = & \frac{QV(t)\eta_z}{2z_0^2}\left(3+\delta\right)S_X\phi \\ I_Y\ddot{\theta} = & \frac{QV(t)\eta_z}{2z_0^2}\left(3-\delta\right)S_Y\theta \\ I_Z\ddot{\psi} = & \frac{QV(t)\eta_z}{z_0^2}\delta S_Z\psi \end{cases} \tag{2.21}$$

These equations are Matthieu equation, as presented in equations 2.3 or 2.4, with dimentionless parameters:

$$\begin{cases} a_\phi = & 2\frac{QV_{dc}\eta_z}{z_0^2\Omega^2}\frac{(3+\delta)S_X}{I_X} \\ q_\phi = & \frac{QV_{ac}\eta_z}{z_0^2\Omega^2}\frac{(3+\delta)S_X}{I_X} \end{cases}, \begin{cases} a_\theta = & 2\frac{QV_{dc}\eta_z}{z_0^2\Omega^2}\frac{(3-\delta)S_Y}{I_Y} \\ q_\theta = & \frac{QV_{ac}\eta_z}{z_0^2\Omega^2}\frac{(3-\delta)S_Y}{I_Y} \end{cases}, \begin{cases} a_\psi = & 4\frac{QV_{dc}\eta_z}{z_0^2\Omega^2}\frac{\delta S_Z}{I_Z} \\ q_\psi = & 2\frac{QV_{ac}\eta_z}{z_0^2\Omega^2}\frac{\delta S_Z}{I_Z} \end{cases}. \tag{2.22}$$

The three Euler angles therefore behave as the position of the particle: when the dimentionless parameters are within the stability region, the Paul trap confines the orientation of the particle around its equilibrium position. For each Euler angle $\alpha = \phi, \theta, \psi$ we therefore have a harmonic confinement:

$$\begin{aligned} U_{\text{rot}}\left(\phi,\theta,\psi\right) &= \sum_{\alpha=\phi,\theta,\psi}\frac{I_\alpha}{2}\omega_\alpha^2\alpha^2 \\ \omega_\alpha &= \sqrt{a_\alpha = +\frac{q_\alpha^2}{2}}\Omega, \end{aligned} \tag{2.23}$$

and the particle undergoes librations at such frequency for each of the corresponding axes. One should note that the electric torque can at a given time have the same sign for all three axes of the rotating frame, depending on the particle's orientation and geometry. This is forbidden for the electric force due to the Laplace equation for the CoM and will in turn change the shape of the stability diagram.

Optimization of the confinement

The strength of the angular confinement is a key parameter in several experiments: either for reaching the resolved sideband regime of the spin-mechanical coupling (see section 4.4) or simply to have a sufficient angular stability to cope with strong parasitic fluctuating torques (see section 3.3.2).

Let us here focus on increasing the confinement around the X rotation axis. If we vary the Paul trap DC field and AC frequency in order to keep the a and q parameters at the same value a_0 and q_0 -within the stability region for all degrees of freedom- the confinement frequency can be rewritten:

$$\omega_\phi = \underbrace{\sqrt{\frac{q_0^2}{2} + \frac{a_0}{q_0}}}_{\text{stability}} \underbrace{\sqrt{\frac{(3+\delta)\, V_{ac}\eta_z}{z_0^2}}}_{\text{Paul trap}} \underbrace{\sqrt{\frac{QS_X}{I_X}}}_{\text{particle}}. \tag{2.24}$$

We distinguish three contributions: the stability parameters, bound by the stability region, the Paul trap parameters and the particles charge and geometry. The Paul trap parameters V_{ac}, z_0 and δ can be tuned to increase the confinement frequency ω_ϕ but technical limitations will set an upper bound. The Paul trap should not be smaller than a few tens of microns in order not to be too sensitive to fluctuating charge patches [117], by definition $\delta < 2$ and reaching a voltage higher than a few thousands volts at high frequencies will be challenging. The intrinsic parameters of the diamond particle are then the only parameters that can be tuned.

First of all, for a given particle geometry, confinement increases with the number of charge. With dielectric levitated particle, the usual assumption is that there are charge patches trapped on its surface, with a total excess charge that can either be positive or negative. In experiments where diamond nano or micro particles are levitated in a Paul trap, the charge to surface ratio strongly depends on the injection technique. Electro-spray [118] yields the highest charge with, depending on the experiment, a charge to surface ratio from 300 electrons per square micrometer for micro clusters of nanodiamonds [65] to 20000 electrons per square micrometer for single nano-diamonds [52]. Using dry injection of micro-diamond we reach in our experiment about 15 charges per square micrometer. It should be noted that those are crude estimation: usually only the charge to mass ratio is directly measured and the charge is obtained using an often imprecise estimation of the mass.

The geometry and size of the particle then play a crucial role in confinement through the inertia momentum I_X and the S_X parameter. Regarding the size: from equation 2.24 and assuming a constant surface charge density, we can expect the confinement to scale as $\mathrm{d}^{-\frac{1}{2}}$ where d is the size of the particle. One should therefore be able to reach higher confinement frequencies with smaller particles. Finally confinement is impacted by the

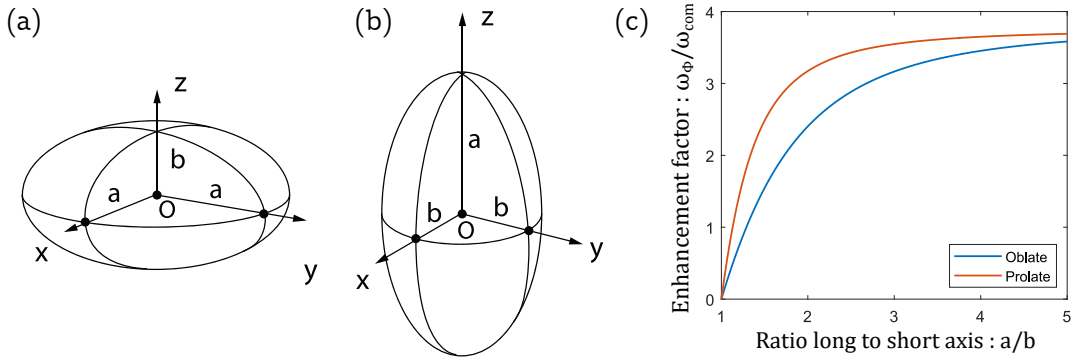

Figure 2.5: Ellipsoid of revolution with rotation symmetry around the Z axis. For the oblate ellipsoid a) the long axis a is in the XY plane while for the prolate b) it is along the Z axis. c) Ratio of angular to CoM confinement depending on the aspect ratio of ellipsoids of revolution.

spatial distribution of the charges compared to the mass: confinement is higher if the charges are distributed at the extrema of the particle, but the more elongated its shape is, the higher the inertia momentum gets, reducing the frequency of the confinement.

To gain insight into how the confinement depends on the shape, we consider particles with regular shapes: spheroid (ellipsoid of revolution) described in figure 2.5, both prolate and oblate. Because we do not know how the charges are distributed and have no control over it, we assumed homogeneous charge distribution and calculated confinement for different aspect ratios. Results are showed in figure 2.5.c) where we plot the enhancement factor *ie* the angular confinement over the center of mass confinement for both oblate and prolate ellipsoids of revolution as a function of their aspect ratio. We see that although the relative confinement increases with the asymmetry of the particle its enhancement saturates at about 3.7 .

Hybrid particle for enhanced confinement

To further increase angular confinement, one can resort to a more advanced engineering of an asymmetric charge distribution. First, the diamond surface could be functionalized to change its electrical properties and allow a higher surface charge density. Then one could also use another material lighter than diamond and assemble a hybrid particle composed of a small diamond and a strongly elongated light and highly charged particle. Because the shape and size of the diamond also impact NV spin properties within the diamond and the spin-mechanical coupling rate, this will be further discussed in section 4.4. One can also envision discharging or charging the diamond locally through photo-ionisation [119], electron bombardment [120] or small corona discharges [52, 121] to increase the charge asymmetry. One could further use an additional force and torque to confine the particle: for example if the charge distribution has a strong dipolar moment, adding a uniform non-varying electric field would provide angular confinement. Adding an electric field will however also displace the center of mass away from the minimum of the Paul trap potential. This shift should therefore be compensated by an additional force to limit the micro-motion of the particle.
An other option is to use a hybrid trap where the particle is levitated using the Paul trap while its angular degrees of freedom are confined by another force. In chapter 5, we

demonstrate an increased confinement using a magnetic torque.

2.2 Trap set-up

Let us start by describing the trapping apparatus. An ion trap typically consists in electrodes that are placed at an oscillating potential generating a time-varying quadrupolar electric field. In the adiabatic regime, this provides a ponderomotive force that brings charged particles at the minimum of the electric field's intensity [9]. While we explained the concept and principle of this ponderomotive force in section 2.1.1, we here focus on the experimental set-up and parameters. Because the charge to mass ratio of a micro or nano-particle is much smaller than the one of an ion, confinement is considerably weaker. This led us early on to work with smaller electrode, higher voltages and lower frequencies than what is typically used in the ion trap community.

Overview

We first give an overview of the trap set-up before going into a more detailed explanation for specific parts. Figure 2.6 depicts the overall system. An electrode (typically a ring) is used to levitate micro-diamonds by applying a high oscillating voltage between the trap electrode(s) and the ground (typically 2000 V at 4 kHz). The electrodes (geometry and fabrication) and the applied voltage are discussed in section 2.2.2 and 2.2.4 respectively.

We use an optical set-up to observe and measure the motion of the particle. A 4 mW 532 nm green laser is focused close to the particle using an aspheric lens. Its intensity can be tuned using a halve-wave plate followed by a polarization beam splitter and it can be chopped using an acousto-optic modulator. The trapped particle can be monitored through phase-contrast imaging: as described in section 2.2.1 when laser light transmitted by the particle is projected on a screen we can observe an image similar to a shadow. Retro-reflected light scattered by the levitating particle also allows us to measure the particle dynamics using an additional set-up described in section 2.3.

Both the trap and the lens are encapsulated in a vacuum chamber (or in a cardboard box for the early stages of the experiment). Injection of particles is accomplished under atmospheric pressure in the opened vacuum chamber by approaching a metallic wire covered with micro-diamonds close to the trap. As explained in section 2.2.3, Coulomb forces allow for charged diamond particles to be expelled from the wire and eventually confined in the trap.

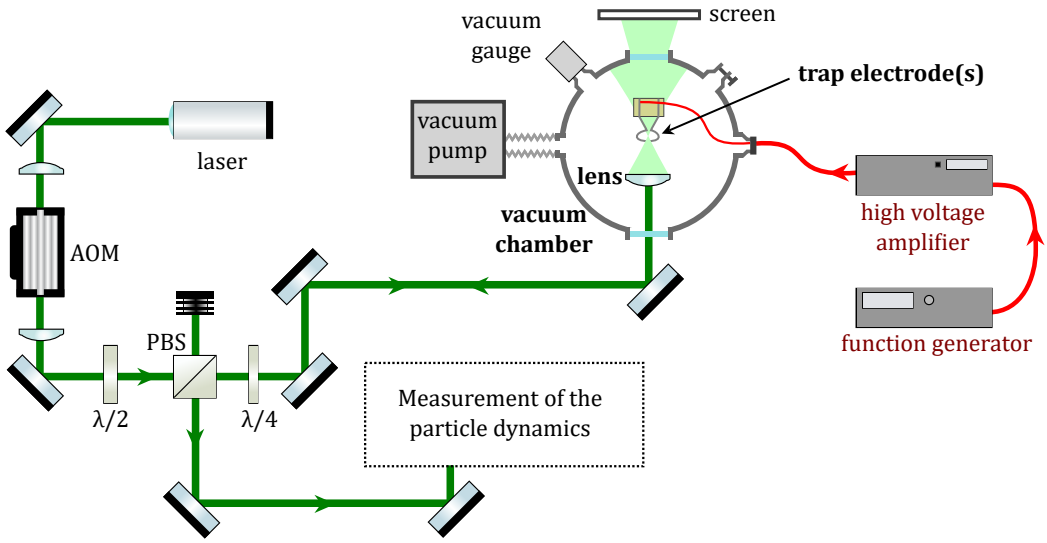

Figure 2.6: Overall set-up for micro-diamond levitation. Levitating particles can be monitored by phase contrast imaging from the laser light projected on a paper screen. To measure the dynamics of the particle, an additional set-up described in section 2.3 is used. The vacuum chamber is equiped with three windows (front, back and top). The air is pumped through a flexible tube connected to a turbomolecular pump while the pressure is monitored by a vacuum Gauge. AOM: acousto-optic modulator, PBS: polarization beam-splitter, $\lambda/2$ and $\lambda/4$: halve and quarter-wave plate.

2.2.1 Diamond visualization

Phase contrast imaging is employed to visualize the levitating diamonds. Phase contrast imaging simply takes advantage of differences in optical refractive index to visualize structures. In our case it allows us to observe micro-diamonds distinctly: because of the high refractive index of diamond ($\sim$2.5) the contour of the 2D projected image of the diamond appears darkened. Figure 2.7.b) shows a typical image of a levitating micro-diamond captured by a commercial camera.

The experimental scheme producing this image is depicted in figure 2.7.a). We use an aspheric lens (NA=0.77 LightPath 355330 or NA=0.5 C240TMD from Thorlabs) to focus laser light in front of the levitating diamond and simply place a screen behind the latter. Rough optical alignment is typically done while monitoring the phase contrast image by direct visual observation of the screen.

Note that several interferences features might be observed because we use a coherent light source. This can be seen on the edges of a micro-diamond, or on a nano-diamond, which displays concentric circles. Speckle patterns due to interferences in the reflected light also turned out to be key for the measurement of the diamond motion as will be detailed later in section 2.4.2.

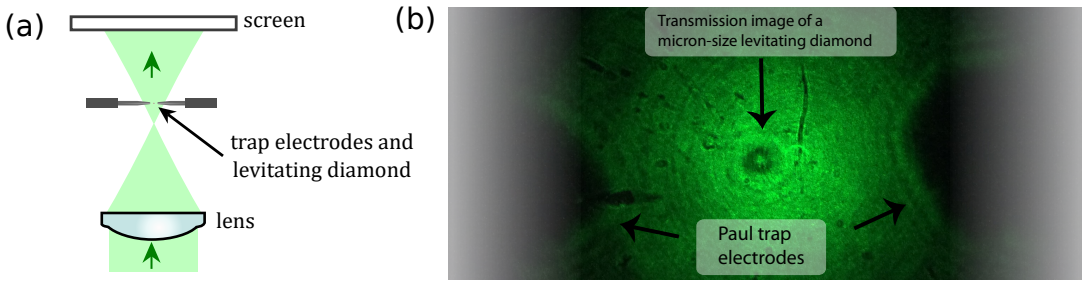

Figure 2.7: a) Schematics of the visualization system: an aspheric lens focuses a green laser in front of a levitating particle. The laser light is projected onto a screen for visual observation of phase contrast images. b) Phase contrast imaging of a single levitating micro-diamond and shadow of the trapping electrodes (endcap trap). The various spots on the lens are the diamonds that did not make it to the center of the trap and ended up on the surface of the aspherical lens. Here it lies 3.1 mm below the trap.

Another useful tool to adjust the trap settings is to chop the light source at a frequency close to the frequency of the oscillating Paul trap potential. This stroboscopic illumination of the particle allows visual observation of the periodic micro-motion of the particle even if it is too fast to be directly perceived by the naked eye. The micro-motion is caused by external forces, which shift the center of the Paul trap from the zero of the electric field. It should be minimized, in particular to obtain a sharp image of the particle. The trap parameters are first often adjusted to reduce micro-motion using this method.

2.2.2 Trapping electrode(s)

A number of geometries can be used for the trap electrodes, we use a simple ring or two needles in front of each other in the so-called Paul-Straubel and endcaps geometries [111]. It should be noted that any electrodes configuration which is symmetric with respect to the XY, XZ and YZ planes will generate the desired electric potential:

$$\phi(x,y,z,t) = \frac{V_{ac}\cos(\Omega t) + V_{dc}}{z_0^2}\left(\eta_x x^2 + \eta_y y^2 + \eta_z z^2\right) + \mathcal{O}\left(x^4, y^4, z^4\right). \tag{2.25}$$

where the additional fourth order terms can be neglected close enough to the trap center. Here the aspect ratio of the needle and rings are chosen to roughly minimize such anharmonic components [111].

Endcap configuration

Figure 2.8.a) shows the trapping electrodes in the endcap configuration. Two tungsten needles with a radius of curvature of ∼25µm are aligned in front of each other, separated by a distance $d = 2z_0$ of about 100µm. They are surrounded by an uncritical ground electrode structure composed of our collection lens mount a few millimeters away and diverse mechanical components a few centimeters away. When Electron Spin Resonance (ESR) is carried out on NV spins within a levitating diamond (see section 3.2), a micro-wire is brought a few hundreds micrometers from the trap center to drive the spins. The trapping parameters then need to be adjusted as the trapping potential is modified by the proximity

of a ground electrode and to avoid electric arcs (see section 3.2, also table 2.1).

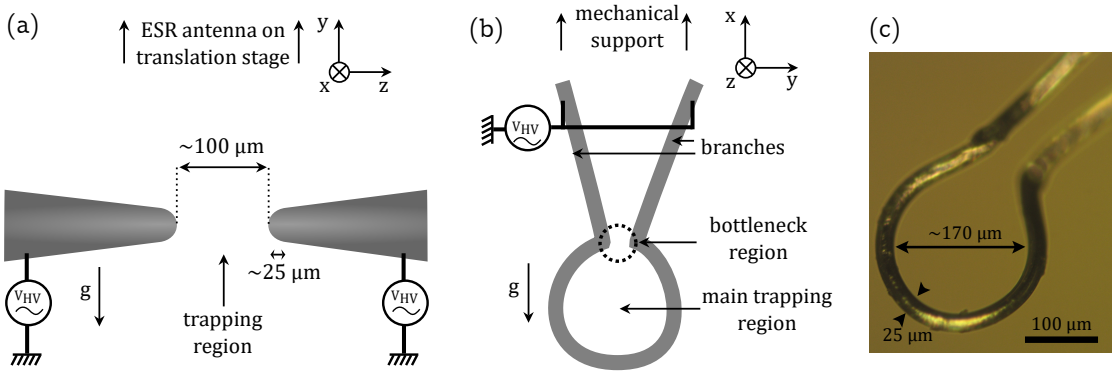

Figure 2.8: a) Needle electrodes: two needles with the trapping voltage applied to both electrodes. An ESR antenna can be approached from the top to control NV spins. b) Ring electrode: a tungsten wire producing a near-torus shape, opened at the top (bottleneck) where two branches of the wire depart from the ring following radial trajectories. Both the center of the ring and the bottleneck region provide stable trapping. The trapping voltage is applied at both end of the wire and a microwave current can be injected in the ring to control NV spins. c) White light microscope image of a tungsten micro-ring.

Ring geometry

The ring electrodes are near-torus structures hand-made out of a single wire (see annex A for details on the fabrication procedure). Figure 2.8.b) depicts its shape and figure 2.8.c) shows a microscope image of an actual trapping ring. The wire forms a ring, slightly opened at the upper extremity where the two branches of the wire deviate from the ring and follow radial trajectories instead of joining each other. The extremity of these branches is eventually used to hold the whole structure. As detailed in section 3.2 such ring can be used not only to generate the trapping potential, but also to generate the microwave field driving the NV spins.

Importantly, we noticed there is another region apart from the ring center where the electric potential is nearly harmonic so that stable trapping occurs: at the point where the two branches holding the ring almost join each other. We designate such region as the bottleneck and because the distance between the two branches of the electrodes is much smaller than the interior diameter of the ring, there are stronger electric fields resulting in a stronger confinement. Moreover the asymmetry of the trapping field is higher than at the center of the nearly symmetric ring. This will result in an enhanced confinement of the angular degrees of freedom (librational modes) compared to the center of mass (higher δ in equation 2.22 of section 2.1.2).

The size of the rings that we use ranges from several millimeters to about 120 µm for the interior diameter and depends on the intended confinement: a smaller ring yields a higher potential curvature through higher η/z_0^2 parameters. Table 2.1 presents an overview of the different trap geometries and parameters that we used for the experiments carried out. Note that because our fabrication procedure is not reproducible, confinement also varies from one ring to another depending on their shape, even if they have the approxi-

mate same size.

2.2.3 Injection of micro-particles in the Paul trap

Injection procedure

Injection of micro-diamonds in the Paul trap is accomplished through a dry, low-yield, atmospheric pressure method presented in figure 2.9.a). A metallic wire is used to bring micro-diamonds in the vicinity of the trapping electrode(s). The width of the wire that we use depends on the fragility of the trap: 25µm for micro-ring or 150µm for bigger trapping electrodes. The tip of the wire is dipped into a large quantity of micro-diamonds (in the form of a dry powder) so that large clusters of micro-diamonds are stuck on its surface (see figure 2.9.a)). This method can pick-up a large enough quantity of micro-diamonds from large volume of material but also from a few millimeter squares of a single layer of micro-diamonds laying on a glass coverslip (see section 5.3).

The tip of the wire is then approached to the trapping electrode: either close to the tip of the needles of an endcap trap or hundreds of microns above the bottleneck with a ring trap (see figure 2.9.a)). This is done manually by holding the -insulated- other end of the injection wire. When the trap voltage is turned on, charged diamonds will be ejected from the tip and if the trap is stable, some micro-diamonds can be captured by the trap and optically detected (see below). Electric arcs may form between the injection wire and the trapping electrodes and the two of them might come into contact but trapping often occurs without those events happening.

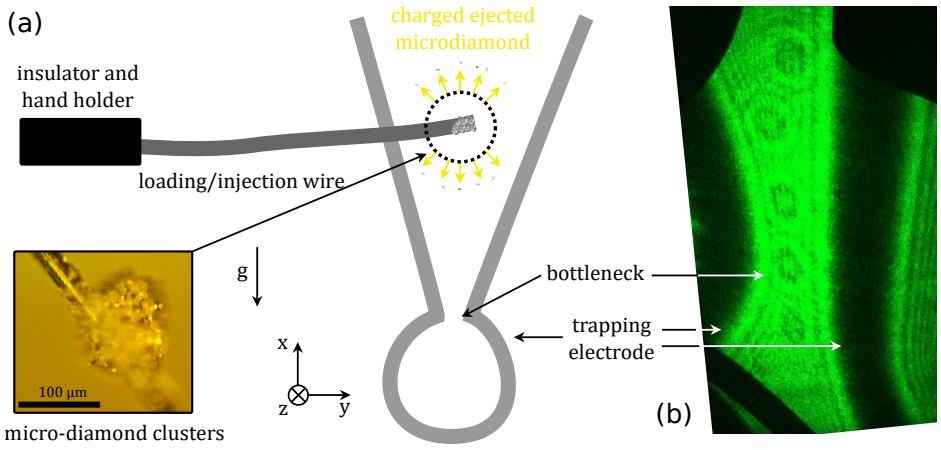

Figure 2.9: a) Injection of micro-diamonds in a ring trap. The tip of the injection wire was prealably dipped in micro-diamonds powder so it is covered in micro-diamonds clusters as can be seen under optical microscope in the bottom left caption. When the injection wire is brought close to the trapping electrode and the trapping voltage is on, charged diamonds are ejected and follow nearly random trajectories with some of them slowed down within a stable trapping region. b) Phase contrast image of several micro-diamonds trapped in the bottlenech region and above. Particles can also be trapped below, near the center of the ring. The shadow of the trapping electrode as well as diverse mechanical elements can also be seen.

The injection method that we use has a low yield, so we need a relatively large supply of micro-diamonds. As an order of magnitude, 50 mg of 15 µm diamonds is sufficient to carry experiments for several months, with several daily injections in the trap. In order to produce large quantities of micro-diamonds, the usual method is to mill a bulk diamond. Our most common micro-diamond sample originates from bulk diamonds made at high pressure and high temperature (MSY from microdiamond). They are sold as powders of different micro-diamond sizes, we use sizes ranging from 500 nm to 10 µm.

Physical mechanism

We have not exhaustively studied the injection mechanism but it can be understood by basic mechanical and electric considerations. We propose two non mutually exclusive explanations for the ejection of charged diamonds from the tip as it is brought in the strong electric field, close to the center of the trap. First, the tip and the diamond clusters on it can be capacitively charged and the excess charge can break the cluster apart when repulsive Coulomb forces overcome van der Waals forces. Second, we observed on a glass coverslip that a strong electric field can break apart micro-diamonds clusters, it is therefore possible for the electric fields to polarize and break clusters at the tip of the injection wire. Once clouds of charged micro-diamond are dispersed around the trapping electrode some of the micro-diamonds -slowed down by air damping- will be captured by the Paul trap.

Interestingly, when using our ring electrodes we noticed diamonds can be trapped into the bottleneck as explained in section 2.2.2 but also above, in between the two branches holding the electrode with sometime a chain of trapped micro-diamonds. The geometry can indeed be assimilated to linear Paul traps -usually build of four rods placed at the vertices of a square, with the trapping voltage applied between adjacent rods. Here the two branches provide confinement in the YZ plane (see figure 2.9) while gravity and repulsive Coulomb forces provide confinement along the x axis. Figure 2.9.b) shows a phase contrast image of a chain of trapped diamonds in and above the bottleneck of a ring electrode. Such observation points towards the branches and the bottleneck as playing the role of a guide for charged micro-diamonds toward the bottleneck and the center of the ring, thus increasing the injection yield.

This loading method gives us a reliable and simple way to load the diamonds as each trapping run only requires one minute on average. This loading technique further provides a charge to mass ratio that enables trapping of the diamond particles for several days under ambient conditions. Other potential injection methods are described in section 2.1.2.

2.2.4 Tuning the stability and confinement of the Paul trap

In order for injected charged diamonds to remain in the trap, its parameters must be correctly tuned. Let us rewrite the formulas from section 2.1.1 for the stability dimensionless parameters and confinement along a direction u:

$$\begin{cases} a_u = \dfrac{4\eta_u}{z_0^2}\dfrac{V_{dc}}{\Omega^2}\dfrac{Q}{m} \\ q_u = \dfrac{2\eta_u}{z_0^2}\dfrac{V_{ac}}{\Omega^2}\dfrac{Q}{m} \end{cases}, \qquad \begin{aligned} \omega_u &= \sqrt{a_u + \frac{q_u^2}{2}}\Omega \\ &= \sqrt{\frac{4\eta_u}{z_0^2}V_{dc}\frac{Q}{m} + 2\left(\frac{\eta_u}{z_0^2}\frac{V_{ac}}{\Omega}\frac{Q}{m}\right)^2}. \end{aligned} \tag{2.26}$$

Stable trapping in the three directions first requires the a and q stability parameters to be within a bounded region, with in particular $|a|, |q| < 1$ (see section 2.1.1 for details). The charge to mass ratio Q/m is determined by the injection mechanism and the η_u/z_0^2 factor by the trap geometry. For a given electrode and injection method, the amplitude (V_{ac}), frequency (Ω) and bias (V_{dc}) of the voltage must therefore be tuned to allow stable trapping.

Note however that because the confinement strength diminishes with the a and q stability parameters, gravity or stray electric fields might pull the particle out of the trap if a and q are too low. There hence exists only a finite window of parameters for which a given particle can be trapped. The width of this stable window varies with the particle type, the trapping electrode and the maximum amplitude of the tension.

Table 2.1: Shape and size of the trap electrodes and trap parameters used for different experiments carried out. Size, amplitude voltage and frequency of the trap are only rough indicative values as they change from one trap to another and depends on the -variable- charge to mass ratio of the trapped particle.

Experiment		electrode	size	pressure	frequency	voltage
Injection, trapping, observation		ring	5 mm	P_{atm}	50 Hz	6000 V
[74]	trapping	needles	100 µm	1 Atm	2-6 kHz	2000 V
	splitted ESR	+ antenna			1-3 kHz	600 V
[122]	zero-field ESR	ring	700 µm	1 Atm to 0.01 mbar	1-3 kHz	600 V
[75]	zeeman splitted ESR Rabi, Ramsey, echo	ring	180 µm	1 Atm	3-6 kHz	2000 V
				1 mbar	1-3 kHz	600 V
[77]	zeeman-splitted ESR Spin-dependent torque Bistability	bottleneck	$\sim$ 30 µm	1 Atm	3-6 kHz	2000 V
	Spin-cooling Spin-lasing Spin-spring			1 mbar	1-3 kHz	600 V

Typical voltage used

We generally use an AC voltage with only a small DC offset. The amplitude and frequency of the AC tension is highly variable and depends on the geometry and size of the trapping electrode as well as on the experimental conditions. A small DC offset is added when a higher confinement along a specific direction is required, for example to reduce micro-motion due to an external force.

Usually we use a high voltage and high frequency during the injection to both maximize the ejection of charged particle from the injection wire and trapping of only the most charged particle, the trap thus acts as a filter for the charge to mass ratio. Once a particle is trapped, parameters are adjusted depending on the experiment carried out. In order not to loose the particle, both amplitude and frequency are smoothly changed in opposite ways and a DC tension might be added to compensate stray electric fields or

gravity. When using needle electrodes the distance separating them can also be decreased to increase the electric potential curvature.

Table 2.1 gives an overview of the range of amplitude and frequency used depending on the size of the electrode and the experiment. Vacuum conditions typically requires amplitude as low as 600 V to avoid forming a plasma when pressure is lowered. The same goes if one uses an additional antenna brought close to the trap to prevent electric arcs from forming between them.

Instability onset

When the trap is unstable because the a and q stability parameters are too high, the particle follows oscillation of increasing amplitude until it escapes from the trap or hit the trap electrodes. Under atmospheric conditions, damping however enlarge the stability region and tempers the onset of the instability. Instead of oscillations of increasing amplitude, the particle describes large but bounded oscillations similar to micro-motion.

This motion is often observed when the parameters of the trap are modified to increase confinement (increasing voltage or reducing the frequency). We noticed the instability appears more abruptly for an endcap trap (or at the bottleneck) than for a ring Paul-Straubel trap and noticed this is correlated with the sign of the trap anharmonicities [111]. In both cases it is however still possible to observe the onset of the motion instability without loosing the particle if we (very) slowly sweep the trap parameters while carefully monitoring the motion of the particle.

Charge to mass ratio

Observation of the instability provides us with a means to determine the charge to mass ratio Q/m of the levitating particles: as equation 2.26 shows, Q/m is a critical factor for confinement and stability of the Paul trap. In particular, it depends on the injection method as discussed in section 2.1.2. In order to measure it, we perform a slow ramp of the trap frequency downwards from 4 kHz to a few kHz. As the stability factor q increases, the trapping eventually becomes unstable at $q \sim 0.9$ and we can then infer Q/m. The first observed instability corresponds to the highest confinement frequency ω_z. We measured it to be about 1 kHz for diamonds that have a 10 μm diameter in a needle trap. Using the stability criterion, the diamond density and an estimation of the field generated by the trapping electrodes, we can extract the total charge on the surface of the levitated particle. The stability parameter q_{max} is 0.908 in our case ($a \sim 0$), and relates to $|Q_{\text{tot}}|/m$ via the formula

$$|Q_{\text{tot}}|/m = \frac{q_{\text{max}}}{4\xi}\Omega^2$$

where ξ is the curvature of the static electric potential. We obtain $\xi = 2 \times 10^6\ V/m^2$ from 3D simulations of the electric potential of our trap, so the total number of elementary excess charges $|Q_{\text{tot}}|$ in the diamond is about 5000.

We also measured the sign of the total charge by adding a constant voltage to the needles. Due to residual static electric fields, the particles are slightly displaced from the zero of the oscillating electric field. Adding an extra DC voltage corrects or amplifies this

displacement depending on the relative sign between the voltage and the excess charge of the particle. Applying a positive voltage on more than 20 different particles systematically displaced them towards the trap center needle, letting us conclude that the total surface charge is very often negative.

2.2.5 Vacuum conditions

It should be noted that although particles are levitated, they are far from being insulated due to the background gas: all the experiments presented until now are carried under atmospheric pressure. In order to harness the mechanical properties of our levitation system, one must work under vacuum conditions to reduce damping and brownian motion caused by collisions with gas molecules. Although we eventually want to work under high vacuum, as a first step we aim at accessing the underdamped regime where the damping rate is lower than the frequency of the mechanical oscillator. In our case this can be achieved at a relatively low vacuum, in the mbar range.

For any vacuum condition experiments, we proceed by first trapping a particle under atmospheric pressure before (slowly) pumping out the air. Note that it is possible to inject particles in a Paul trap already under high vacuum [123], here the procedure we perform is well suited for moderate pressure ($10^{-2} - 1$ mbar), with one successful iteration taking between 10 and 30 minutes only.

Equipment

When vacuum conditions are required, the Paul trap as well as the collection lens is placed within a custom-made vacuum chamber (from Neyco). A vacuum pump composed of a primary pump and a turbomolecular pump is connected to the chamber through a flexible tube. The pressure within the chamber can be lowered to below 10^{-3} milibars within hours starting at atmospheric pressure and without any heat treatment or specific cleaning procedure for elements within the chamber. A vacuum Gauge is directly connected to the chamber to monitor the vacuum pressure and an exhaust valve is available to restore atmospheric pressure.

Breakdown voltage

As the pressure is lowered, the voltage needs to be lowered to 600 V to avoid plasmas that would otherwise appear in the chamber as the breakdown voltage, which follows Paschen's law [124], is lowered. Since this systematically leads to a lowered confinement, a preselection of particles with a high charge to mass ratio can be performed at atmospheric pressures to compensate. The whole procedure typically requires 3 to 4 loading steps before a high enough charge to mass ratio is attained. Once a particle is trapped, the voltage and frequency are lowered in air, following an iso-q curve. Once 600 V is reached, the turbomolecular pump is turned on.

Impact of vacuum conditions on the trapped particle

We observed both in transmission and by looking at the back-scattered green light that when the pressure reaches 500 mbars already, the center of the trap shifts. This takes place because of two cummulative effects. First the secular frequency depends on the damping rate, *i.e.* on the vacuum level [114, 125]. In the presence of residual electric fields or gravity, changing the confinement via the damping rate displaces the particle. Secondly, vacuum conditions might alter the surface of the trapped diamond [64] and may cause a change in the charge to mass ratio. The observed displacement has both a reversible and an irreversible part which prompted us to consider both effects.

When using a low confinement trap (*eg* larger ring), the back-scattered image of the diamond also appeared elongated in a direction perpendicular to the optical axis, consistant with a large amplitude of the micromotion. When the damping rate decreases the particle indeed explores a larger volume away from the center of the trap so that micromotion increases.

Note that when the vacuum reaches 10^{-2} mbars, the voltage can be increased back to 4000 V without any arching in the chamber. In principle, the optimum voltage for high confinement and no arching, could be chosen by following the Paschen law [124].

2.3 Center of mass motion

Once the particle is stably levitated, we aim at observing its dynamics in order to eventually use it as a mechanical oscillator coupled to NV spins. This is typically done under vacuum conditions, in the underdamped regime where the damping rate is lower than the mechanical frequencies so that we can observe harmonic motion of the particle.

We first focus on the harmonic oscillations of the particle Center of Mass (CoM). As already mentioned, the mechanical modes that we are most interested with are the libration of the particle. Monitoring the CoM is however important, especially to ensure the levitated particle does not escape the trap. In order to observe the CoM modes, one can proceed either by exciting the CoM of the particle while observing its response or simply by observing spontaneous oscillations due to the finite temperature of the system, here determined by collisions with the background gas. Here we choose the latter method, we first describe our detection set-up before showing the results obtained in the underdamped regime.

Detection of the CoM motion

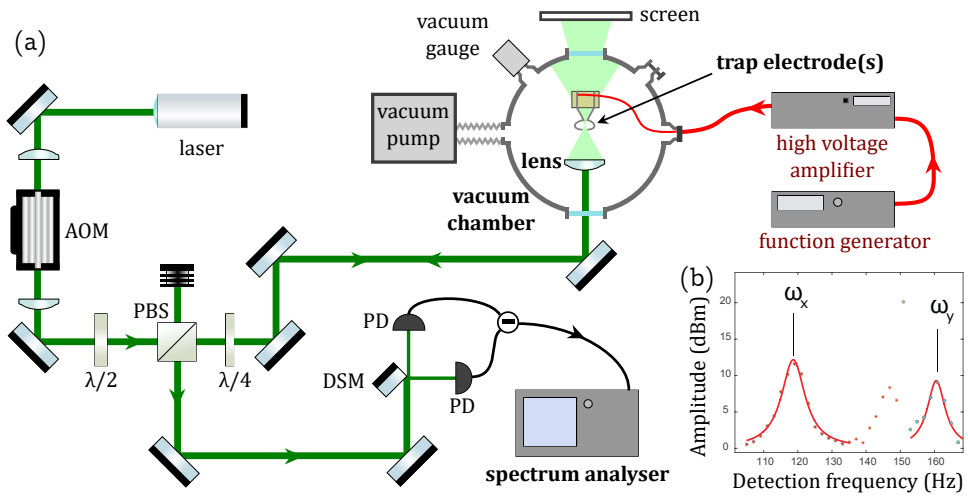

Figure 2.10: a) Trap set-up including detection of the CoM motion. DSM: D-shape mirror, PD: photo-detector. b) Power Spectral Density (PSD) of the CoM motion obtained from the spectrum analyser. The two mechanical modes of lower frequencies are labelled ω_x and ω_y.

Figure 2.10.a) shows the overall trap set-up, which was described in previous section, except for the part used to measure the dynamics of the particle. We use the retro-reflected light scattered by the levitating particle: it is first separated from the incident laser using an optical circulator composed of a $\lambda/4$ waveplate followed by a polarization beam-splitter. The light is then focused on the edge of a D-shape mirror and the reflected and transmitted light are measured by a dual photo-detector (PDB210A, from Thorlabs). The two signals are then subtracted and sent to a spectrum analyser (Keysight N9020A MXA). When the CoM of the particle moves, its image on the D-shape mirror is displaced, therefore changing the subtracted signal. Depending on the orientation of the D-shape mirror and of the trap axes relative to the optical axis, we can use this method to measure oscillations of the CoM along the three axes of the Paul trap.

Harmonic CoM oscillations

Figure 2.10.b) shows the Power Spectral Density (PSD) of the CoM motion of a levitating diamond acquired on a spectrum analyzer. This spectrum is taken at 0.5 mbar at 300 V of trap voltage and 1.12 kHz of trap frequency. We distinguish two peaks, which varies with the trap parameters, the peak in-between is at a multiple frequency of 50 Hz and is an artifact. Here the third most confined trap axis is along the optical axis and the sensitivity of our detection scheme to motion along this axis is diminished, therefore preventing us from observing this mode on the spectrum.

The observation of these modes enables useful technical implementations. In particular, one can use the detection of the position to cool down the CoM motion using an active feed-back loop that applies a force proportional to the velocity through the trap electrodes [52] (parametric feed-back [51]) or through an additional electrode (cold damping [54, 126]). This method can allow for cooling the CoM modes to about a dozen

phonons [54]. Since we are here interested in the angular motion, this method would be implemented for example to prevent heating of the CoM modes. Such heating could result in the particle escaping the trap or to heating of the angular degress of freedom through coupling with the CoM modes. Although the means to apply parametric feedback cooling or cold damping have been established, we have not performed it yet and it should be the subject of future work.
These peaks also give relevant informations regarding the external temperature, *ie* temperature of the CoM modes [53]. Note that measurement of the absolute temperature however requires a calibration of the measurement. It is typically obtained by observing the PSD at high enough pressure so that the external temperature does not depend on the pressure and is equal to the gas temperature (∼300 K) [53]. A strong limitation to the use of such a technique in our experiment is that the position of the particle can drift when the pressure is lowered (see section 2.2.5), changing in turn the sensitivity of the position measurement as the optical alignment changes.

Amplitude of the micro-motion

When external forces are strong compared to the confinement of the Paul trap (*eg* ω_z), the center of the trap is shifted away from the zero of the oscillating electric field. This causes the so-called micro-motion (see section 2.1.1): the position of the particle oscillates at the frequency of the Paul trap Ω. In our case the micro-motion originates from gravity and stray electric fields generated by charge patches on the trapping electrodes. A large micro-motion will actually blur the optical image of the particle, which we use to measure the position of the particle.

The amplitude of the micro-motion can be monitored on the PSD of the motion, or simply using the phase contrast image of the particle while the green laser is chopped at a frequency close to Ω. This amplitude could be reduced by applying another external force to compensate the already existing ones. In our case we simply increase the confinement of the trap: for small ring electrodes we reach a confinement strong enough so that micro-motion does not impact our detection apparatus.

2.4 Angular confinement: the librational modes

Although our focus was initially the center of mass of the levitated particle, it turned early on towards the angular degrees of freedom as we noticed its confinement. First observation of the confinement were made thanks to the shape anisotropy of the particle through phase imaging and confirmed through NV magnetometry (see section 3.2) but we will here focus on the characterization of this confinement through optical means. We first discuss whether we can confirm its origin to be the Paul trap as described previously or if others are likely. We then present the set-up for detection of the angular degrees of freedom of the particle which allows us to observe librations of the particle under vacuum conditions.

2.4.1 Origin of the confinement

In section 2.1.2 we theoretically demonstrated the Paul trap can confine not only the center of mass but also the angular degrees of freedom of a levitating particle. There are in

fact several mechanisms that could stabilize the angular degrees of freedom as well. For example if the charges distribution of the trapped particle has an electric moment, a static electric field introduces a torque and can stabilize the particle rotation around at least two axes. This could in practice occur thanks to stray electric fields generated by charges patches on the surface of the trap electrodes. Another mechanism would be the effect of gravity (or any volume force) combined with a localized charge distribution on the trap particle. As long as the charges are not localized at the center of mass, the forces from the Paul trap will introduce a torque and the particle will be stabilized with most charges pointing upward. Currently, we cannot assert that the Paul trap angular confinement is always the dominating mechanism, but several observations point towards it being present and at least not negligible.

First, looking at elongated particles, one can visually observe micro-motion of the angular degree of freedom using the visualization methods described in section 2.2.1. Angular micro-motion consists of oscillation of the angular degrees of freedom at the frequency of the Paul trap voltage. It is key to the confinement generated by the Paul trap but also means that external torques do displace the angular equilibrium position away from the bottom of the trap.

A second observation consisted in observing a change of the orientation of a levitating micro-diamond as the trap frequency was modified. We can see this on the phase contrast image that is seen rotating, but it was also confirmed using NV magnetometry to measure the particle orientation with respect to the magnetic field (see below, section 3.3). It is tempting to conclude from this experiment that the shift of the orientation of the particle is caused by a change of the dominant confinement mechanism, from the Paul trap to another one. There are however loopholes to this reasoning: when the frequency of the trap changes, the trap center is also shifted (if external forces are not fully compensated). This eventually changes the stray electric field felt by the particle and its resulting confinement as well. Further experiments are therefore required to fully settle this issue but it does not prevent us from taking advantage of the observed angular confinement.

2.4.2 Detection of the angular position

In previous measurements of the mechanical oscillator, we did not take into account the angular degrees of freedom of the particle: their aim was solely to measure a translation of the particle's CoM and the optical detection was aligned so that all other signals -considered as noise- were minimized. Here we describe an other set-up, similar but designed to detect the angular degrees of freedom.

Set-up

We can distinguish two ways for optical detection of the angular position of the particle. Overall, we make use of the anisotropy of the particle to modify the collected back-scattered light when the particle rotates. Since the particle (typically 10 µm size) is much bigger than the wavelength (532 nm) we can use the anisotropy from its overall shape but we can also use the anisotropy arising from the roughness of the particle's surface.

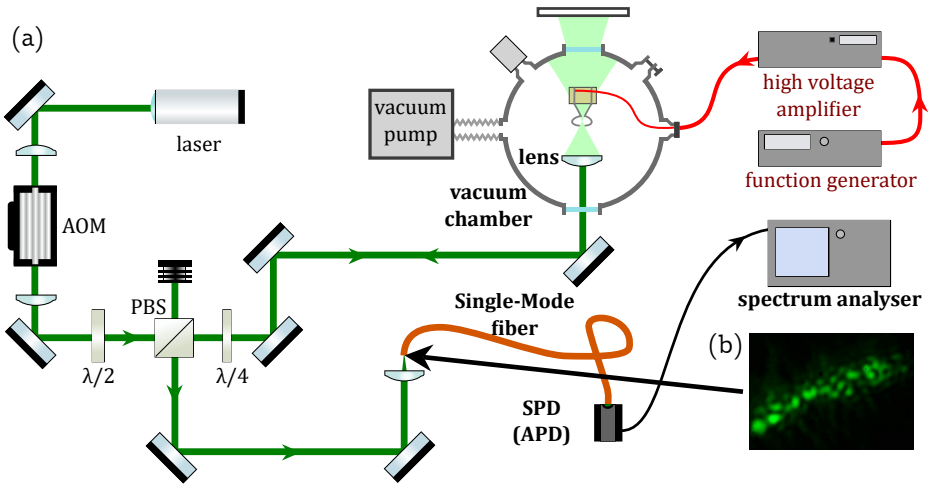

Figure 2.11: a) Trap set-up with detection of the angular position. PBS: Polarisation Beam Splitter, SPD: Single Photon Detector, APD: Avalanche Photo-Diode. b) Image of a levitated iron micro-rod obtained from the back-scattered light before the lens coupling it into the single mode fiber. Similar speckle patterns are obtained with levitated micro-diamonds.

Figure 2.11.a) depicts the set-up that we use. It is similar to the one presented for the CoM detection except we don't use a D-shape mirror but directly couple the back-scattered light into a single mode fiber and detect it using a single photon detector (APD SPCM-ARQ-15 from Perkin-Elmer). Here we however do not optimize the intensity of the collected light: in fact we take care not to focus the back-scattered light exactly into the core of the fiber. First of all, we misalign the position of the image of the levitating particle so that it is not centered on the core of the fiber. This breaks the symmetry around the optical axis and the collected light will vary depending on the orientation and shape of the particle's image.

Although this method allows us to track large rotation of the particle (as in section 3.3.2), one can further take advantage of the coherence of our laser combined with the roughness of the particle to obtain a more sensitive measurement. Figure 2.11.b) shows the image of a levitated particle before the lens that couples it into the fiber. Here the image is produced by an iron rod but similar features are observed with levitated micro-diamonds. Beside the elongated shape, we can see the intensity of the light varies due to speckle patterns, *ie* interferences between light scattered by the particle at different positions and different heights due to the material roughness. These speckle patterns can be used to detect the angular position by coupling only a bright -or dark- spot in the fiber. In order to do so, one can eclipse the rest of the image with a diaphragm of the right size. In practice it is however simpler to set the distance between the diamond and the collection lens such that the back-scattered light diverges. This way the lens before the fiber will only couple into the fiber a small area of the speckle patterns.

Sensitivity and calibration

This latter method, which exploits the interferences creating the speckle pattern, is very sensitive. However, it has the considerable drawback of yielding a sensitivity that is diffi-

cult to precisely calibrate. We therefore cannot relate our signal with an absolute angular position.
Optimization of the signal is realized either using thermal fluctuations of the angular degrees of freedom or a controlled pulsed excitation (usually a magnetic torque, see section 4.1 and 5.2). One can then check the linearity of the dependency of the signal on the angular position by exerting a controlled torque or observing harmonic oscillations, but the sensitivity itself is highly dependent on the surface that determines the speckle pattern and will vary with the three Euler angles, the CoM position and with the optical alignment.

Our best experimental estimation of the sensitivity is obtained using NV spin magnetometry: we measure a variation of 43 mrad between the magnetic field and the NV axis for a shift of the countrate of one MHz. Given our noise, this gives us a measured sensitivity of 0.29 mrad/$\sqrt{\text{Hz}}$ (see section 4.1.3). Note that since the rotation that we optically measure is not necessarily about an axis perpendicular to both the NV and the magnetic field axis, the exact sensitivity remains unknown.
We can also calculate a rough order of magnitude of this sensitivity with a simplified model of the speckle patterns. Let us assume a bright spot of the speckle pattern is produced by two scattering surfaces within the same diffraction spot (distant of $\sim$1 µm), at a height difference of λ compared to the wavefront of the laser. For a rotation other than about the optical axis, one can expect a complete extinction of this bright spot for a relative displacement of the two surfaces of $\sim \lambda/2 = 266$ nm. This corresponds to a displacement of roughly 0.25 rad, given the usual photon count rate at the outpout of our detector of 10 MHz (close to saturation) we obtain a sensitivity of about 0.1 mrad.$\sqrt{\text{Hz}}$, in the same range as the measured sensitivity.

2.4.3 Librational modes in the underdamped regime

The measurement of the angular position allows us to observe the librational modes *ie* oscillations of the angular degrees of freedom around an equilibrium position. As for the CoM modes, this can be done either by exciting those modes and observing the response of the mechanical oscillator or by simply observing the thermal fluctuations in the underdamped regime, where the damping rate is lower than the frequency of the oscillator. Although excitation through a magnetic torque was used to initially detect the librational modes, here we directly present the observation of the oscillator under thermal fluctuations.

Experimental observation

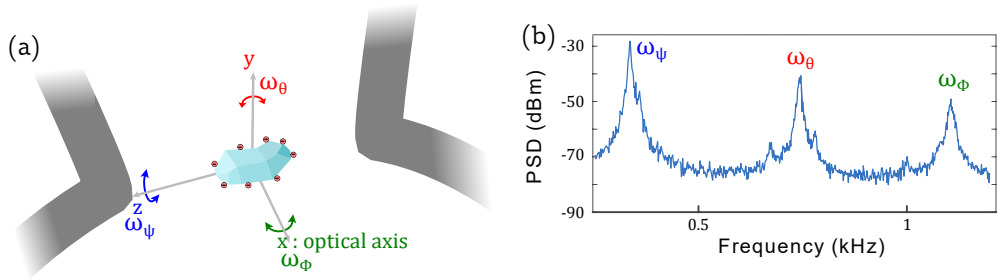

Figure 2.12: a) Representation of a levitated diamond in the bottleneck region of a ring electrode. The rotation of the particle is confined by harmonic potentials for all the three axes of the Paul trap (x, y, z). b) Power Spectral Density (PSD) of the collected speckle spot of the light backscattered by a levitating diamond. We associate each peak with librations along the most probable axis of the Paul trap.

Figure 2.12.b) shows the Power Spectral Density (PSD) of the angular position measured using speckle patterns under a pressure of 1.5 mbar. We use a 15 µm diamond levitating in the bottleneck region of a ring trap made of a 25 µm wire. The trap voltage is 600 V with trapping frequencies typically ranging from 2 to 4 kHz. We distinguish three peaks in the spectrum, ranging from 400 Hz to 1.1 kHz. Each of them corresponds to a librational mode for rotation about one axis of the Paul trap. These mechanical frequencies are consistent with confinement resulting from the Paul trap mechanism, with the trapping frequency Ω higher than the resulting confinement.

Model

We fit the power spectral density of the librational modes using equations derived from the following model, relying on linear response theory. We first treat each librational modes independently, here we therefore consider a single angle of rotation, assuming it does not couple to other angles.
Noting ϕ the angle between the equilibrium position of the diamond and its angular position, the librational motion is ruled by the equation

$$I\ddot{\phi} = -I\omega_\phi^2\phi - I\gamma\dot{\phi} + \Gamma_T(t) \tag{2.27}$$

where I is the moment of inertia, ω_ϕ is the angular frequency, γ is the damping rate due to collisions with the background gas and $\Gamma_T(t)$ is the associated Langevin torque.

Fourier Transforming this equation yields

$$\phi(\omega) = \chi(\omega)\Gamma_T(\omega),$$

where

$$\chi(\omega) = \frac{1}{I(\omega_\phi^2 - \omega^2 + i\omega\gamma)}.$$

The Langevin torque $\Gamma_T(t)$ obeys the relation

$$\langle \Gamma_T(\omega)\Gamma_T(\omega')\rangle = 2\pi\delta(\omega+\omega')S_T(\omega)$$

where

$$S_T(\omega) = -\frac{2kT}{\omega}\mathrm{Im}\Big[\frac{1}{\chi(\omega)}\Big].$$

We therefore have

$$S_T(\omega) = 2kT\gamma I.$$

The librational spectrum is then found to be

$$\begin{aligned} S_\phi(\omega) &= |\chi(\omega)|^2 S_T(\omega) \\ &= \frac{2\gamma kT}{I((\omega_\phi^2-\omega^2)^2+\gamma^2\omega^2)} \end{aligned} \tag{2.28}$$

This formula describes very well the observed librational motion from our experience.

Note that integrating this expression over ω, we obtain

$$\frac{1}{2}I\omega_\phi^2\langle\phi^2\rangle = \frac{1}{2}kT$$

where

$$\langle\phi^2\rangle = \int S_\phi(\omega)d\omega,$$

in agreement with the equipartition theorem.

Estimation of the temperature

In principle, the area below the lorentzian curves observed in the PSD gives us direct access to the temperature through the relation

$$T = \int S_\phi(\omega)d\omega\frac{I\omega_\phi^2}{k}.$$

Obtaining an absolute value for the temperature would however require a precise estimate of both the moment of intertia I of the particle as well as the sensitivity of the angular position measurement, both of which are prone to strong systematic errors.

The standard method to circumvent this issue is to vary the pressure [107] while observing the power spectral density (PSD): over the pressure range where its area is constant the librational mode temperature is known to be 300 K as it is thermalized with the gas temperature. In our case, pressure variations slightly change the orientation and position of the trapped particle (see section 2.2.5). Incidentally, the sensitivity to angular motion is not constant and we cannot employ this method.

An alternative method is to work at a fixed pressure and identify the heat sources that would prevent thermalization. If no noticeable changes of the PSD shape and amplitude occur when they are increased, we can assume the particle's motion to be at 300 K. This is the method we used for the experiment of chapter 4 with microdiamonds in the mbar pressure range.

2.5 Limitations

The main advantage of a levitated mechanical oscillator is its isolation: one only needs to pump the gas out and go to high vacuum to remove the main cause of damping. The limitation of the system is then either how high a vacuum one can get, or how strong are other noise or heat sources. In our case, although we can observe a levitated diamond under vacuum pressure down to 10^{-3} mbars, the properties of the mechanical oscillator are not retained below $\sim$1 mbar.

We identified two limitations to our system that cause fluctuating forces or torques or induce rotation of the particles. These effects are either due to laser-induced radiation pressure or driven by the Paul trap itself. We will here only attempt to introduce the issues surrounding these limitations or how they can be mitigated. Further investigation are needed and will be conducted to give a better understanding and overcome them.

2.5.1 Effect of the radiation pressure

Beside conservative forces that shift or create a stable angular potential, there are also nonconservative forces at play in the experiment. We first focus on optical forces, in particular on the radiation pressure. Radiation pressure is caused by the scattering or absorption of light and the conservation of momentum: the difference of momentum between a scattered and incident photon is necessarily passed onto the reflecting material. In an optical tweezer, combining a high numerical aperture and an isotropic particle results in the observation of a mainly conservative optical force (the optical spring force). A small nonconservative force is nonetheless always applied to the particle through radiation pressure and can accumulate work due to the inhomogeneity of the light field [127, 128]. In a simplified picture, this effect can be explained by the particle undergoing heating cycles: figure 2.13.a) depicts such cycles where the particle position cycle while it gains kinetic energy. This effect is however strongly mitigated when the particle motion is cooled down because "the heating rate due to the [optical] nonconservative force is proportional to the energy of the [levitating particle]" [129].

Force and torque

Contrary to usual nano or micro-spheres in optical tweezers, the anisotropy of micro-diamonds makes the angular degree of freedom relevant when considering the radiation pressure. This comes from the irregular shapes -bigger than the optical wavelength- of most micro-diamonds. Here, we will show with simple examples how additional heating mechanisms rises from this anisotropy. An exhaustive theoretical description is beyond the scope of this work, we just give a hint of the processes at play before showing the experimental consequences. We also only treat reflected light: due to the high refractive index of diamond (2.5) transmitted light is also deflected and generates another radiation-induced force that we don't consider here.

Figure 2.13.b) shows the effect of radiation pressure for very simple shapes. In (i) radiation pressure on a prism-shaped particle applies a force similar to wind on a sail, both along and perpendicular to the direction of the incident light field. In (ii) we see how a particle composed of two prisms with opposite slopes next to each other sees a torque induced

by radiation pressure along the optical axis in a similar fashion to the blades of a propeller.

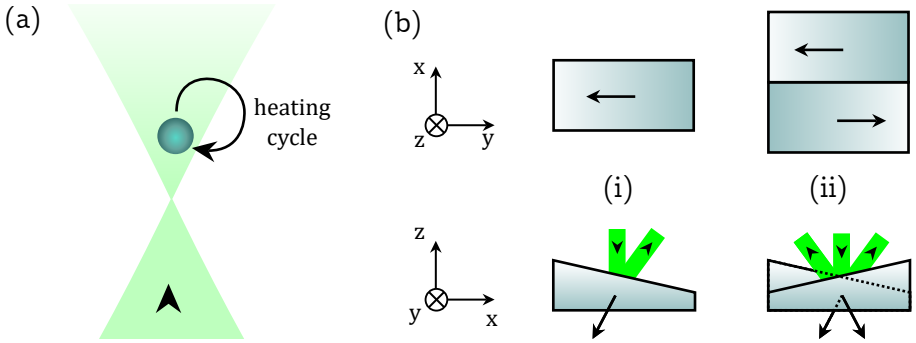

Figure 2.13: a) Example of a heating mechanism for the center of mass of an isotropic particle. Here it follows a heating cycle in and out of the light beam, during which it gains energy from the radiation pressure. b) Effect of the radiation pressure on basic shapes: (i) prism-like particle, (ii) prisms of opposite slopes next to each other. Particles are shown from two points of view: the z optical axis (top) and the y axis. Black arrows indicate optical forces while light green beams show how the laser field is reflected off the particle.

Rotation of the particle

These forces allow new heating cycles involving the angular degree of freedom, even with a homogeneous light field: for example full rotation around the optical axis for the particle in (ii) from 2.13.b) -like a windmill. This has in fact been confirmed early on by experimental observations in the case where radiation pressure strongly displaces the levitating particle [74]. In particular, we observed radiation-induced continuous rotations about the optical axis (windmill-like heating cycle).

The rotation around the optical axis and the heating of the center of mass can be observed visually using the method described in 2.2.1 for a slow motion (<10 Hz). The cause of such motion is confirmed by observing an initially stable micro-diamond and increasing the laser intensity: both center of mass and angular degrees of freedom are displaced with increasing intensity. Finally if we compare the calculated order of magnitude of the radiation pressure to the measurement of the stiffness of the Paul trap we indeed find displacement that agrees with visual observations [74]. It should be noted that as the radiation pressure and the Paul trap stiffness don't vary identically with the size of the levitating particle, we find different displacements for different sizes: about 350 nm for a 10 µm diamond and 11 µm for 2.8 µm diamond under 1 mW of total laser power.

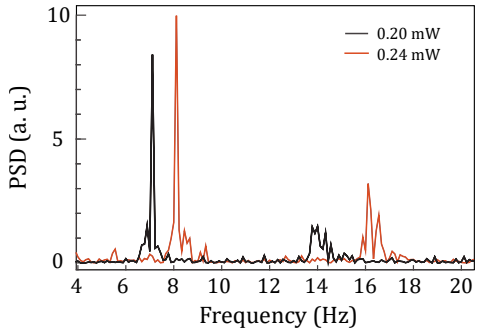

Figure 2.14: Power spectral density (PSD) of the back-scattered light from a levitated micro-diamond roating due to the radiation pressure.

By tuning the parameters of the experiment (size of the particle, intensity of the laser, frequency of the trap) we can observe both angularly confined particles (as shown in previous section under vacuum conditions) or particles rotating due to radiation pressure. Figure 2.14 shows the power spectral density from the back-scattered light obtained from a rotating micro-diamond at two different laser powers. Here the rotation is rather slow and can be seen with the naked eye using phase contrast imaging, the PSD features the first and second harmonics corresponding to rotations at a rate of about 8 Hz (*ie* angular velocity of $8 \times 2\pi$ rad/s). This rate clearly increases with the laser power and radiation pressure.

2.5.2 Trap-driven rotations

In a more confined trap designed to mitigate the effect of radiation pressure, only a strong torque is able to induce a full rotation of a levitating particle. It should however be noted that once the energy of the particle has exceeded the potential barrier of the angular confinement, the particle will continuously rotates if damping forces are not strong enough.

In practice, we observed that stable particles under atmospheric pressure often start to rotate when the pressure is lowered, and then show hysteresis *ie* rotation stops at a much higher pressure than the one at which it started. Here we first show that such rotations can actually be driven by the Paul trap. We then discuss the mechanism kick-starting these rotations.

Crankshaft mechanism

Figure 2.15 shows the Power Spectral Density (PSD) of the signal used to measure the angular position under a vacuum of 0.5 mbar for three different trap frequencies Ω. Here the particle is continuously rotating, this can be observed through NV spin magnetometry (see section 3.3) or simply by looking at the phase contrast image or the back-scattered light which both show fast time averaging of the shape of the particle and of its speckle patterns. Interestingly the particle rotates at a frequency of $\Omega/2$: in figure 2.15 one can observe the peak corresponding to the rotation, which indeed varies as we slightly ramp up the trap frequency Ω. The rotation of the particle is in fact locked by the electric potential driving the Paul trap. Note that such locked rotations have already been observed with

elongated particles levitating in an optical trap where the polarization of the optical field was periodically switched [130].

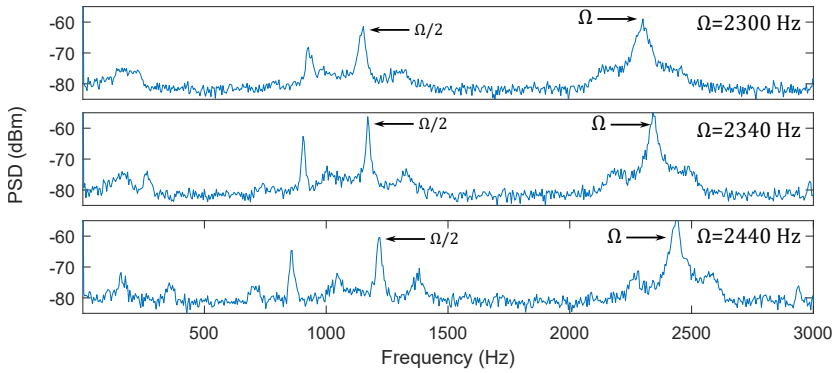

Figure 2.15: Power Spectral Density (PSD) of the angular position of a levitated diamond under a vacuum pressure of 0.5 mbar as the rotation of the particle is driven by the Paul trap.

It is possible to explain the synchronization of the particle's rotation with the Paul trap by a locking mechanism similar to a crankshaft. In order to do so, we consider a simplified problem with a single angular degree of freedom ϕ. Using the results presented in section 2.1.2 we can rewrite the torque applied by the electric field on the particle as:

$$M = M_0 \sin(2\phi)\cos(\Omega t) \quad \text{with} \quad M_0 = \frac{QV_{\text{ac}}\eta_z}{4z_0^2} S_X\,(3+\delta)\,, \tag{2.29}$$

where we consider only an AC field.

One can then notice that when the particle rotates at a frequency $\Omega/2$ with a constant velocity and at the right phase so that $\phi = \Omega t/2 + \pi/2$ the electric torque becomes:

$$M = M_0 \cos(\Omega t)^2, \tag{2.30}$$

and therefore always have the same sign, here supporting the rotation.

This can be understood intuitively by looking at the modification of the electric potential energy as a function of time, as the particle rotates. Figure 2.16 shows a particle, with a rotation period of $T = 4\pi/\Omega$ at different timescales with below, the corresponding electric potential energy. As the particle arrives at the bottom of a potential well, the time dependency of the electric field inverts the bottom of the well with the top of a potential barrier.

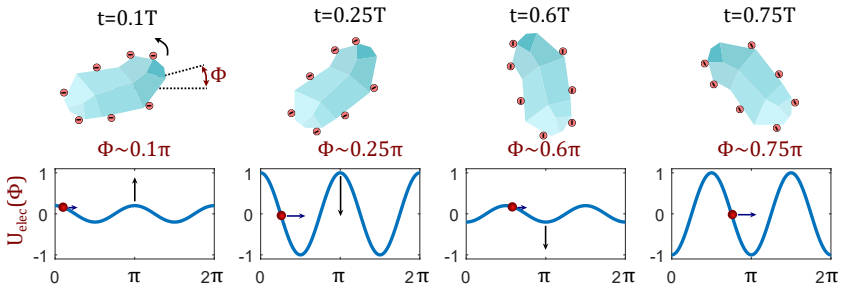

Figure 2.16: Rotation of a particle in a Paul trap. Top: illustration of the rotating diamond, at different timescales after an initial time t=0. Bottom: electric potential energy U_{elec} of the particle as a function of the orientation of the particle (ϕ).

This mechanism can maintain the rotation of a particle, compensating the drag force similarly to a mechanical crankshaft. The actual velocity is of course not constant and further investigation are being carried out in the team in order to better understand and perhaps exploit this effect and will be the focus of future work [116].

Causes of the instability

Assuming one explains that the rotation of the particle under vacuum conditions is maintained by the Paul trap through the crankshaft mechanism, one still has to explain how the transition to vacuum conditions kick-starts the rotation. Two processes could be involved here: the appearance of a new torque (or the increase of an existing one) or a change of the temperature of the librational modes such that the potential barrier between two adjacent wells can be overcome.

Identifying the exact process requires further work to be carried out. One could for example track the temperature of the librational modes or the angular position (*eg* using NV magnetometry, see section 3.3) as the pressure is lowered. Drifts of the particle position as the pressure is lowered however make such experiments difficult and we were not able to perform them for now.

2.6 Conclusion

In this chapter, we have shown that a Paul trap can confines the center of mass and the angular degrees of freedom of a levitating micro-particle. We first showed theoretically that the mechanism allowing confinement of the center of mass is also at work for the angular degrees of freedom. We have described the experimental apparatus, which is similar to an ion trap, but with a different design due to the large size and lower charge to mass ratio of the levitated particle. We then considered the levitated diamond as a mechanical oscillator: we measured the harmonic oscillations of the center of mass and of the angular degrees of freedom (librational modes) by optical means. Finally we discussed the main limitations that we observed, namely the torque induced by the radiation pressure and rotations locked by the electric field of the Paul trap below 1 mbar of vacuum pressure. Overall, we leverage the first issue by working with smaller electrodes ($\sim$ 200 µm diameter rings), which produce a higher confinement. We also observed larger particles ($\sim$10 µm) are more stable than smaller one ($\sim$ 1 µm) and therefore focus on this size range.

Finally, we have not been able to suppress the locked rotations, which limits the use of the librational mode to about 1 mbar of vacuum pressure. Although this limits the quality factor of the librational modes, we are still able to reach the underdamped regime at this pressure range.

Chapter 3

Spin control in levitating diamonds

We now turn to the second component of our system: the Nitrogen Vacancy (NV) center and its spin. We have seen in the previous section that the angular degrees of freedom of a levitating diamond can be confined owing to the anisotropy of the diamond particle. Because of the crystalline anisotropy, the NV spins are sensitive to this angular degree of freedom. Here we will describe the optical and spin properties of NV centers, before expanding on how we manipulate them experimentally. We will see how they can be used to monitor angular stability in the Paul trap and whether or not their spin properties are affected by the trap.

3.1 The NV center in diamond

Let us first describe the NV center and how its spin is experimentally manipulated, outside of a Paul trap.

3.1.1 Atomic and electronic structure of the NV center

Diamond is a solid made of carbons arranged in a crystal, it is widely studied for the properties granted by its crystalline structure and the strong covalent bond between carbon atoms. Under ambient conditions diamond is metastable, it is formed naturally at High Pressure and High Temperature (HPHT) within the earth crust. It can also be artificially synthesized either by placing carbon under HPHT conditions or by using Chemical Vapour Deposition (CVD). Diamond is a semiconductor with a high band gap of 5.49 eV [131]. This makes diamond a highly favorable host crystal for optically active atomic defects: in a semiconductor, such defects can only be optically active if both its ground and excited states lie within the material band gap. These atomic defects in diamond are called color centers because through absorption, emission or scattering of light, they give different colors to a diamond. More than 500 different color centers were found and studied in diamond [131], we are here interested in the nitrogen vacancy center only.

The crystal structure of diamond is called “diamond cubic”, each carbon atoms has four neighboring atoms. Figure 3.1.a) shows the composition of a Nitrogen Vacancy (NV) center: it consists of a nitrogen atom replacing a carbon in the diamond lattice next to a

site left vacant. It has a C_{3v} symmetry around the NV axis which can be used to calculate its molecular orbitals and accounts for some of its properties [132, 133].

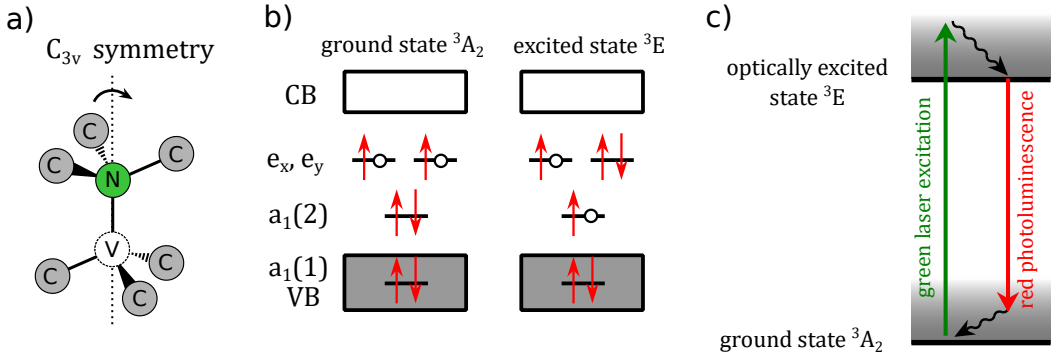

Figure 3.1: a) NV center embedded in a diamond crystal, with a C_{3v} symmetry around the NV axis. N: nitrogen, C: carbon, V: vacancy. b) Detailed electronic structure of the NV^- center, the molecular orbitals are named after their symmetry. VB: Valance Band, CB: Conduction Band. c) Orbital ground and excited states of the NV^- center. Excitation is typically done at 532 nm in the phonon band (grey gradient) while the photoluminescence spectrum is mostly in the red, following phonon emission (wavy arrow).

The NV center has two well-studied charge states: the neutral NV^0 and the negatively charged NV^-. There are several conversion processes from one to the other including optical ionization [134, 135]. We are here interested solely by the NV^- center and although the conversion to and presence of the NV^0 can be an issue (*eg* regarding spin state initialization or read-out fidelity [136]), it is not addressed here.

Since we are mostly interested in the NV^- center, unless specifically discussing the NV center charge states, we will systematically omit the $^-$ and the reader should now consider implied that we are referring by NV center to the negative charge state.

The NV center has six electrons which share four molecular orbitals. Two electronic configurations with two unpaired electrons give rise to a ground and an excited states separated by an energy corresponding to a wavelength of 637 nm as presented in figure 3.1.b).

3.1.2 Orbital states and optical observation

The orbitals of the NV center result in specific optical features. We will first describe them and then elaborate on the optical set-up used to characterize them. The optical set-up used here is similar to the one in the levitating diamond experiment.

NV optical transition

Figure 3.1.c) shows the ground and excited states from the NV center and its optical transition. Despite having its emission in the red, NV centers are often excited using a 532 nm green laser. Because of coupling to the phonons of the diamond lattice, both the NV center excitation and emission optical spectrum is broadened by Stokes and anti-Stokes shifts. The NV center can hence be efficiently excited by a green laser and emits light

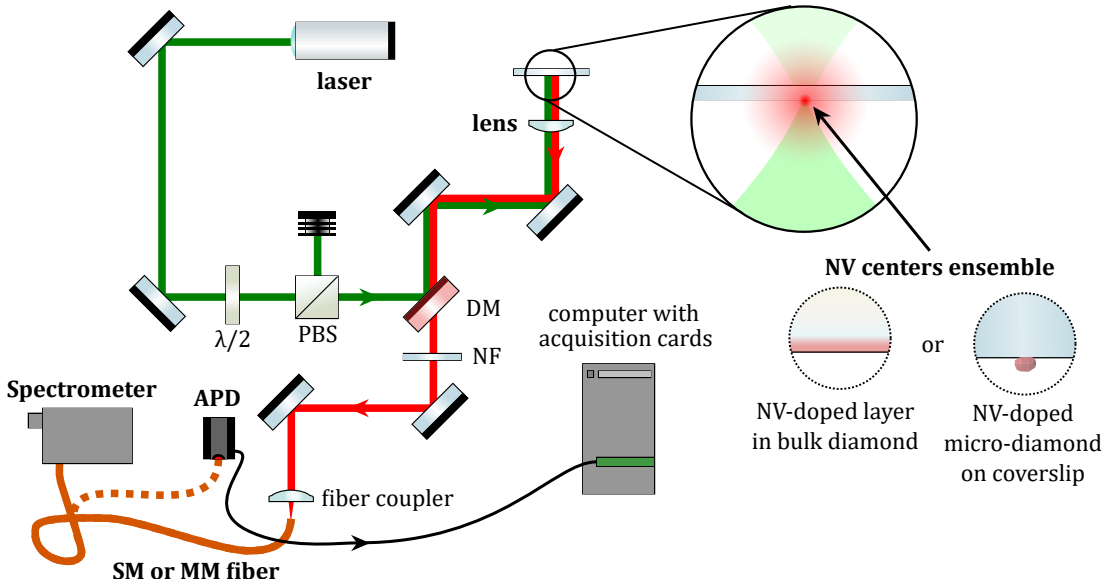

Figure 3.2: Confocal set-up for optical observation of NV centers. Optical excitation is carried out by a 532 nm green laser, the power of which can be tuned using a waveplate ($\lambda/2$) followed by a Polarization Beam Splitter (PBS). The laser is focused onto an NV-rich diamond and the red PL is collected by the same lens (high numerical aperture aspheric lens). The excitation and PL beams are separated by a Dichroic Mirror (DM) and after being further filtered by a Notch Filter (NF) the PL is coupled into a Multi-Mode (MM) or Single-Mode (SM) fiber. The PL is analysed using a spectrometer or measured by an APD. In the latter case the photons are counted by a PCIe acquisition card.

between 637 nm and ∼750 nm. Coupling to the phonon gives rise to specific features in the emission spectrum: a sharp peak, the Zero Phonon Line (ZPL) at the difference of energy between the ground and excited states and the Phonon Side Band (PSB), a broader peak at lower energy. They correspond to emission of light without and with creation of phonon(s) respectively. Do note that the phonons considered here are the one of the diamond crystal *ie* vibration between carbon atoms and not phonons corresponding to the collective motion of the whole crystal as one harmonic mechanical oscillator.

NV spectrum using a confocal microscope

The optical spectrum of NV centers is acquired using the home-build confocal microscope described in figure 3.2. The 532 nm laser source is a ∼4.5 mW laser module from Thorlabs (CPS532) and its intensity can be tuned using a halve-wave plate followed by a polarization beam splitter which can be combined with neutral density filters if needed. A high Numerical Aperture (NA) aspheric lens (NA=0.77 LightPath 355330 or NA=0.5 C240TMD from Thorlabs) is used to both focus the excitation laser and collect the PhotoLuminescence (PL) unto and from a diamond sample containing NV centers. The collected red PL is separated from the excitation laser by a dichroic mirror and a notch filter around 532 nm. It is then coupled into a Single-Mode (SM) or Multi-Mode (MM) fiber. When the system is well-aligned, the SM or MM fiber is conjugated with the focus point of the collection lens (hence the confocal term) and the fiber provides spatial filtering: light coming from

any other point of the sample or from the room is not efficiently injected in the fiber. This allows one to reduce the background light from the room or from the sample. In practice a SM fiber provides a more efficient spatial filtering than with a MM fiber since it rejects all optical modes but one. Light transmitted by the fiber is finally sent either to a spectrometer or to an Avalanche Photo-Diode (APD). The spectrometer consists of a CCD camera (iDus 401A from Andor) mounted on a grating spectrograph (Shamrock 500i gratings 1200 or 1800 l/mm from Andor).

The emission spectrum of an ensemble of NV centers is shown in figure 3.3. It shows the characteristic features of the NV^- center as well as of the NV^0 center, which is also optically active. The proportion of the two charge states incidentally depends on the optical power used, evidencing the optically activated charge conversion process [134, 135]. The NV^- centers typically emit about 5% of the total photoluminescence (PL) intensity in the Zero Phonon Line (ZPL) at 637 nm and 95% of the PL into the phonon sideband ranging from around 640 to 800 nm.

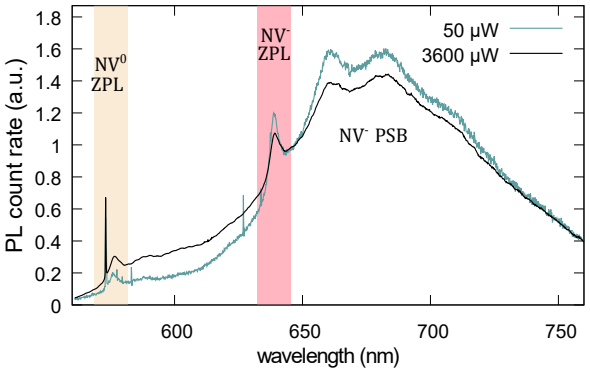

Figure 3.3: Photoluminescence spectrum of an ensemble of NV centers in a 10 µm diamond, laying on a quartz coverslip under green laser excitation, for two different laser powers. Both features of the NV^- and NV^0 can be distinguished: the Zero Phonon Line (ZPL) and the Phonon SideBand (PSB). The sharp peak on the left of the NV^0 ZPL is Raman scattering of the green laser by the diamond.

The NV center presents some key advantages as an optical emitter: in particular, it is photo-stable at room temperatures and its ZPL is nearly lifetime-limited at cryogenic temperature. Most of its PL (>70%) is however emitted in the PSB following phonon emission which is a considerable drawback for applications requiring optical coherence. Light emission can however still be used as a detection tool in biology for example to observe the motion of marked cells [137, 138].

Note that in the entirety of this manuscript we show results on NV ensembles. While the properties of single NV centers (especially spin properties) can be superior to the one of NV ensembles due to inhomogeneities, working with large ensembles grants a higher PL and signal to noise ratio. Since it considerably lowers the acquisition time, it allows for faster development and understanding of the system.

The spectrum shown in figure 3.3 is obtained from a 10 µm micro-diamond (sample:

MSY 8-12). We estimate the number of NV centers in a micro-diamond with the photoluminescence count rate measured by a single photon detector. We observed strong inhomogeneities in our sample from one diamond to another, with count rates varying from 0.5 to 200 MHz, under 3.6 mW of excitation laser and with a high numerical aperture (NA=0.77) aspheric lens. Given our collection efficiency, we find there are roughly from 10^3 to 10^6 NV centers in each of these micro-diamonds.

Here we are interested in using NV center spins to control a mechanical oscillator. As we will see, thanks to spin-dependent processes between the NV orbital states, the NV optical transition provides a practical means to control the NV spins.

3.1.3 Optically detected magnetic resonance

One of the most important features of the NV center is its optically addressable and long lived electron spin. We will make extensive use of these properties in this thesis. Here, in order to introduce how NV spins are manipulated at room temperatures, we describe the processes allowing Optically Detected Magnetic Resonance (ODMR) of NV spins, which combines optical initialization and read-out with Electron Spin Resonance (ESR).

Optical spin initialization and read-out

Figure 3.4.a) illustrates the energies of the orbital ground and excited states as well as the fine structure of their spin states. Due to the presence of two unpaired electrons in its electronic structure, the NV center is a spin one system with three possible spin states $m_s = 0, \pm 1$ where m_s is the projection of the spin on the N-V axis. In the orbital ground state, spin-spin interation between the two unpaired electrons lifts the degeneracy between the $m_s = \pm 1$ and $m_s = 0$ states and induces a zero-field splitting of D = 2.87 GHz [133]. In the orbital excited state, a similar coupling is present with a lower interaction $\mathrm{D_{exc}} = 1.43$ GHz and combined with two orbital states. At room temperature those orbital states are however mixed through a dynamical Jahn-Teller effect [139, 140] such that the orbital excited state can be described in a simplified picture similarly to the ground state.

Optical transitions are electric dipole transitions and therefore conserve the spin projection: $\Delta m_s = 0$. The orbital excited state has a relatively short lifetime of $\tau_{exc} \simeq 10$ ns and two decay paths: through optical emission (spin-conserving) and through a non-radiative decay to an intermediate singlet meta-stable state ($\tau_{met} \simeq 200$ ns [141]) . The later process is spin-dependent and is at the heart of the optical control of the NV spin at room temperature: decay into the meta-stable state is about ten times more likely for the $m_s = \pm 1$ states than for the $m_s = 0$ state [142, 143]. From the meta-stable state there are (almost) equal decay rates into all three spin states of the orbital ground state through other intermediates states not described here [141, 144].

The consequences from this spin-selective process are two-fold: first, under optical excitation and afeter a few optical cycles the NV spin population is polarized in the $m_s = 0$ spin state; second, after optical excitation the ground $m_s = 0$ spin state is on average brighter than the $m_s = \pm 1$ states, which spend longer time in the meta-stable state. This results both in the ability to optically initialize and to read-out the NV center spin states.

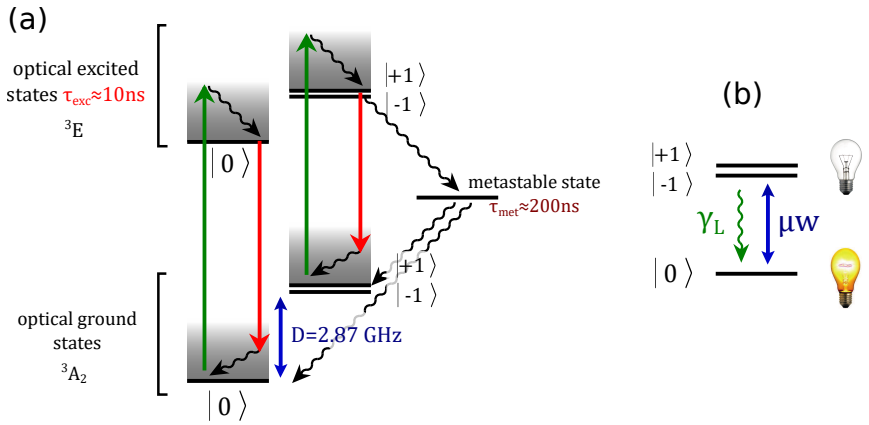

Figure 3.4: a) Simplified struture of the electronic states of the NV^- center, including the three spin states $m_s = 0, \pm 1$. Red (green) arrows are optical (off) resonant transitions while the blue arrow is a microwave transition. Wavy arrows represent non-radiative decay. b) Simplified scheme of the spin system: under green laser excitation, the $m_s = \pm 1$ spin states are darker than the $m_s = 0$ and decay towards the ground states at a rate γ_L. A microwave (μw) can then drive the transition between them.

The optical polarization efficiency is about 80 % [142, 143] , it is limited by the non-zero relaxation rate from the spin ground state into the metastable state which does not allow for fully spin-conserving optical cycle of the spin ground state. Considering a single optical cycle, the $m_s = \pm 1$ dark states emit about half as many photons than the $m_s = 0$ bright state, the spin read-out efficiency then depends on the amount of PL detected.

Electron Spin Resonance

Besides optical transition, there are microwave dipole magnetic transitions between the $m_s = 0$ and $m_s = \pm 1$ states within the orbital ground or excited states. A transverse magnetic field oscillating resonantly with the transition will indeed allow one to flip the spin state.

Figure 3.5.b) shows Electron Spin Resonance (ESR) spectra obtained by combining optical and microwave excitation to carry out an Optically Detected Magnetic Resonance (ODMR) measurement. It is produced by detecting the Photoluminescence (PL) from the NV centers while applying a strong microwave field and sweeping its frequency across the spin resonance at $\nu = 2.87$ GHz. If the microwave is detuned from the resonance, optical cycles polarize the NV centers in the brighter $m_s = 0$ spin state whereas at resonance a strong continuous microwave drive balances each spin states population therefore reducing the detected PL. Under a strong continuous microwave drive the contrast of the ESR can be expected to be as high as 30 %. The contrast of the ESR in fact depends on many factors: the relative strength of the optical and microwave fields, the spin lifetime, and the selectivity of the spin-dependent non-radiative decay, which can vary (see next section). Figure 3.5.b) shows two ESR at different microwave powers. The ESR plotted in trace (ii) was done under a weaker microwave excitation: it has a lower contrast but displays a sharper peak, which evidence a power broadening as the ESR becomes saturated.

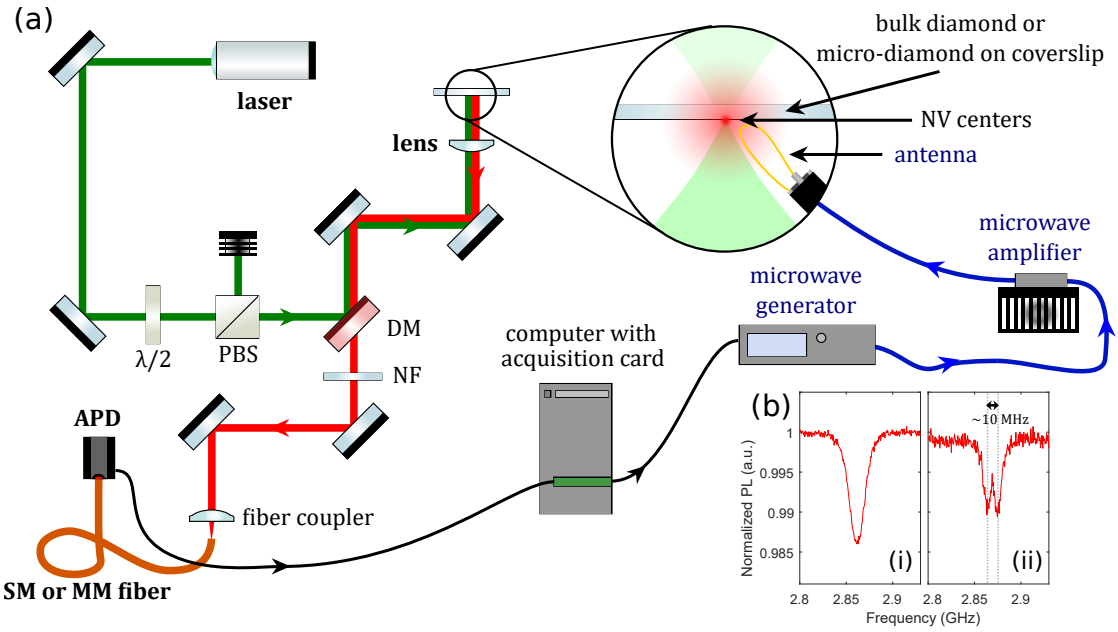

Figure 3.5: a) Set-up for measurement of the NV Electron Spin Resonance (ESR). We use a confocal microscope (previously described) to excite and collect the PL emitted by NV centers. The PL is measured by an APD and the photon count rate is counted by the acquisition card of a computer. We send a microwave current in an antenna -a wire loop- that we approach close to the sample. For the microwave current we use a generator and an amplifier. APD: Avalanche PhotoDiode, SM/MM fiber: Single/Multi Mode fiber, DM: Dichroic Mirror, NF: Notch Filter, PBS: Polarizing Beam-Splitter. b) Typical ESR spectra obtained when scanning a microwave field around the magnetic resonance while shining a green laser unto NV centers and observing their photoluminescence (PL). We use (i) 10 dBm, (ii) 0 dBm of microwave power.

Figure 3.5.a) presents our ESR set-up. We collect the PL of the NV center using a home-build confocal microscope further described above. The light is then sent to an Avalanche Photo-Diode (APD) which sends the photon count to an acquisition card (PCIe 6320 from National instrument). To generate the microwave field, we send a strong microwave current through an antenna brought in the vicinity of the NV centers. The microwave current is generated by a Rhode & Schwartz generator (SMB100A, up to 25 dBm) followed by an amplification stage (amplifier ZHL-5W or 15W 422 from mini-circuit). The antenna is made of a simple wire loop soldered to an opened SMA coaxial cable. We use wires between 15 µm and 150 µm diameter and bring them at least within a few hundreds of µm away from the NV centers. The microwave generator is controlled by the same acquisition card that counts the photons. This allows us to perform sweeps of its frequency with triggered steps while the PL is measured. A single sweep typically lasts a few hundred miliseconds and we accumulate a few hundreds of them to obtain the ESR spectra showed in figure 3.5.b). We show two spectra realized with different microwave powers. Trace (ii), for which we use a lower power displays two unresolved peaks due to a small strain in the diamond crystal (see next section).

3.1.4 Impact of the magnetic field

NV spins and ESR measurement can be used for magnetometry thanks to the Zeeman effect. When one applies an external magnetic field to an NV center, it does not only modify the energies of the spin states, but it also changes the eigenstates of the Hamiltonian if the magnetic field break the crystalline symmetry around the NV axis. Here we will describe the new Eigenstates of the Hamiltonian due to the Zeeman effect and discuss the implications on the ESR spectrum.

Zeeman effect and new Eigenstates

The Hamiltonian describing the spin in the orbital ground state can be written [145]:

$$\hat{H}_{NV}/\hbar = D\left(\hat{S}_z^2 - \frac{1}{3}S\left(S+1\right)\right) + E\left(S_x^2 - S_y^2\right) + \gamma_e \hat{\mathbf{S}}.\mathbf{B}, \tag{3.1}$$

where $\hbar$ is the reduced Planck constant, D and E are zero-field splittings, $\hat{S}_x$, $\hat{S}_y$, $\hat{S}_z$ are the Pauli matrices for a spin $S = 1$ and $\mathbf{S}$ the corresponding Pauli vector, γ_e is the gyromagnetic ratio of the electron and $\mathbf{B}$ is the external magnetic field.

The $D = 2.87GHz$ coupling is due to a spin-spin interaction [133] while E mainly comes from mechanical strain of the diamond crystal and ranges from 100 kHz in high purity bulk crystals to 5 MHz in nano-structures. Without a magnetic field the strain can slightly lift the degeneracy between the spin excited states, splitting the $|\pm1\rangle$ states of generally around 10 MHz. In most of our samples, this strain leads to the observation of two lines in the ESR spectrum even under no magnetic field. These two peaks -although unresolved- can be observed in the trace (ii) of figure 3.5.b). This is comparable to the Zeeman splitting introduced by a 5 G magnetic field, in order to simplify the diagonalization of the Hamiltonian, we therefore neglect the impact of strain from now on.

The last term is the Zeeman energy, which lifts the degeneracy between the $m_s = \pm1$ states when a magnetic field is applied. Because the spin-spin interaction is strongly anisotropic, the orientation of the magnetic field compared to the NV crystalline axis is critical. Plots from figure 3.6 demonstrate the impact of this anisotropy on the energies of the spin eigenstates, as well as on their projection on the zero-field eigenstates $|0\rangle$ and $|\pm1\rangle$. Let us rewrite the Hamiltonian while neglecting the strain and considering a field in the XZ plane:

$$\hat{H}_{NV}/\hbar = D\hat{S}_z^2 + \gamma_e \hat{S}_z B_{\parallel} + \gamma_e \hat{S}_x B_{\perp}, \tag{3.2}$$

where $\mathbf{B} = B_{\perp}\mathbf{e}_x + B_{\parallel}\mathbf{e}_z$. If there is no transverse field, the Hamiltonian is already diagonal and gives a linear Zeeman effect, plotted in figure 3.6-a). On the contrary if there is a transverse field, the new eigenstates will be superpositions of the zero-field eigenstates ($|0\rangle$, $|\pm1\rangle$).

Figure 3.6.b) shows the energies of the eigenstates under a transverse B field only: the Zeeman effect is much weaker and affect the ground and excited state while the third eigenstate becomes insensitive to the magnetic field. This specific case is treated in more details in section 4.4 but in short this is directly caused by the spin mixing of the new eigenstates.

Let us now consider the eigenstates and their energies when the magnetic field intensity is fixed but its orientation compared to the NV axis is continuously rotated. The

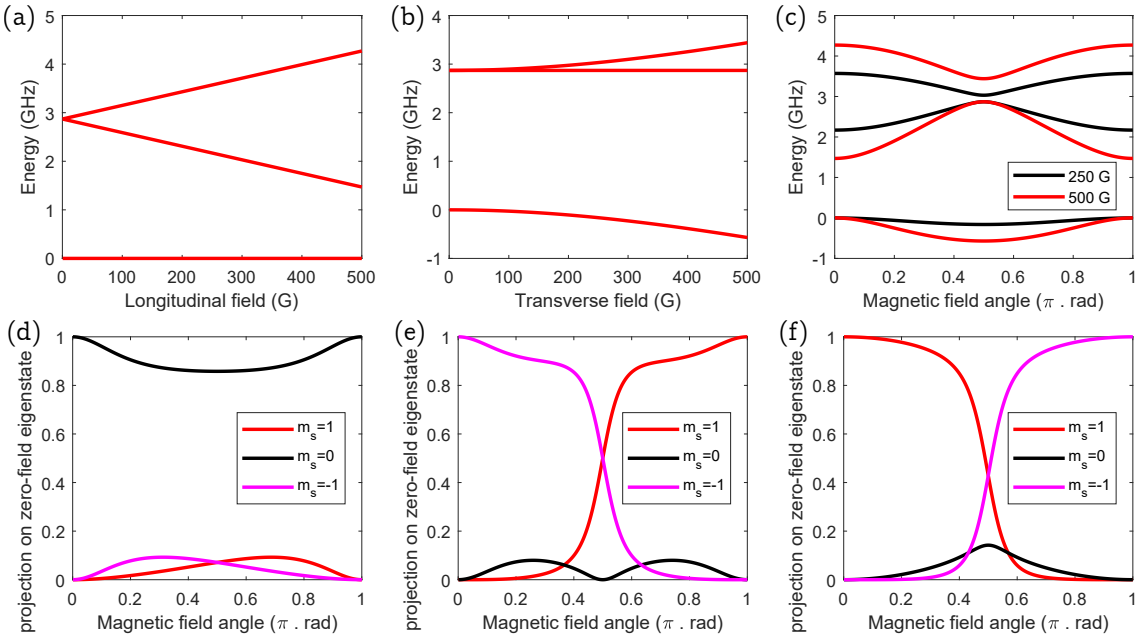

Figure 3.6: a), b), c) Eigenenergies of the spin orbital ground states of an NV center under a longitudinal, transverse and rotating magnetic field respectivaly. d), e), f) Square of the projection of the three zero-field egenstates unto the ground, intermediate and excited spin states respectively as a function of the orientation of a 500 G magnetic field.

eigenenergies, plotted in figure 3.6.c) follow a pi-periodic curve with an avoided crossing when the field is transverse. Note that this variation of the energy with the orientation is at the core of the proposal to obtain a spin-mechanical coupling using the angular degrees of freedom: it translates into a magnetic torque applied to the diamond crystal through the NV spin.

In order to evidence the mixing of the zero-field eigenstates ($|0\rangle$, $|\pm1\rangle$) in the new eigenstates we plot for each new eigenstate the square of its projection on the zero-field eigenstates in figure 3.6.d-e). We can see that this mixing occurs for the three new eigenstates as soon as the field is not longitudinal.

This mixing has important implications for the optical cycles because it allows optical transitions between different spin levels: optical excitation are not spin-conservative anymore. It will also average the spin-selective non-radiative decay, which is at the heart of the optical spin read-out. Both effects will lower optical initialization and read-out fidelity and incidentally reduces the contrast of an ESR spectrum. Such effects are described in more details in section 4.4.

ESR of spin ensembles under a magnetic field

The tetrahedral structure of the diamond crystal allows for four non-degenerate axes for NV centers to co-exist in a single crystal. Although it is possible to synthesize a crystal with preferentially oriented NV centers, most of our work was carried out on diamonds with NV centers equally distributed among the four possible orientations. As we work

with large ensembles, there is the same amount of NV centers along the four orientations.

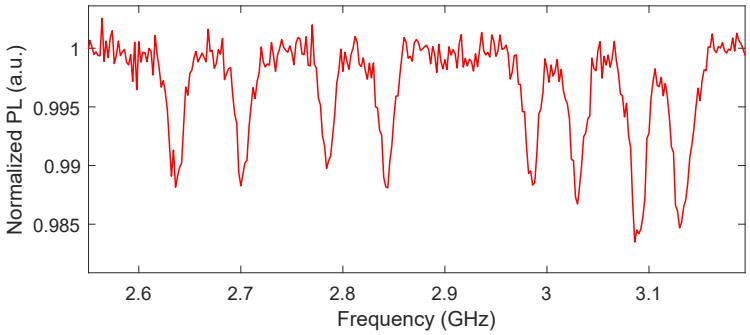

Figure 3.7: ESR spectrum for an NV center ensemble in a single microdiamond taken under a magnetic field of about 100 G. We use a microwave power of 10 dBm.

Figure 3.7 shows an ESR spectrum with a magnetic field of about 100 G. The field is generated by a neodynium magnet brought in the vicinity of the diamond. Since the energy of the spin states under a magnetic field depends on the orientation of the magnetic field compared to the NV axis, we can observe up to eight resolved ESR peaks corresponding to the two new excited eigenstates of the four different NV orientations. In practice all peaks are often not resolved and the magnetic field has to be properly set for the eight lines to be revealed.

3.1.5 Hyperfine coupling to nuclear spins

The full energy structure of an NV spin is actually enriched by the presence of nearby nuclear spins embedded in the diamond lattice. Magnetic dipole-dipole and contact interaction with ^{13}C (spin one) or Nitrogen (spin one for ^{14}N and spin one half for ^{15}N) atoms gives rise to a hyperfine structure in the electron spin resonance spectrum. Another analogous point of view -for magnetic dipole-dipole coupling- would be that an NV spin energy depends on the state of nearby nuclear spins, as its energy is shifted through the Zeeman effect from the magnetic field generated by nearby nuclear spins.

This hyperfine structure can be resolved when observing a single NV spin coupled to few nuclear spins. Figure 3.8 shows an ESR spectrum from NV spins in a high purity diamond, here we observe NV ensembles and the hyperfine structure is due to the coupling of each NV spin to the nuclear spin of its nitrogen (^{14}N, with a spin 1). With single spin, one can actually use the NV electron spin to control nearby nuclear spins [146, 147] and recently, up to 10 nuclear spins were simultaneously manipulated by a single NV spin [20]. Because they are strongly localised and have a weaker gyromagnetic ratio compared to electron spins, nuclear spins are well insulated from their environment and constitute two level systems with excellent lifetime and coherence time.

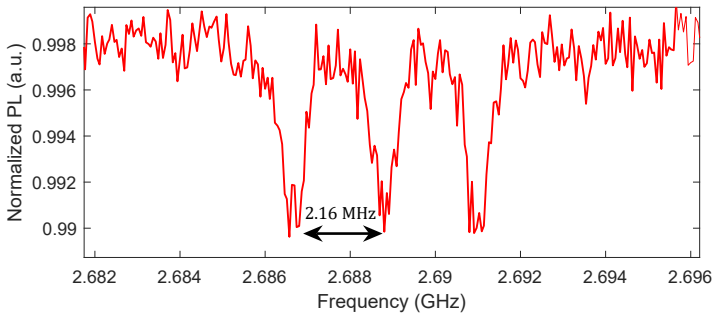

Figure 3.8: Electron spin resonance from NV spins in an isitopically purified CVD-grown bulk diamond. We use a microwave power of -20 dBm.

If there are too many nuclear spins or if one observes an inhomogeneous spin ensemble, coupling to the nuclear spins will broaden the ESR line. This will result in an apparent drop of the coherence of the NV spin that is comparable to spectral diffusion: the energy of the NV spin -coupled to nuclear spins- will vary with time (as the nuclear spins will flip), and so will the dephasing between two NV spin states. Note that given the long lifetime of nuclear spins, one might use decoupling -or rephasing- scheme to recover the NV spin coherence. This issue is discussed in more details in the next section.

Coupling of an NV electron spin to nuclear spins can be described in the Hamiltonian using the hyperfine tensors $\mathbf{A}_{ij}^{(n)}$:

$$\hat{H}_{NV}/h = D\hat{S}_z^2 + \gamma_e \hat{\mathbf{S}}.\vec{B} + \sum_n \mathbf{S}.\mathbf{A}^{(n)}.\mathbf{I}^{(n)}, \tag{3.3}$$

where n are indexes for nearby nuclear spins and $\mathbf{I}^{(n)}$ is their Pauli vector. The form of the hyperfine tensor depends on the geometry of the system and on the distance between the two spins.

For the interaction between the nitrogen of the NV center and the electron spin, we have:

$$A^N = \begin{pmatrix} A_\perp^N & 0 & 0 \\ 0 & A_\perp^N & 0 \\ 0 & 0 & A_{zz}^N \end{pmatrix} \tag{3.4}$$

with $A_{zz}^N = 2.16$ MHz [148] while $A_\perp^N \sim A_{zz}^N \ll D$ [149] -off-diagonal terms in the Hamiltonian- can often be neglected in the secular approximation. As each NV center has the same coupling to its Nitrogen nuclear spin and with an overwhelming majority of ^{14}N isotope (99.6% natural abundance), it can be observed with ensembles as soon as the inhomogeneous width of the ESR line is small enough. This is indeed the frequency span between two peaks in the spectrum of figure 3.8.

3.1.6 NV spins lifetime and coherence

Measurement of the ESR observed through Optically Detected Magnetic Resonance showed above are continuous measurements: the photoluminescence is detected under a continuous microwave and optical pumping for different microwave frequencies.

However, because the NV spin lifetime (longitudinal relaxation time) and coherence lifetime (transverse relaxation time) are long compared to the time it takes to perform optical initialization/read-out and microwave drive respectively, one can also perform pulsed experiments to coherently address the spin or for example measure its relaxation. Such control of the NV spin is mandatory if one is to implement proposals where the NV spin is used for coherent control of a mechanical oscillator.

The main features of the set-up that we use are depicted in figure 3.9, they will be further detailed below for each measurements carried out. In these measurements, we use micro-diamonds obtained by milling HPHT diamonds (MSY 8-12 µm from microdiamond) which are deposited on a quartz coverslip. Note that as already mentioned, we found the NV density to be inhomogeneous from one diamond to an other ($\sim 10^3$ to 10^6 NV per micro-diamond).

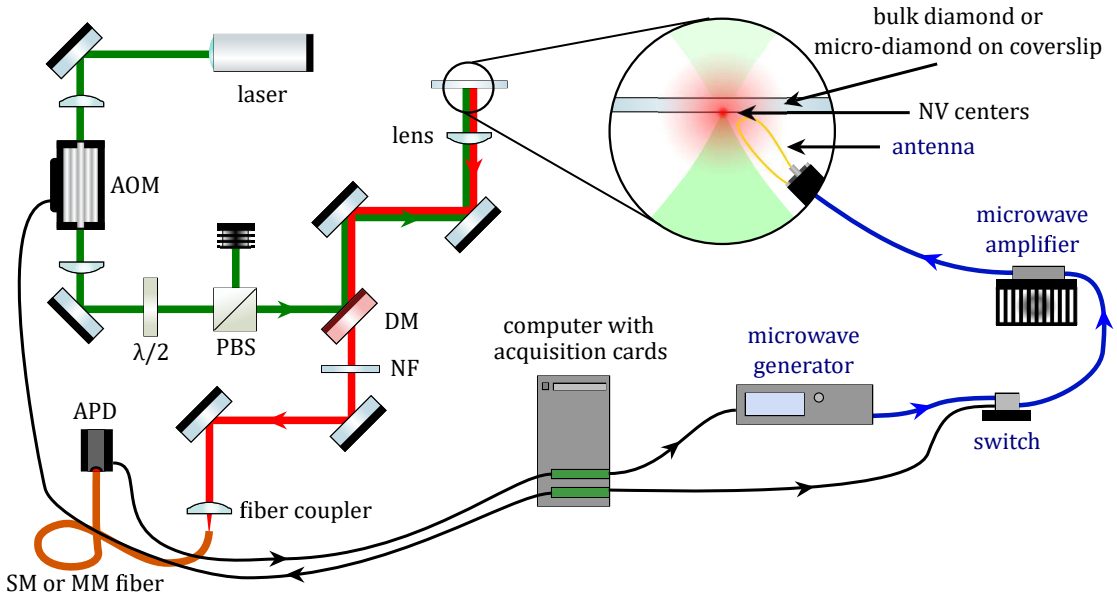

Figure 3.9: Set-up for pulsed measurement of NV spins. Optical excitation is carried out by a 532 nm green laser, which can be rapidly (<50 ns) switched off using an acousto-optic modulator (AOM). The laser is focused and the red PL collected by the same lens while the two beams are separted by a Dichroic Mirror (DM) and a Notch Filter (NF). The PL is coupled into a multi-mode (MM) or single-mode (SM) fiber and sent into an avalanche photodiode (APD), the photons count rate is counted by the acquisition card of a computer. We send a microwave current in an antenna -a wire loop- that we approach close to the sample. For the microwave current we use a generator and an amplifier. Acquisition cards are used to both set the frequency of the generator and rapidly shut down the microwave current using a switch situated between the generator and the amplifier.

Longitudinal relaxation time

Let us first consider the spin lifetime (longitudinal relaxation time), that is the so-called T_1 time of the electron spin. There are two relaxation mechanisms which songly impact the spin T_1: interaction with lattice phonons and cross-relaxation with nearby spin impurities [150]. At room temperature and in a pure enough sample, the former process dominates

the relaxation dynamics while the latter limits the lifetime at cryogenic temperatures [150], as the average phonon number is lowered. Similarly, if the number of bulk impurity is high enough or if the NV spins are shallow and therefore close to surface impurities, cross-relaxation also limits the NV spins lifetime at room temperature [150, 151].

To estimate the T_1 time in our samples we use the pulse sequence depicted in Fig. 3.10.a). Typically, a 15 microseconds, 1 mW green laser pulse first polarises the NV electron spins by using the intersystem crossing in the excited state described in section 3.1.3. Then, an identical second laser pulse is used to excite the NV center and the PL (Photo-Luminescence) the NV centers emit is collected, and sent to an avalanche photodiode (APD SPCM-ARQ-15 from Perkin-Elmer). A PCI card (PCIe 6320 National instrument) then measures the count rate during the first ∼10 microseconds of the laser pulse (using an internal gate). The amplitude of the measured PL depends linearly on the probability of being in the ground $|m_s = 0\rangle$ state.

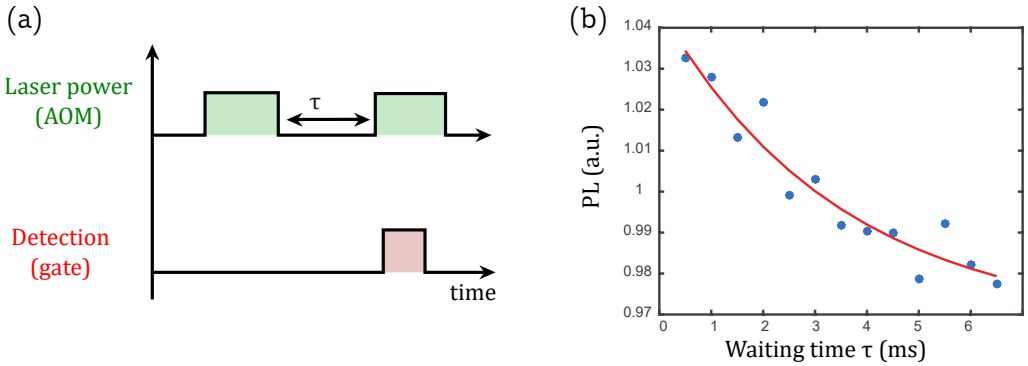

Figure 3.10: a) Pulse sequence used for measuring the T_1 time of NV centers. b) Photoluminescence as a function of the dark time between the two laser pulses. An exponential fit gives $T_1 = 3.2 \pm 0.2$ms.

By repeating this sequence while varying the delay between the two laser pulses, we thus measure how fast the NV spins relax back to the thermal equilibrium. Figure 3.10.b) shows a typical result for micro-diamonds laying on a coverslip. We obtain a decay time $T_1 = 3.2 \pm 0.2$ms from an exponential fit to the data. Typically the lifetime measurement is repeated and accumulated about 10000 times per point, depending on the intensity of the PL. The T_1 values that we measure actually range from 1 ms to 10 ms and are limited by coupling to the phonon bath of the diamond crystal or to nearby impurities [150].

Note that in order to perform an efficient measurement, the duration of the laser pulse and of the measurement window must be properly tuned to be longer and shorter respectively than the time it takes to optically polarize the spins. Since the polarization time depends on the optical power used, it should be measured every time the experimental conditions are changed. It can be obtained simply by looking at the contrast of the lifetime measurement while varying the parameters (duration of the laser pulse and of the measurement window). Alternatively, we can perform the measurement sequence presented in figure 3.11.a): the spins are initialized in the spin excited state (*eg* $|1\rangle$) by a microwave pulse (see experimental details below) and the PL is read-out after a varying re-polarization time. Figure 3.11.b) shows the results from this sequence: with 1 mW of

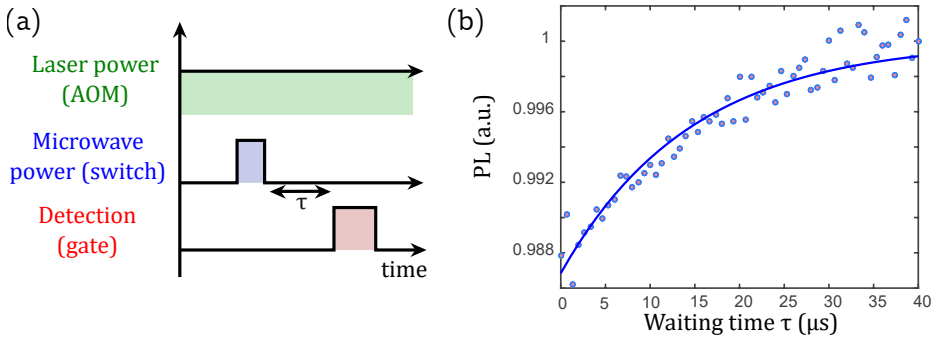

Figure 3.11: a) Shows the pulse sequence used for measuring polarization time of NV centers. b) Photoluminescence as a function of the re-polarization time, after a microwave pulse.

laser power it takes a few tens of microseconds for the spin polarization to saturates.

As we will see next, both the T_1 and the time it takes to polarize the spin are long enough not to impact measurement of the coherence time.

Bloch sphere

In order to describe the evolution of a superposition of two states, we use the representation of the spin wave-function on the Bloch sphere. Let us consider the wavefunction of a superposition of the two spin states $|m_s = 0\rangle$ and $|m_s = 1\rangle$:

$$|\Psi\rangle = \alpha|0\rangle + \beta|1\rangle. \tag{3.5}$$

If we consider the wavefunction normalized and choose the overall phase so that α is real, we can rewrite any superposition state:

$$|\Psi\rangle = \cos\frac{\theta}{2}|0\rangle + \sin\frac{\theta}{2}e^{i\phi}|1\rangle, \tag{3.6}$$

where $0 \leq \theta \leq \pi$ and $0 \leq \phi \leq 2\pi$. Those two angles can then be used to define a vector on a unity-radius sphere in polar coordinate as depicted in figure 3.12.a). We call such sphere the Bloch sphere and the vector corresponding to a given state the Bloch vector. When the Bloch vector is at the north or south pole of the sphere, the spin is in the $|0\rangle$ and $|1\rangle$ state respectively. The Bloch sphere gives a simplified view of the evolution of a superposition state.

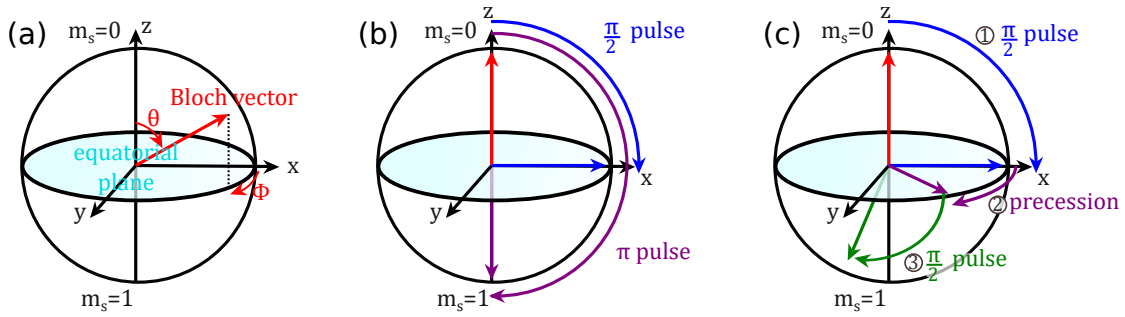

Figure 3.12: a) Bloch sphere and Bloch vector. b) π and $\pi/2$ pulses depicted on the Bloch sphere. c) Evolution of the Bloch vector during a Ramsey fringes experiment.

Rabi oscillations

Under a microwave magnetic field perpendicular to the spin quantization axis and oscillating in resonance with a transition between the ground and an excited spin states, the spin undergoes Rabi oscillations. If it starts for example from the $|0\rangle$ states, it continuously evolves between superposition states to the $|1\rangle$ state and back and forth. In a frame rotating at the frequency of the field, this consists in a simple rotation of the Bloch vector around the x or y axis -depending on the phase of the microwave field. The frequency of such rotation is called the Rabi frequency and depends on the strength of the perpendicular oscillating field B_1:

$$\Omega_{\mathrm{R}} = \gamma_e B_1. \tag{3.7}$$

Depending on the duration τ of the microwave signal, one can perform rotation of an arbitrary angle $\Omega_{\mathrm{R}}\tau$. π and $\pi/2$ pulses, which rotate the Bloch vector by π and $\pi/2$ respectively are depicted in figure 3.12.b).

Rabi oscillation can be observed on NV spins using a sequence where the microwave is pulsed. A common sequence is detailed in figure 3.13.a):

- a laser pulse initializes the NV spins in the $|0\rangle$ state
- a resonant microwave pulse is applied for a duration τ
- a laser pulse is applied for spin read-out (and spin re-polarization)
- a gated APD measures the spin state at the beginning of the laser pulse.

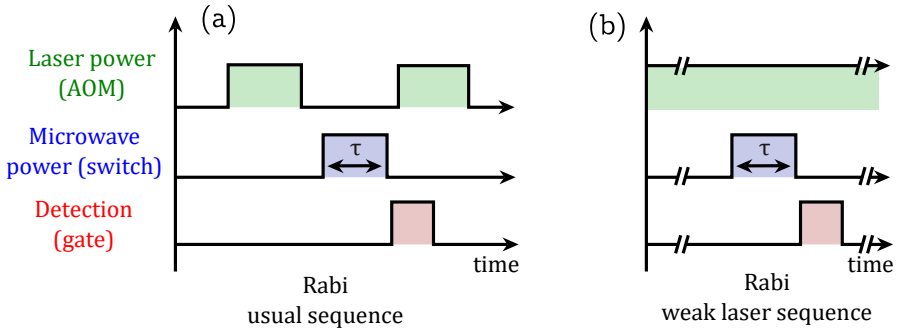

Figure 3.13: a) Shows the usual pulse sequence performed to observe Rabi oscillations of NV spins. b) Shows the sequence that we apply given a weak laser excitation. The axis break symbolises a long waiting time necessary to initialize the spins (from a dozen to a hundred microseconds).

In our specific case, the laser power is weak enough so that each NV center is efficiently initialized only after about a dozen to a hundred microseconds. This is evidenced from measurements like the one displayed in figure 3.11. On the other hand the Rabi oscillatons that we observe occur on timescales closer to one microsecond, which means that even using a continuous laser, spins are only weakly re-initialized during or right after the Rabi oscillations. Accordingly we apply the sequence described in figure 3.13.b) with continuous laser excitation, long initialization time at the beginning and at the end of the sequence and a short time between the microwave pulse and the spin read-out.

Microwave pulses are obtained using a microwave switch (ZASWA-2-50-DR+ from Minicircuit) located between the microwave generator and the microwave amplifier. A card (PulseBlaster from SpinCore Technologies, Inc.) then generates TTL pulses which control the switch. It should be noted that in the current set-up, because we only switch the input signal of the microwave amplifier, the latter slightly deforms the end of the microwave pulse. This comes from a ring-down of the amplifier [75] and could be improved by adding a high power switch after the amplifier. During the sequence, the APD continuously counts photons but the cards measuring its signal (PCIe 6320) is gated by the PulseBlaster card. Both cards are interfaced on a computer and the sequence is repeated for different microwave durations and accumulated at least several hundreds times for each point.

Observing clear Rabi oscillations on NV ensembles requires addressing the NV centers with the same orientation, otherwise the Rabi frequencies for the different orientations would likely not be the same and the Rabi oscillations would be blurred out (see SI from [75]). This can be done by applying a magnetic field as done in section 3.1.4 and tuning the microwave frequency at a single, well-resolved peak.

Figure 3.14.a) and b) show the NV photoluminescence as a function of the microwave pulse duration for two different microwave powers. One can see clear, damped Rabi oscillations. We use different microwave powers, hence the different Rabi frequencies: in a) we use 20 dBm, while in b) we use -5 dBm. Our fitting method and its result are the following: for all fits of the Rabi oscillations, we use the function

$$f(t) = 1 - C_1(1 - (C_3 e^{-t^2/\tau_1^2} + C_5 e^{-t^2/\tau_2^2}) \cos \Omega_R t). \tag{3.8}$$

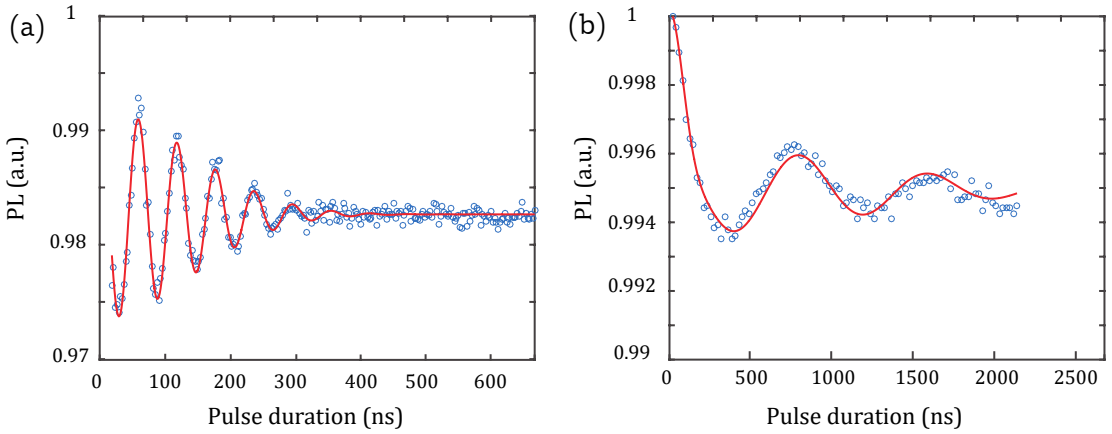

Figure 3.14: Rabi oscillations from NV centers in a diamond laying on a quartz coverslip for two different microwave powers in the presence of an externally applied magnetic field. All parameters are the same apart from the two microwave powers: a) 20 dBm, $\Omega_R = 16$ MHz, b) -5 dBm, $\Omega_R = 1.3$ MHz.

For the first Rabi measurement a), the fit gives the following values: $C_1 = 0.017, C_3 = -5.500 \times 10^{-4}, \tau_1 = 179, C_5 = 0.52, \tau_2 = 192$, in nanoseconds units. It yields Rabi oscillations periods of 60 ns$\pm$4 ns. Here, the decay can be modeled by a single gaussian decay to a good approximation.

For the second measuremt b), we get the following values for the fit $C_1 = 0.0048, C_3 = 0.7778, \tau_1 = 176, C_5 = 0.2548, \tau_2 = 1565$. Two decay constants are thus non negligible here. The short term evolution decays with a time constant of 176 ns while the long term one is given by 1.565 μs.

We make two observations from these results: first the damping of the Rabi oscillations depends strongly on the employed microwave power and secondly the damping cannot be characterized by a single exponential decay. This can actually be explained by the fact that damping of the Rabi oscillations is here governed by the inhomogeneity of the NV spins [152, 153]. Each spin is differently coupled to the spin bath composed of nearby paramagnetic impurities, and its energy varies with time depending on the spin bath state. In a simplified picture, one can notice that with a Rabi frequency that is strong compared to the ESR linewidth, all NV spins -including the one the most strongly coupled to the spin bath- will undergo Rabi oscillations and contribute to the signal that we observe. Conversely, a weak Rabi frequency will yield a lower contrast for the Rabi oscillations, but only the NV spins at the center of the ESR line will contribute to it, enabling a weaker decay [152]. Regarding the shape of the decay, it was theoretically showed that differences of coupling strengths to the spin bath from one NV spin to another yields different decay shapes [153, 154].

In practice, we were not able to fit our data to the theoretical model from [154]. Once we are able to perform π pulses faster than the decoherence of the NV spins, more complex protocols can be envisioned that allow a more precise characterization of the decoherence rate.

Dephasing: Ramsey fringes

Ramsey fringes provide a measurement of the transverse relaxation time (T_2^*) of an NV spin ensemble. It corresponds to the decay rate of the coherence between two spin states *ie* the rate at which a coherent superposition of these two states changes into a statistical superposition.
Figure 3.15.a) describes the Ramsey sequence we use while the evolution of the Bloch vector is depicted in figure 3.12.c). The NV spin ensemble is first initialized, then a microwave $\pi/2$ pulse put it in a superposition state. The microwave is usually slightly detuned from the resonance of a quantity we note Δ. In the frame rotating at the microwave frequency, the Bloch vector is therefore in the equatorial plane and rotates around the z axis at a rate Δ. After a free precession time τ a second $\pi/2$ pulse is applied and the spin state is read-out *via* the NV centers' PL.
Depending on the position of the Bloch vector at the end of the free precession time, the spin ends up in the $|0\rangle$ state ($\tau.\Delta = (2n+1)\pi$ where n is an integer), the $|1\rangle$ state ($\tau.\Delta = 2n\pi$) or in-between. This translates to oscillations of the PL signal with the free precession time τ at a frequency Δ, the so-called Ramsey fringes. Those fringes are blurred if the coherence is lost during the sequence, their decay is therefore a direct measurement of the decoherence rate of a superposition state. Although we observe Ramsey fringes in the time domain, one can proceed similarly but with a fixed free precession time τ while scanning the detuning Δ, enabling precise measurement of the transition frequency. The profile of the fringes decay is the Fourier transform of the ESR spectrum, here a Gaussian because of the inhomogeneous broadening.

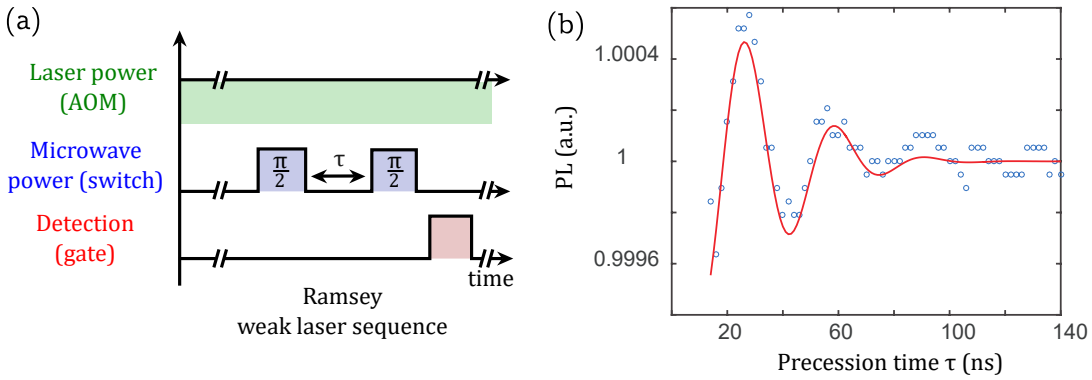

Figure 3.15: a) Ramsey sequence measuring the T_2^* of the NV spins under a weak laser. The axis break symbolises a long waiting time necessary to initialize the spins. b) Photoluminescence as a function of the free precession time for an NV spin ensemble embedded in micro-diamonds laying on a coverslip. The microwave frequency is detuned of 25 MHz from resonance.

Ramsey fringes are more precise for measuring the T_2^* when using short intense $\pi/2$ pulses that yield a higher contrast for the oscillations. Figure 3.15.b) shows Ramsey fringes obtained using the sequence described in figure 3.15.a) with diamonds laying on a coverslip and with a microwave detuning of 25 MHz from the center of the ESR transition. The microwave pulse duration is 50 ns. We fit the Ramsey signal with a Gaussian decay and obtain a T_2^* of 45 ns. It should be noted that this value is very close to the values expected from the gaussian ESR width whereas even the shortest measured Rabi decay would yield

a smaller linewidth.

In the sample we study, the width of the ESR line mainly comes from coupling to a spin bath comprising nearby electron and nuclear spins. As mentioned in the previous section, when an NV spin is coupled to a spin bath it witnesses an inhomogeneous-like broadening. This in fact causes the fast decay of the Ramsey fringes that we observe. Although Ramsey fringes give information relative to the coupling of each NV spin to the spin bath, it does not take into account the dynamics of the spin bath. Decoupling techniques such as spin echo take advantage of the slower dynamics of the spin bath and can enhance the coherence time of the NV spins.

Spin echo and decoupling from the spin bath

Figure 3.16.c) depicts the sequence that we apply to perform a spin echo on an NV spin ensemble. Aside from the initialization and measurement stages it essentially consists of two $\pi/2$ pulses separated by a precession time 2τ split in two by a π pulse at half the total precession time. The role of the π pulse is to re-phase the inhomogeneous precessions. An inhomogeneous dephasing can occur between different NV spins but also for each single NV spin at a different time when the measurement is averaged (and as the state of the spin bath changes). Both these dephasings are rephased by the echo sequence. Figure 3.16.a) shows a geometric analysis in the Bloch sphere that demonstrates it simply. Let us consider that the spin bath is frozen during one measurement sequence. After the first $\pi/2$ pulse the spin precesses, which translates, in the rotating frame, in a rotation in the equatorial plane at a speed equal to the detuning between the spin transition and the microwave frequency. Inhomogeneities will cause the Bloch vector to rotate at different speeds, for different spins. Figure 3.16.b) shows the evolution of this dephasing for three different detunings. The inhomogeneous dephasing causes a fast decay of the Ramsey fringes in the Ramsey sequence. We can see that applying a π pulse at the center of the precession time allows inhomogeneous dephasings to be rephased during the second part of the precession time. This happens as long as the spin bath has not changed during one iteration of the echo sequence.

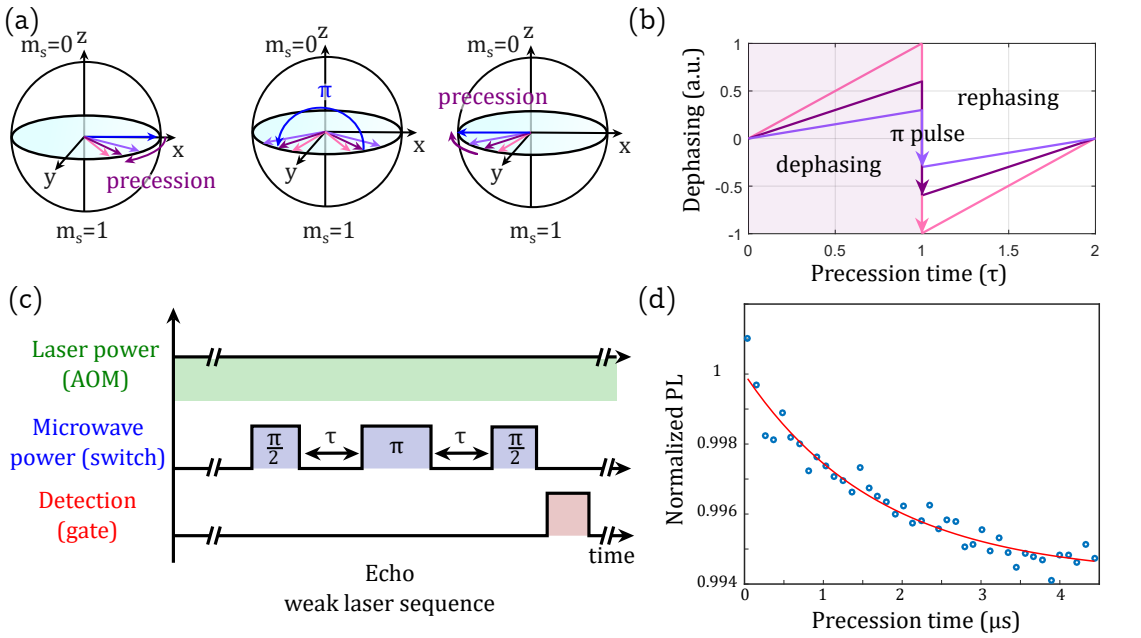

Figure 3.16: a) Bloch vector during an echo sequence, in between the two $\pi/2$ pulses. b) Evolution of the dephasing for three NV spins (or one NV spin for different spin bath states) during the precession time. Dephasing is measured compared to the x axis before the π pulse and compared to the -x axis after. Here we consider the π pulse to be infinitely short. c) Echo sequence used to measure the T_2^{echo} of the NV spins under a weak laser. The axis break symbolises a long waiting time necessary to initialize the spins. d) PL as a function of the free precession time for NV spins ensemble in deposited micro-diamonds.

The PL as a function of the free precession time τ for an echo sequence is shown in figure 3.16.c). Here an exponential fit yields a decay time of 1.65 µs. We typically measure echo decays between 1 and 3 µs for this sample (MSY 8-12).

Damping of the echo signal is here due to the fluctuation of the spin bath: as it changes during an echo sequence, it introduces errors in the rephasing process. Working with purer samples comprising less electron spins and eventually less nuclear spins would increase the T_2^{echo}. Otherwise, one can employ more complex decoupling sequences with more than one rephasing π pulse like the Carr-Purcell-Meiboom-Gill (CPMG) sequence [155, 156], spin locking [157] or the XY4 sequence [158].

3.1.7 Spin properties in diamond particles

Even if spin properties can be improved using decoupling schemes they will primarily depend on the diamond material. Here we give a small overview of the NV spins properties and what governs them.

Low temperature

Going from room temperature (RT) to Cryogenic Temperature (CT) usually enhances coherence and lifetime because coupling to the phonon bath is reduced. This is especially the case for the optical line of the NV center but the NV spin lifetime is similarly increased to nearly a second below 80 K [156]. The spin coherence however remains limited

by the coupling to the spin bath, even at CT (here 4-8 K): overall, dynamical decoupling sequences are still required to recover a coherence time limited by the spin lifetime [156].

Well-resolved optical lines nonetheless change the paradigm of NV spin read-out. In fact optical transitions have different wavelengths for different spin states. Because they are resolved at low temperatures, it becomes possible to resonantly excite spin-selective optical transitions. By repeating several optical cycles while measuring the PL in the Phonon Side-Band (PSB) one can achieve high fidelity spin read-out. This additionally provides high fidelity initialization through a slight spin mixing. In bulk material and with a single NV center working at CT below 10 K, the fidelity for spin initialization is 0.998 [19] while the fidelity for spin read-out is as high as 0.96 [159].

Such attractive properties should be tempered by the implied experimental constraints: the cited results were obtain within a liquid helium cryostat, using a bulk diamond with a solid immersion lens etched around a single NV spin to improve the PL collection efficiency. Currently such conditions are hardly compatible with a levitating diamond experiment. Although optical cryogenic cooling is possible [109, 160] and its implementation with a levitating rare-earth particle was successful [110] it is for now limited to a final temperature of about 80 K. NV spin properties at CT are therefore limited to experiments with clamped diamond cantilever.

Role of the paramagnetic impurities

Since the NV spin coherence is limited by coupling to the surrounding spin bath, its coherence can be improved by removing as many spins as possible from its surroundings [161, 162]. One can achieve this by producing high purity diamonds through Chemical Vapour Deposition (CVD) and using ^{12}C isotopically purified carbons to limit the number of nuclear spins from the ^{13}C isotope [163]. A single NV spin in such diamond for example displayed a coherence time as high as 500 µs without any decoupling sequence [18].

Those coherence times are however obtained with NV centers deep within the diamond crystal: when the NV spin is closer to the surface, its properties will suffer from the presence of surface impurities. The magnetic noise from those impurities lowers both the lifetime [151] and coherence time [164] of shallow NV spins. This is crucial for spin-mechanical experiments with levitating diamonds since working with smaller -*eg* nano- diamonds increases the spin-mechanical coupling rate while the NV decoherence is expected to be the strongest limitation under high vacuum. Note that as discussed in section 4.4, dynamical decoupling can be integrated within a spin-mechanical experiment to solve this issue. With a single decoupling pulse (Hahn echo sequence) one can reach coherence times up to 200 µs for 5-nm-deep NV spin and of 800 µs for 50-nm-deep NV spin [165]. The impurities themselves could also be driven to decouple them from NV spins [166] .

3.1.8 Samples for the levitation experiment

As we have seen, the diamond quality is crucial for the spin properties of NV centers. There are however experimental constraints to be considered in the levitation experiment: most importantly, our injection procedure requires a relatively large amount of diamond particles.

The method of choice to achieve a high spin coherence time in diamond micro-particles would be to use etching to fabricate micro or nano crystals from a high purity CVD diamond made using isotopically purified carbon [167]. In practice, although we were able to obtain micro-pillars from such high purity diamonds, we were unable to detach a sufficient amount to load them into the Paul trap.
The other method that allows one to obtain large quantities of diamond particles from a bulk crystal consist in milling it. Although we tried milling high purity diamonds, it seems the process introduces an inhomogeneous strain in the diamond particles that we obtained. This strain yields an inhomogeneous broadening of the ESR lines such that their linewidth is similar to the one in low purity diamonds. Further work should be carried out to either test different milling processes or fabricate a sufficient quantity of micro-diamond through etching.

The samples that we used in the levitation experiment are therefore milled HPHT diamonds. Our most commonly used diamonds are MSY samples from the company microdiamond, they are sold as powder of particles with calibrated sizes. We mostly used MSY 8-12 (between 8 and 10 µm) and used it without applying any additional treatment. These samples were extensively used in the experiments of chapters 2 and 3.

Another key point regarding the samples that we use is the concentration of nitrogen impurities in the diamond crystal. As mentioned above, a large quantity of nitrogen will negatively impact the spin properties of NV centers. However, since we are working with spin ensembles, a large number of NV centers will enhance the signals that we observe and the spin-mechanical coupling that we want to see. It is important to note that all nitrogen atoms in a diamond crystal are not converted into NV centers. In fact most of them remain as substitional nitrogen centers (N_s, without an associated vacancy) [168], which still degrade the spin properties of nearby NV centers. Interestingly, it is possible to increase the conversion rate from N_s to NV center through irradiation by high energy electrons, ions or even high laser pulses combined with annealing [169].

We therefore used a second type of sample: MDNV15u provided by the company Adamas. They are micro-diamond of 15 µm size that have a similar nitrogen concentration than MSY samples but that have been irradiated by high energy electrons or ions. The NV concentration in these samples is roughly 1000 times higher than with MSY diamonds. These samples were mostly used to observe the spin-mechanical coupling in chapter 4. We finally also used similarly irradiated nano-diamonds (brFND-100 from FND biotech) for experiments of chapter 5.

3.2 Observation and control of NV centers in levitating diamonds

Once a micro-diamond is levitating, we aim at controlling embedded NV spins similarly to what we have shown with diamonds laying on a coverslip. Here we will first describe the observation and characterization of the PL from NV centers embedded in a levitating diamond and then explain how we combine a microwave antenna with the trap set-up to achieve spin manipulation. Apart from the microwave antenna, we use a similar set-up as described in sections 3.1.2 and 3.1.3 to read-out and control the spin states. Two different

antenna systems were operated: first an external antenna similar to the one from a non levitating experiment and then a ring antenna integrated to the trap.

3.2.1 NV optical observation

Observation of the PL is achieved by modifying the tools described in sections 3.1.2 to adapt them to the Paul trap. The confocal microscope and optical path is nearly identical to the one previously described (section 3.1.2, figure 3.2) so we will only emphasize the differences from a non-levitating set-up. The NV center PL is collected by an aspheric lens (NA=0.77 LightPath 355330 or NA=0.5 C240TMD from Thorlabs). We don't focus the excitation laser on but rather in front of the levitating particle for visualization purpose. This introduces a mismatch between the divergence of the collected PL and the green laser. It is usually corrected either by natural achromatism of the aspheric lens, or by an additional lens on the path of the green laser. After repeated loading of the trap, micro-diamonds start to pollute the surface of the aspheric lens, it is therefore often protected by an additional glass coverslip fixed to the lens mount. Finally since we don't have parasitic light from a substrate, a large core Multi-Mode fiber is used to facilitate the collection of the PL.

Once the PL is collected, its photon can be counted using an APD or its spectrum analyzed by a grating spectrometer. Figure 3.17.a) shows the spectrum from NV centers embedded within a levitating micro-diamond and figure 3.17.b) the spectrum from a similar diamond laying on a quartz coverslip. We use the same sample for both experiments: 10 µm diamonds (MSY 8-12).

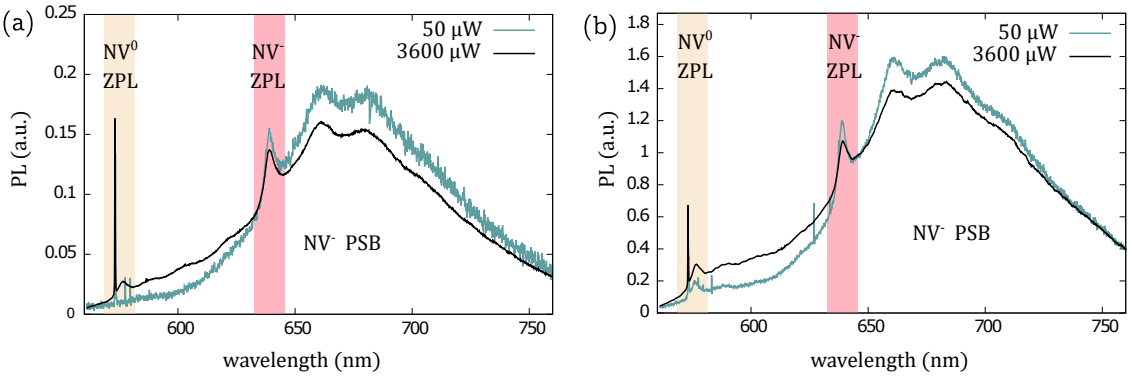

Figure 3.17: Optical spectra of NV centers embedded within a micro-diamond for two different powers for a) a levitating diamond and b) a diamond lying on a glass coverslip.

The same features of the NV^- and NV^0 centers (already described in section 3.1.2) are visible with no distinguishable pattern when levitating compared to non levitating experiments. Although this experiment was carried with micro-diamond (8-12 µm), another experiment found similar results with nano-diamonds levitating in a Paul trap [52]. We should note that as we don't use chromatic aberration-corrected optics, the spectrum can be slightly distorted depending on the alignment of the collection optics (aspheric lens and coupling into the fiber).

3.2.2 External antenna

Approaching an antenna close to the levitating micro-diamond to generate a microwave field proved to be difficult due to the trap high voltage and the necessity to approach the antenna at least within a few hundreds microns from the diamond. Figure 3.18.a) depicts the antenna in the early stage of the experiment: we approached a 28 µm gold wire stretched between two bigger wires close to an endcap trap. To avoid electric arcs, the amplitude voltage of the trap is lowered to about 600 V while other parameters (frequency, distance between the endcap electrodes) are adjusted to maintain the particle stably trapped.

We noticed that the trap stability parameters depend upon the distance between the antenna and the center of the trap. Numerical simulations show that the stiffness of the trap increases when the distance with the antenna decreases. As the antenna is brought close to the trap, the q factor of the Mathieu equations thus increases and so the frequency and AC voltage are often adjusted to keep the q factor well within the stability region. In the presence of the antenna, trapping is nonetheless still critical and the particle is often lost due to small air flows, when the trapping apparatus is not properly enclosed. This points towards a decrease of the potential depth due to the increasing asymmetry of the trap. This issue, also confirmed by numerical simulations, prevents us from acquiring data for more than about half an hour and limits the signal to noise ratio of the ESR using such antenna.

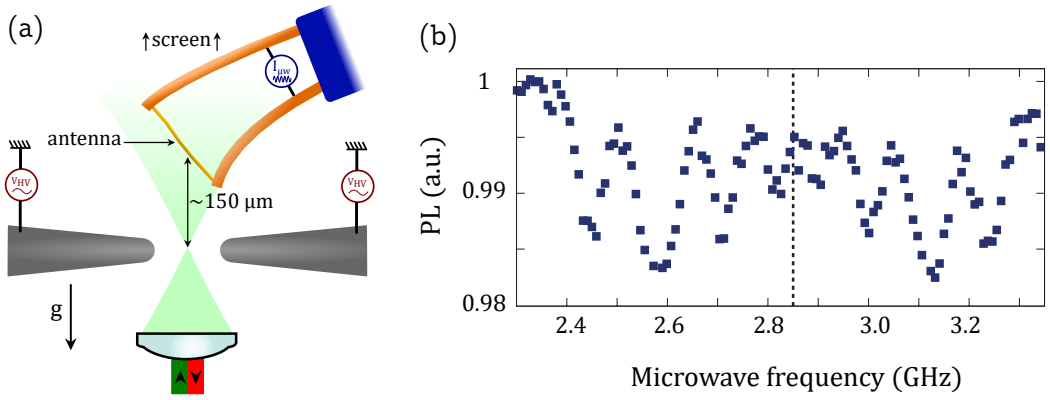

Figure 3.18: a) External antenna system with an endcap trap: a 28 µm wire is approached about 150 µm from the center of the trap. b) Electron spin resonance spectrum (ESR) from NV spins embededd in a micro-diamond levitating in an endcap trap, under a magnetic field of about 150 G.

Combining the microwave antenna with optical observation of the NV centers allows us to read-out and efficiently manipulate NV spins embedded within levitating diamonds. Figure 3.18.b) shows an ESR spectrum from a levitating micro-diamond (MSY 8-12 µm) under a magnetic field of about 150 G. This spectrum already demonstrates two important points: first the orientation of the levitating micro-diamond is stable, secondly we are not able to detect degradation of the spin properties (line width, initialization, read-out). These points will be further discussed in the next two sections 3.3 and 3.4, let us focus for now on the experimental system. Here, the inability to perform long measurements

requires us to use a strong micro-wave driving to saturate the NV spins and improve the contrast of the ESR. This in turn first enlarges each spin line through power broadening but also creates artefacts in the spectrum due to heating and dilation of the antenna.

3.2.3 Integrated ring antenna with Bias T

To overcome these limitations and simplify the system, one can use a ring geometry for the trap and use this same ring for the antenna as well. The microwave amplifier then needs to be insulated from the high voltage amplifier. This is achieved by a bias T, which acts as a filter taking advantage of the large frequency difference between the two microwave (GHz) and high voltage (kHz) signals.

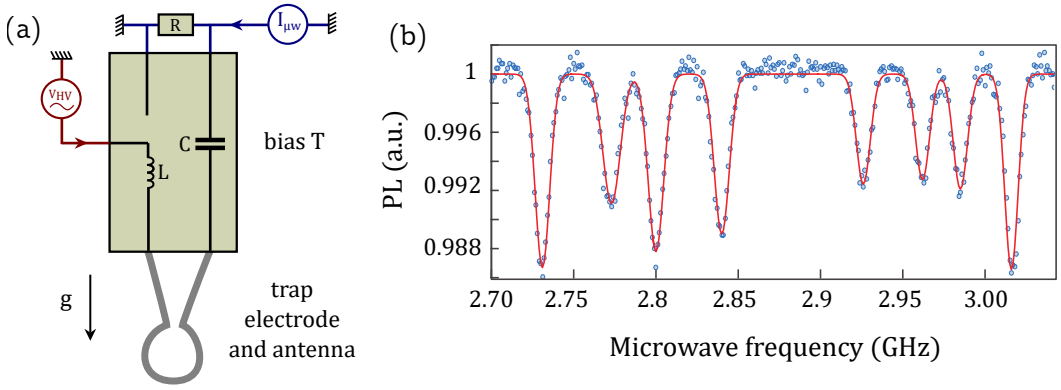

Figure 3.19: a) Ring trap mounted on a bias T. The bias T combine the microwave current and the Paul trap high voltage while the ring plays the role of both the trap electrode and the antenna. b) Electron spin resonance spectrum from NV spins embededd in a micro-diamond levitating in a ring trap under a magnetic field of about 50 G. Here the ring inner diameter is 180 µm and the diameter of the wire is 25 µm.

Figure 3.19.a) shows the trap mounted on the bias T. A small capacity (C∼pF) and a resistance (R=50 Ω) are used to filter out the high voltage while a coil filters out the microwave current. Note that in the current scheme both the microwave and the high voltage are connected to a nearly open load and are mainly coupled into the ring only thanks to the auto-capacity of the circuit. This is always the case for a Paul trap and not uncommon for a microwave antenna.

Figure 3.19.b) shows an ESR spectrum obtained from NV spins in a levitating micro-diamond (MSY 8-12 µm) with this system and a small (180 µm) ring trap. The signal to noise ratio (SNR) of the ESR is distinctly better than the one performed with an external antenna (figure 3.18.b)). A direct consequence of this is that it is not necessary to strongly drive the NV spins: we still clearly distinguish the ESR lines with a weaker microwave field causing a lower contrast but also sharper lines.

The higher SNR can be traced back to several factors. First the antenna generates a higher microwave field at the diamond position with fewer intensity and heating in the antenna. The small ring trap also confines the particle more strongly than the endcap trap when the antenna has been approached and the voltage reduced, which means any

fluctuating force on the levitating diamond induces a smaller noise. Finally the ring trap was enclosed in a vacuum chamber which provides better insulation from air flow than the box used with the endcap trap. Overall, only the first experiments (see next section) were performed with the endcap trap and external antenna: once installed the system with an integrated antenna was preferred.

3.3 NV spins to monitor the angular stability

Here, we discuss the angular stability of a levitating diamond through the prism of the NV spins embedded in it. In particular, we show how the ESR spectra can be used to monitor the angular stability. This section is closely related to section 2.4 where we consider only the motion of the mechanical oscillator.
We describe two experiments: one where the angle of the diamond is stable and one where the diamond is rotating in the trap due to radiation pressure.

3.3.1 Paul trap angular stability

The spectra showed in figure 3.18.b) and 3.19.b) clarify an important point regarding the levitating diamond: its orientation is stable over time. If it wasn't, the orientation of the magnetic field compared to each of the four possible orientations would vary and so would the spin states energies (see figure 3.21.a) or section 3.1.4 for details). In the ESR spectrum this would considerably broaden the spin lines.

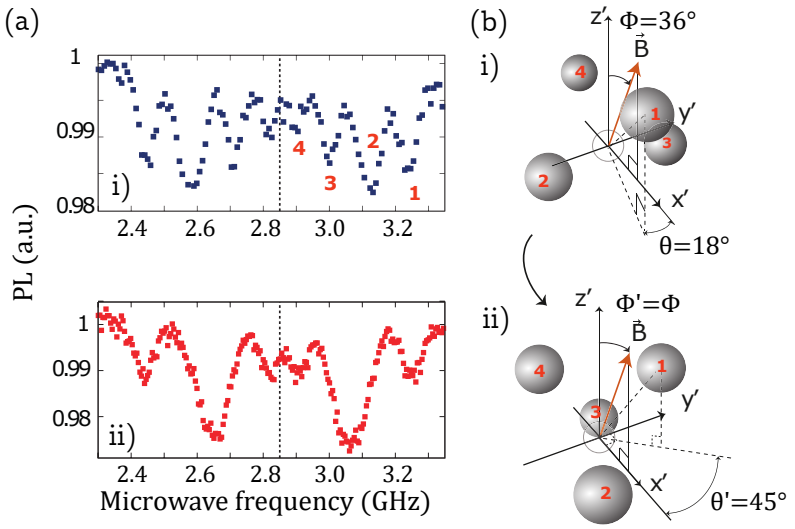

Figure 3.20: a) ESR spectra from a levitated micro-diamond. Trace i) and ii) are obtained with the same magnetic field and micro-diamond but with different frequencies for the trap voltage. b) Orientation of the NV centers with respect to the magnetic field parametrised by ϕ and θ. The angles are calculated from the corresponding ESR spectra.

Although one can consider angular stability was already demonstrated by the observation of the librational modes (see section 2.4.3, a well resolved ESR spectrum under a magnetic field provides an unambiguous proof. The ESR spectrum can also be used to

characterized the rotation of a levitated diamond.

Figure 3.20.a) displays two ESR spectra for different frequencies of the Paul trap (3.3 KHz and 2.6 kHz): the angles between the magnetic field and each possible NV orientation changes and so does the position of the ESR lines. It is in fact possible to determine the orientation of the diamond crystal with respect to the magnetic field using the eight (eventually non-resolved) ESR lines of an NV spin ensemble. We show that the orientation of the crystal compared to the magnetic field in figure 3.20.b) for the two different ESR spectra. Note that here, we used the specific features of the spectra to simplify calculations [74].

As discussed in section 2.4.1 the fact that the trap parameters have an impact on the orientation of a levitated particles indicates the Paul trap has a role in the confinement of the particle. Although the rotation of the particle can be observed *via* phase contrast imaging, the ESR spectra were key to confirm it.

3.3.2 ESR spectra in rotating diamonds

Rotation of micro-diamonds due to radiation pressure have been observed through visualization and measurement of the back-scattered light (see section 2.5.1). We now show the impact of such rotation on the ESR spectra. Here we use smaller diamonds than from the previous experiment (∼2.8 µm size). Because the radiation pressure has a stronger effect on them, they tend to enter continuous rotation more often. Figure 3.21.a) shows the energies of the two spin transitions as a function of the angle between the magnetic field and the NV axis. Contrary to ESR spectra previously shown, the ESR spectrum of a rotating diamond under a magnetic field will be blurred because the NV spins energy varies when the angle between the magnetic field and the NV axis changes.

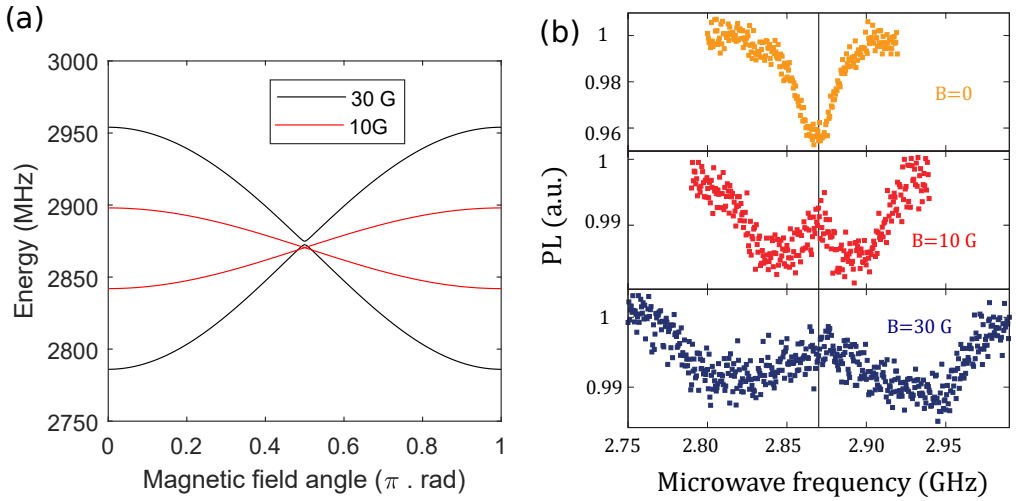

Figure 3.21: a) Frequencies of the spin transition as a function of the angle between the magnetic field and an NV center for different magnetic field intensities (see section 3.1.4 for details). b) ESR spectra from a levitating and rotating micro-diamond (2.8 µm size) for three values of the magnetic field: B=0, B= 10 G and B= 30 G. The system used is composed of an endcap trap with an external ESR antenna.

Figure 3.21.b) shows ESR spectra from a rotating micro-diamond (MSY 2.25-3.5 µm) under different magnetic field intensities. As the magnetic field is increased the ESR is broadened but do not show resolved lines. Since each spectrum is obtained by averaging the signal over minutes while each NV senses a varying magnetic field, we observe the mean distribution of the spins energies. For one NV crystalline axis it should be close to the distribution of a sinus, here we observe a superposition of four distributions corresponding to the different NV crystalline axes.

Note that if the particle rotation is confined to a single axis, a resolved spectrum can be obtained by tuning the orientation of the magnetic field close to the rotation axis. In practice attempts to do so failed, evidencing a more complex motion. This comes from the fact than during a full rotation -*eg* around the optical axis- the particle explores angles far from the trap equilibrium position which can results in electric torques along different axes than the initial rotation.

3.4 Coherent control and spin properties in levitating diamonds

Let us turn to more advanced studies of NV spin properties as presented in section 3.1.6 but with levitating diamonds. Beside the spin lifetime measurement, these experiments (Rabi oscillations, Ramsey fringes, spin echo) require coherent control of NV spins and therefore an angularly stable levitating diamond. Those experiments allow us to verify that NV spins properties are not degraded by the Paul trap mechanism but are also a prerequisite to pulsed spin-mechanical protocols [43].

We have already showed that bigger ~ 10 µm sized micro-diamonds are less impacted by radiation pressure and show stable orientation within our Paul trap. More generally, the effects of radiation pressure are mitigated while working with a stronger angular confinement: the minimum torque needed to climb up the angular potential barrier is higher and the fluctuations of the angle for a given temperature are lower. We hence used a small ring trap (170 µm wide, described in section 2.2.2) to trap ~ 10 µm micro-diamonds (MSY 8-12 from micro-diamond) and probe the lifetime and coherence properties of NV centers.
The measurement that we carry out here (spin lifetime, Rabi oscillations, Ramsey fringes and spin echoes [75]) are similar to the one presented in section 3.1.6 except for the trap set-up, described in section 3.2. We will therefore only briefly comment the results. The main difficulty of these experiments stems from having a large enough confinement and a strong enough microwave drive. Both these constraints are achieved by using the small ring electrodes.

Spin lifetime

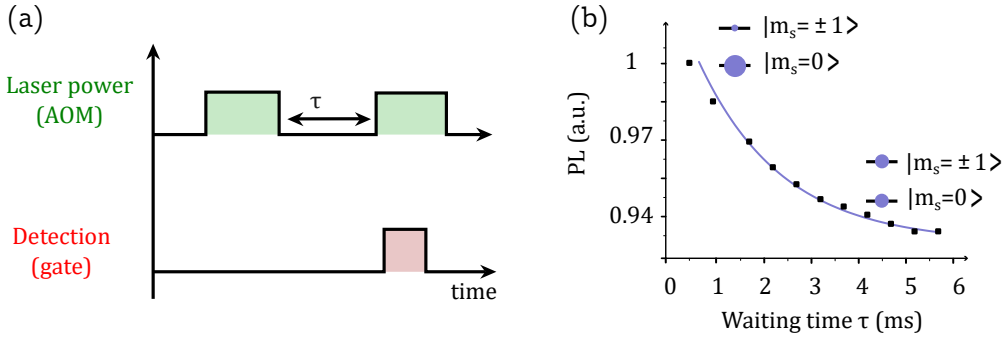

Figure 3.22: a) Pulse sequence used for measuring the T_1 time of NV centers. b) Photoluminescence as a function of the dark time between the two laser pulses. An exponential fit gives a decay time $T_1 \sim 3$ms.

Figure 3.22.a) shows the sequence that we use to measure the NV spins lifetime and figure 3.22.b) the resulting photoluminescence. The measured T_1 (3 ms here) is in the same range as the one that we measure from the same sample of micro-diamonds but laying on a coverslip (1-10 ms).

Rabi oscillations

Figure 3.23.a) depicts the sequence that we use to observe Rabi oscillations from spin ensembles. Figure 3.23.b) shows Rabi oscillations. We observe coherent oscillations for up to 2.5 µs at a Rabi frequency of around 4 MHz.

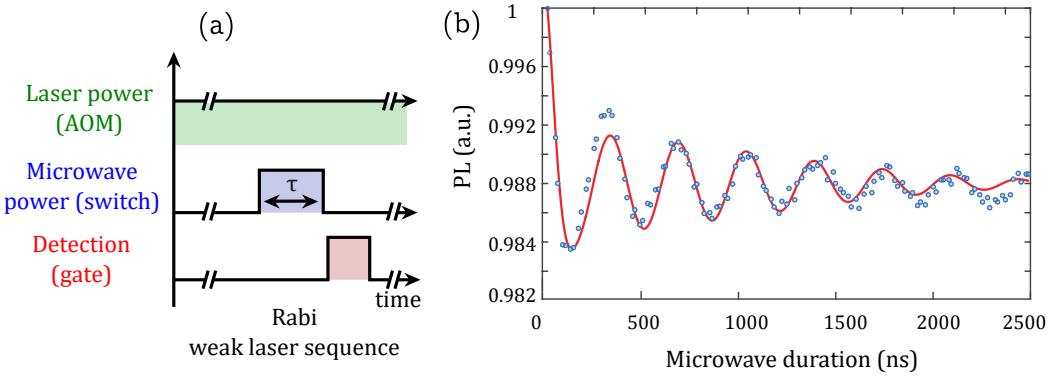

Figure 3.23: a) Sequence applied to observe Rabi oscillations given a weak laser excitation. The axis break symbolises a long waiting time necessary to initialize the spins (from a dozen to a hundred microseconds). b) Rabi oscillations from NV centers embedded in a levitated micro-diamond. We use 5 dBm of microwave power.

In order to verify that the Rabi oscillations have the same response to variations of the microwave power as non-levitating diamonds (see section 3.1.6), we measure several Rabi oscillations with different microwave powers and fit them with the function

$$f(t) = 1 - C_1(1 - (C_3 e^{-t^2/\tau_1^2} + C_5 e^{-t^2/\tau_2^2}) \cos \Omega_R t). \tag{3.9}$$

Table 3.23 gives an overview of the parameters used for the fitting these Rabi oscillations. We observe higher decay rates with stronger microwave powers, similarly to what has been shown in section 3.1.6 with diamonds laying on a coverslip.

Power	C_1	Ω_R	C_3	τ_1	C_5	τ_2
10 dBm	0.013	11.1	0.84	133	0.21	1536
15 dBm	0.016	18	0.86	95	0.23	1292
20 dBm	0.017	26	0.90	60	0.31	849

Table 3.1: Parameters used for the fits of the Rabi oscillations as the microwave power varies. The Rabi frequency is expressed in rad/μs^{-1} and the decay times are in ns.

The Rabi frequencies that we obtain are smaller than the one we have attained with a diamond laying on a coverslip. Still, we obtain Rabi frequencies high enough so that a π pulse lasts for about 100 ns. The efficient microwave excitation mainly comes from integration of microwave antenna in the trap set-up and the use of a small ring electrode ($\sim$ 200 µm). Note that a strong microwave drive is a necessary condition to probe the coherence time of inhomogeneous ensembles of NV spins.

Ramsey fringes

We measure Ramsey fringes using the sequence described in figure 3.24.a). Figure 3.24.b) shows the Ramsey fringes that we obtain with different detunings. We fit our experimental data using a sine with a Gaussian decay. We obtain a T_2^* value of 47 ns, which corresponds to an ESR width of 9.4 MHz.

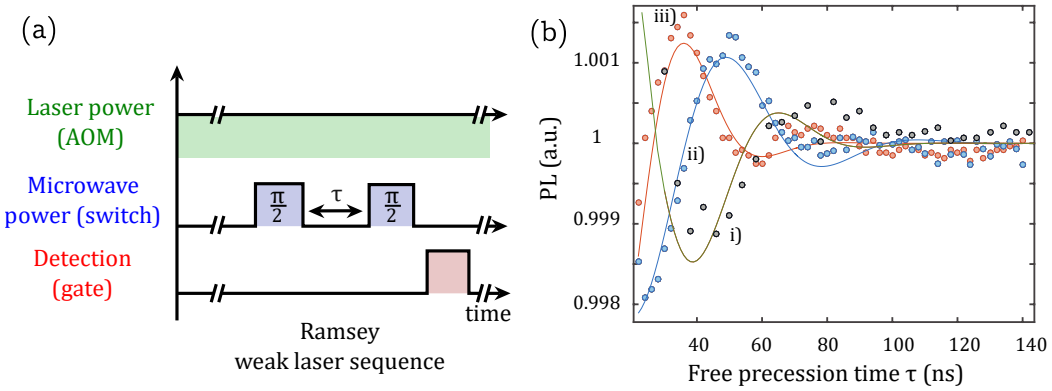

Figure 3.24: a) Ramsey sequence used to measure the T_2^* of the NV spins under weak laser. The axis break symbolises a long waiting time necessary to initialize the spins. b) Photoluminescence as a function of the free precession time for NV spin ensemble in a levitating micro-diamond. The microwave frequency is detuned of (i) 11 MHz (ii) 15 MHz and (iii) 20 MHz from the resonance.

Spin echo

A spin echo sequence can be used to decouple the NV spin from its spin bath, therefore increasing its coherence time. The spin echo sequence that we use is depicted in figure 3.25.a). Figure 3.25.b) shows the photoluminescence of the NV centers as a function of

the precession time. We fit the echo signal with an exponential decay and extract a decay time of 3.3 µs.

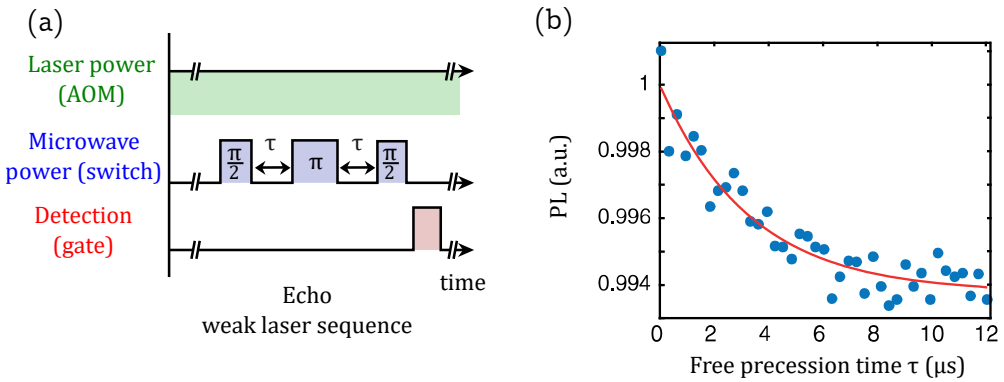

Figure 3.25: a) Echo sequence we use to measure the T_2^{echo} of the NV spins under weak laser. The axis break symbolises a long waiting time necessary to initialize the spins. b) PL as a function of the free precession time for an NV spin ensemble in a levitated micro-diamond.

Conclusion

We have performed measurements of the spin properties of a spin ensemble in a levitating diamond. The lifetime and coherence times (Ramsey, echo) that we have measured show no significant impact of the trap. In this regard, we are however currently limited by the inhomogeneity of our sample: since we did not perform measurement in, and out of the trap for the same particle, we cannot detect variations smaller than the inhomogeneous distribution amongst the micro-diamonds that we use.
Without carrying time consuming calibrations, we can therefore only assert that the spin properties remain in the same order of magnitude: $T_1 \sim$ 1-10 ms, $T_2^* \sim$ 50 ns and $T_2^{\text{echo}} \sim$1-3 µs.

3.5 NV thermometry

We have seen in the previous section that the Paul trap appears not to impact the properties of NV spins. This enables us to fully control them down to mbar pressures, before the micro-diamond starts undergoing rotation driven by the Paul trap (see section 2.5.2). Such pressure ranges are in fact difficult to attain with an optical levitation scheme: the high optical power required to levitate the diamond heats up the internal temperature of the diamond through absorption. As the pressure is lowered, gas collisions cannot cool down the diamond temperature and the particle is eventually lost [64, 66, 67]. Here we will show that this issue is also relevant in our experiment at higher vacuum [122]: we will see that despite the low optical power, the high number of impurities in our diamond still cause heating, which we measure using NV thermometry. We will finally discuss the causes of the heating and give an estimation of whether or not this will limit experiments at higher vacuum in the future.

NV thermometry

Let us first introduce the NV thermometry method. As we have seen earlier, without a magnetic field the degeneracy between the spin ground state $|m_s = 0\rangle$ and excited states $|m_s = \pm 1\rangle$ is lifted by a zero-field splitting of $D \sim 2.87$ GHz due to spin-spin interaction. This coupling strength D is actually highly temperature-dependent and decreases with the temperature [170]. This can be understood intuitively by the two unpaired electron of the spin 1 system being further apart as the diamond is dilated, therefore diminishing the spin-spin coupling rate.

Figure 3.26.a) shows ESR spectra under different pressures with a constant laser power of 50 µW and without a magnetic field obtained from a 10 µm diamond (sampe MSY 8-12). At a given pressure, the ESR is constituted of two unresolved peaks, with the strain partially lifting the degeneracy. As the pressure is lowered, the central frequency of these peaks decreases. One should note that the contrast of the ESR also falls: this is due to an increase of the non-radiative decay from the $|m_s = 0\rangle$ spin state in the excited orbital states, which lower its brightness bringing it closer to the one of the $|m_s = \pm 1\rangle$ states [171].

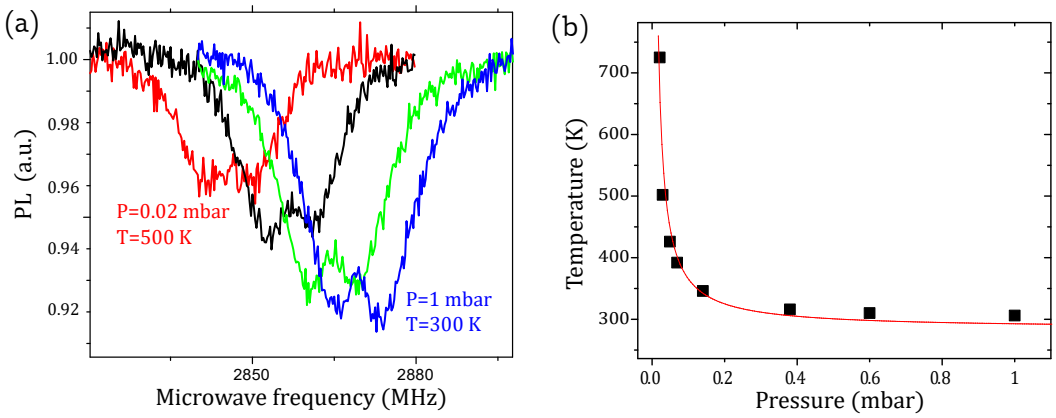

Figure 3.26: a) Electron Spin Resonance (ESR) from a levitated diamond under different pressures ranging from 1 mbar (right) to 0.02 mbar (left), under the same optical excitation. b) NV-measured temperature as a function of the vacuum pressure P. Experimental points are fitted by a first order polynomial in $1/P$.

The internal temperature of the diamond can be obtained from the central frequency of the ESR by describing the zero-field splitting $D(T)$ by a third order polynomial [171]. Figure 3.26.b) shows the dependency of the measured temperature as the pressure is lowered. Temperatures higher than 700 K were measured at $\sim 10^{-2}$ mbar of vacuum pressure. For a given pressure and laser power, we observed that the attained temperature slightly varies from one diamond to another, which is consistent with inhomogeneous impurity density in our samples. We confirmed the heat source to be the 50 µW green laser that we use to observe the diamond and NV centers [122]. Finally we can also see that the temperature evolves as the inverse of the pressure: here gas collisions are the main thermal contact and in this pressure range the cooling rate of the internal temperature is proportional to the vacuum pressure.

High vacuum limitations

In its present form, our system allows for spin control down to 0.1 mbar: below this pressure the system is clearly degraded by heating of the internal temperature. Although this boundary can be pushed by pulsing the laser, as in optical tweezer [66], further changes are still required to work under high vacuum. Two solutions can be envisioned: incorporating an additional cooling mechanism or optimizing the parameters given the current cooling and heating sources.

Regarding the former proposal, optical cooling is possible using anti-stokes emission in rare-earth crystals down to below 100 K [108, 109]. A remarkable experiment recently realized such cooling while levitating a rare-earth crystal [110]. Combining a diamond particle stuck to such rare-earth crystal offers an interesting prospect to mitigate the effect of heating, although such experiment seems challenging (*eg* the high optical power used for optical cooling could be absorbed by the diamond).

In optical tweezers, it was also shown using milled high purity CVD diamonds that the main source of absorption are nitrogen impurities in the diamond crystal [106]. We also made a similar observation: we levitated micro-diamonds with different concentrations of NV centers, 10 µm diamonds with $\sim 10^6$ NV centers (MSY 8-12) and 15 µm diamonds with $\sim 10^9$ NV centers (Adamas MDNV15u). For these samples, we find that heating due to absorption of the green laser occurs at the same vacuum pressure ($\sim$ 1 mbar). Here, the sample containing more NV centers has a higher conversion ratio between nitrogen impurities and NV centers, meaning both samples may contain the same number of nitrogen impurities. While we have not characterize the number of impurities, this result still demonstrates that the NV spins are not the main heating source in the MSY sample.
If one is to rely on gas collisions for dissipation, the relevant parameter is then the number of impurities in the levitating particle divided by its surface. One should note that since the number of impurities is proportional to the volume, working as we do with large, low purity micro-diamonds is particularly disadvantageous. In order to reduce the temperature at higher vacuum, we should therefore work with purer and smaller diamonds. The size of micro-diamond can be reduced by one order of magnitude to 1 µm without altering the NV spin properties while in [106], the purity was improved by three order of magnitudes compared to commercially available nano-diamonds. A rough estimation would therefore yield a gain of four orders of magnitudes for the achievable pressure (10^{-5} mbar) one could reach under reasonable conditions.

3.6 Conclusion

In this chapter, we first presented the physics surrounding the NV spins and the tools commonly used to manipulate them. We then described how one can include them in our trap apparatus, in particular, we used a micro-metric ring playing the role of both the trap electrode as well as the microwave antenna. Interestingly, the NV spins can be used to monitor the angular stability of a levitating diamond by taking advantage of their intrinsic anisotropy. This set-up also allowed us to coherently control NV spins embedded in levitating diamonds and thereby to measure their coherence properties. Under vacuum conditions, we also observed heating of the internal temperature through NV thermometry.

For now this heating happens at a lower pressure (0.1 mbar) than the locked motion (1 mbar, as discussed in previous chapter). If this latter limitation is solved, we expect that working with purer and smaller diamonds will allow the vacuum pressure to be lowered by four orders of magnitude.
To conclude, the ability to coherently control the NV spins in a levitating diamond is representative of the successful integration of the NV spins in the trap set-up: under the right conditions, we can manipulate the NV spins at will in a levitating diamond with stable orientation.

Chapter 4

Spin-mechanical coupling

We have shown the manipulation of NV spins embedded in a levitated diamond, combining a Paul trap with the standard tools used to control NV centers. We have furthermore used NV spins to monitor the angular stability of a levitating diamond, taking advantage of the impact that the orientation of the mechanical oscillator has on the energy of the NV spins. We will now focus on the effect of NV spins onto the mechanical oscillator. In practice those two effects are two sides of the same coin: the spin-mechanical coupling between the NV spins and the angular degrees of freedom of the diamond.

For now, we have used NV spins only to measure large rotation of the mechanical oscillator, with angles in the radians range. We will see in the next chapter that NV spins can also be used to measure the small librations of the diamond. Overall, such measurements take advantage of the efficient spin read-out and the relatively large amplitude of the mechanical oscillations. The impact of a single spin on a macroscopic mechanical oscillator is, in contrast, much more difficult to observe: *eg* it constitutes, in the field of magnetic resonance force microscopy, an experimental tour de force [41]. Our system however has a strong asset: contrary to usual schemes, which rely on a magnetic field gradient to apply a force on an electron spin, we use a homogeneous field and consider the spin-induced torque on the angular degrees of freedom of the mechanical oscillator. We can therefore use large ensembles of NV spins without an additional inhomogeneous broadening that would be created by magnetic field gradients.

In the previous chapter, we have already used spin ensembles with $\sim 10^6$ NV spins, here we will use even larger ensembles. In all the experiments from this chapter, we use the micro-diamonds from the sample Adamas MDNV15u. They have an approximate size of 15 µm and each micro-diamond contains around $\sim 10^9$ NV spins. We will first observe a spin-induced torque applied to the levitating diamond. We will then use this torque to exert a back-action on the mechanical oscillator. In the linear regime this back-action yields a spin-spring effect and spin-cooling of the librations, while in the non-linear regime we observe a bistability and an amplification of the libration motion. We will finally give a theoretical description of the quantum regime, where the NV spins are used to manipulate the librational modes at the single phonon level.

4.1 Spin-induced torque

The simplest action that the NV spins can have on our mechanical oscillator is a spin-dependent torque. Here we consider a simple experiment where both the spins and the mechanical oscillator are in their stationary state hence discarding any dynamical effect. Unlike freely rotating spins from single atoms, an NV spin under a magnetic field applies a torque on the diamond crystal. Its origin lies in the spin-spin interaction of the two unpaired electrons of the NV center and in the structure of its orbitals. Let us first give an idea of the process at play, before laying the formalism that we will use.

As described in the previous chapter, the NV center is a spin triplet system with three eigenstates due to the presence of two unpaired electrons. Without a magnetic field, the magnetic states $m_s = \pm 1$ have a higher energy than the $m_s = 0$ state due to a coupling between the two electron spins of $D \sim 2.87$ GHz. Figure 4.1.a) depicts an NV center in the diamond crystal: in a naive picture, one can consider that the orientation of the two electronic spins is fixed to the NV crystalline axis. Let us consider the magnetic state $m_s = 1$: in the presence of an external magnetic field, a magnetic torque Γ_s is applied to these spins, but because of the spin-spin coupling, the electronic spins do not precess about or align themselves along the magnetic field -as the spin of a free electron would normally do. The magnetic torque is instead transmitted to the diamond crystal itself.
We will now give a more thorough theoretical description of this spin-induced torque, before showing its experimental observation.

4.1.1 Theoretical description

Under our experimental conditions, the levitating diamond contains a large number of NV centers ($N \sim 10^9$) and their orientations are equally distributed along the four crystalline axes of the diamond, depicted in figure 4.2.a). Under an external magnetic field, the energies of these four classes of NV spins will however be non degenerate. By combining green laser illuminations and a microwave field tuned close to the resonance of NV spins along one specific axis, we can therefore ensure that only this class of NV spins are in a magnetic state.

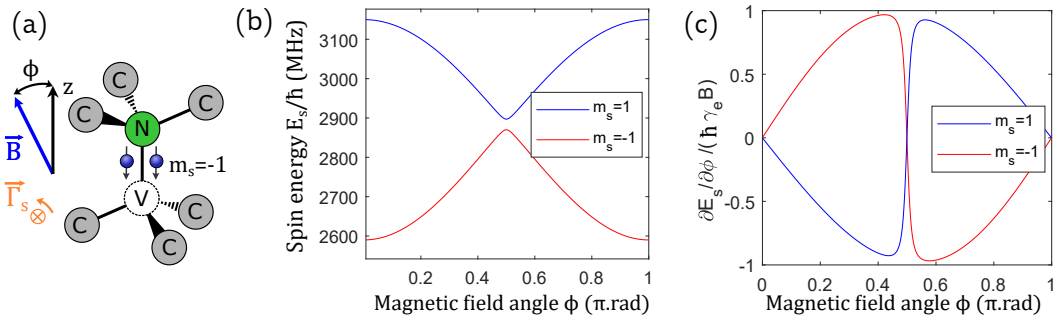

Figure 4.1: a) Simplified picture of an NV center and its spin in the $m = -1$ magnetic state: under an external magnetic field B, a torque $\vec{\Gamma}_s$ is applied to the diamond crystal. b) Eigenenergies E_s for the two magnetic spin states $m_s = \pm 1$ as a function of the angle ϕ between the NV axis and the magnetic field, for $B = 100$ G. c) Normalized derivative of the eigenenergies E_s as a function of ϕ for $B = 100$ G.

NV spin Hamiltonian

Let us write the average spin operators for N spins oriented along the same axis:

$$\hat{S}_\alpha = \frac{1}{N}\sum_{i=1}^{N}\sigma_\alpha^i,$$

where α denotes the three spin directions x, y and z, and σ_α^i are the Pauli matrices of the NV number i corresponding to the direction α.

The Hamiltonian for the NV ensemble aligned along the z direction reads

$$\hat{H}_{\mathrm{NV}} = \hbar N D \hat{S}_z^2 + \hbar\gamma_e N \mathbf{B}\cdot\hat{\mathbf{S}} \tag{4.1}$$

where γ_e is the electron gyromagnetic factor, $\hbar$ the reduced Planck constant, $\mathbf{B}$ the external magnetic field and $\hat{\mathbf{S}}$ the Pauli vector. The first term describes the spin-spin interaction, which is the dominant energy contribution and the second term is the Zeeman energy. Figure 4.1.b) shows the eigenenergies of the two magnetic states $m_s = \pm 1$ as a function of the angle ϕ between the magnetic field and the NV spin orientation. When an NV spin is in a magnetic state, a torque deriving from this energy is therefore applied to the diamond particle. The derivative of the eigenenergies with respect to the angle ϕ and normalized by $\hbar\gamma_e B$ is plotted in figure 4.1.b). We can see that for a moderate field of 100 G, the torque reaches an optimal value close to $\hbar\gamma_e B$ per NV spin (here $\sim 3.10^{-26}$ J, which corresponds to ~ 300 MHz) at an angle ϕ close to $\pi/4$.

New equilibrium position

In order to estimate the effect of the torque in our experiment, we consider a single angular degree of freedom, which is confined by the Paul trap. In the secular approximation the Hamiltonian describing the angular motion resulting from the Paul trap potential reads

$$H_{\mathrm{meca}} = \frac{1}{2}I\omega_\phi^2\phi^2 + \frac{L^2}{2I}, \tag{4.2}$$

where ω_ϕ is the angular frequency of the librational mode that we consider, L the angular momentum of the particle and I its moment of inertia.

We now assume that N spins are in a magnetic state (*eg* $m_s = -1$) and that the magnetic field is at the optimal angle $\phi \sim \pi/4$ so that each spin produces a torque $\hbar\gamma_e B$. For small deviation from this angle, the total energy of the system then reads

$$E = \frac{1}{2}I\omega_\phi^2\phi^2 + \frac{L^2}{2I} - \hbar N\gamma_e B\phi + \mathrm{cte}.$$

The center of the angular potential is thus shifted by the spin-induced torque by

$$\delta\phi_0 = \frac{\hbar N\gamma_e B}{I\omega_\phi^2}.$$

In practice, we consider a 15 µm particle with 10^9 NV spins. Only a quarter of the NV spins are along one of the four directions and only up to 80% of them can be initialized in

a given magnetic state so we have $N \sim 2.10^8$. Taking a typical librational mode frequency of $\omega_\phi/2\pi = 500Hz$ and an external magnetic field of 100 G, we estimate an angle shift of $\phi_0 = 0.1$ rad that should be easily observable given our sensitivity of 0.29 mrad/$\sqrt{\text{Hz}}$ for the detection of the angular position (see section 2.4.2 for estimation, section 4.1.3 -below- for calibration).

4.1.2 Mechanically-detected Electron Spin Resonance

The observation of the torque can be accomplished by comparing the angular position of a levitating diamond with and without a microwave tuned at the magnetic resonance for one orientation of NV spins. We carry out this experimentally by slowly sweeping the frequency of a continuous microwave drive while looking at the angular position of the diamond: at each NV spin resonance, the equilibrium position of the diamond will slightly change.

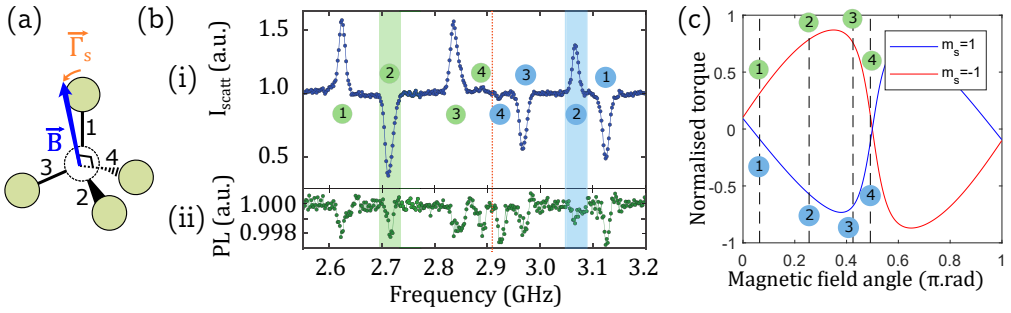

Figure 4.2: a) Vacancy (white circle) in a diamond crystal and its four adjacent lattice site. Each site can be occupied by a nitrogen atom instead of a carbon, yielding the four possible orientations for NV centers. Under an external magnetic field, a torque is applied to the NV spins (Γ_s for NV orientation 1). b) Photo-detector count rate as a function of the microwave frequency for (i) laser light back-scattered by the levitating diamond and (ii) Photoluminescence (PL) collected from NV centers embedded in the levitating diamond. c) Normalized torque exerted on a single NV spin in a magnetic state $\partial E_s/\partial\phi/(\hbar\gamma_e B)$ as a function of the angle between the magnetic field and the NV center orientation.

As depicted in figure 4.2.a), there are four possible orientations for NV centers in the diamond crystal and therefore four pairs of magnetic resonances for NV spins under a magnetic field. Figure 4.2.b) shows the result of a microwave sweep as we monitor the particle. We measure in trace (i) the back-scattered green laser light (proportional to the angular position, see section 2.4.2) while in trace (ii) we observe the NV spins Photoluminescence (PL) executing a standard Optically Detected Magnetic Resonance (ODMR, see section 3.1.3). We can readily identify in the ODMR the four pairs of peaks corresponding to the magnetic resonances. Here the microwave power is kept low so that even at resonance the NV spins are weakly magnetized and the contrast of the ODMR is low ($\sim 0.2\%$). For trace (i), the microwave power is increased and when one class of NV spins is polarized into a magnetic state the spin-induced torque shifts the angular position, which translates into a change of the intensity of the back-scattered light that we collect I_{scatt}. We can clearly see three pairs of peaks, with the two magnetic states $m_s = \pm 1$ of the same NV orientation applying an opposite torque on the diamond therefore resulting in an opposite

signal (*eg* see highlighted peaks).
The fourth pair (labelled 4) produces a much weaker signal, which is explained by the fact that the NV center from this class are almost perpendicular to the magnetic field. Figure 4.2.c) shows the normalized torque applied to a single NV spin depending on its orientation with respect to the magnetic field. Here we have added the angular position of each class of NV centers calculated from the frequencies of their magnetic resonances. We can see that the fourth class produces a much smaller torque than other NV classes.

Note that although the relative strength of the torques explains the weakness of the peaks from the NV class 4, other factors also affect the detected signal. Indeed, spin-induced torques are applied along different axes for each NV class (except for particular symmetric configurations). Since the trap confinement is not the same for the three main axes of the trap, each NV class will produce a different displacement. Moreover, as already mentioned, the angular position sensitivity is not necessarily the same for rotation about different axes. In the spectrum from figure 4.2.b) this explains why the NV classes 2 and 3 -which are expected to produce stronger torques- do not show a stronger signal than the NV class 1.

4.1.3 Calibration of the angular detection sensitivity

Interestingly the ability to apply a controlled torque on a levitated diamond, combined with NV spin magnetometry gives us a means to roughly calibrate the sensitivity to the angular position of our detection scheme. Indeed, an ESR spectrum can be used to determine the angle between NV spins and the magnetic field: several of those spectra carried out while the diamond is at different angular positions (due to a different spin-induced torque) can be used to relate the optical signal that we measure to the absolute value of the angular position.

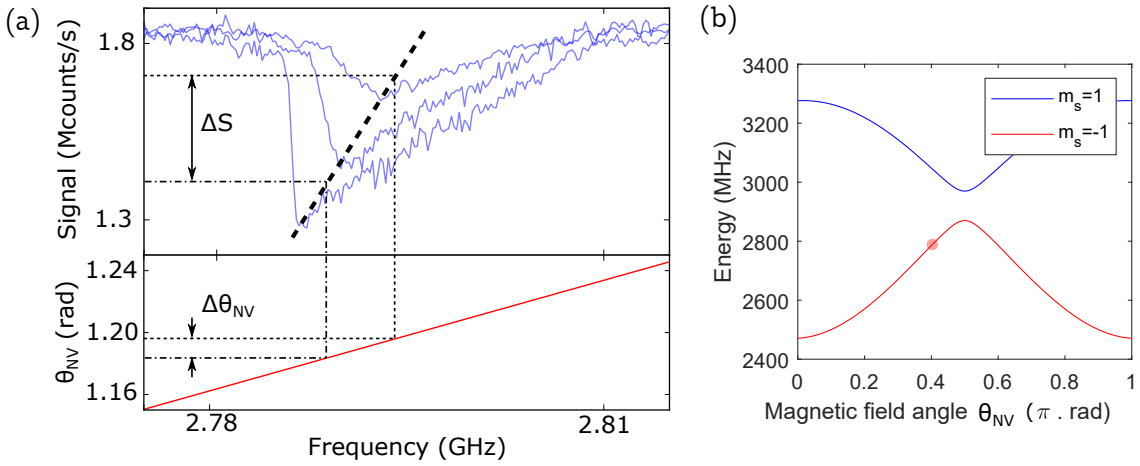

Figure 4.3: a) Upper plot: mechanically-detected ESR spectra for three different microwave powers of (i) -15 dBm, (ii) -25 dBm and (iii) -30 dBm under a magnetic field of 144 G. Bottom plot: angle between the magnetic field and the NV spins as a function of the magnetic resonance energy. b) Energy of the magnetic spin states as a function of the angle θ_{NV} between the magnetic field and the NV for a field of 144 G. The red dot labels the angular position of the NV spins that we observe.

Figure 4.3.a) shows three ESR spectra under 144 G and with three different microwave powers. For a given microwave power, the lower point of the spectra corresponds to the frequency of the magnetic resonance: at this point polarization of the NV spins is the most efficient therefore producing the strongest torque. The frequency of the magnetic resonance is found to depend linearly on the optical signal used to measure the angular position (black dotted line). We then use calculations of the NV spins energy as function of the angle, as shown in figure 4.3.b), to retrieve an absolute measurement of the angle between the NV spins and the magnetic field as a function of the magnetic resonance frequency. This curve is close to linear over the range of angular shifts that we observe, as plotted in figure 4.3.a), bottom plot. We are finally able to relate a variation of our signal (ΔS) to an angular shift $\Delta\theta$ and find a ratio of 43 mrad/Mcounts/s (see figure 4.3.a)). Given our noise level we then estimate our sensitivity to be 0.29 mrad/$\sqrt{\mathrm{Hz}}$.

Note that this calibration is given here as an insight and to provide an order of magnitude: the exact sensitivity varies for each instance of the experiment as the alignment and the speckle patterns change (see section 2.4.2).

4.2 Linear back-action

We have insofar described and shown a static spin-induced torque but the action of the NV spins on the levitating diamond is actually much richer. This stems from the fact that simultaneously to the effect of the spin-induced torque, the modification of the mechanical state of the diamond impacts the NV spins as well. For example, we see in figure 4.3.a) that the magnetic resonance of the NV spins is shifted by around 10 MHz, precisely due to the torque that the spins apply to the mechanical oscillator. Beyond this static case, the NV spins will actually induce a back-action on the libration of the diamond and impact

its dynamics.

We will here describe the back-action applied by the spins to the mechanical oscillator in the linear regime, where we consider small angular displacements. We first describe the expected effects of this back-action on the librational mode. These effects will then be studied in two different experiments: first, in the observation of the relaxation of the excited librational mode and then in the cooling of its thermal fluctuations.

4.2.1 Theoretical description

Let us consider a microwave tuned close to the magnetic resonance of NV spins. For moderate microwave powers, the population of the NV spins in a magnetic state then depends on the detuning of the microwave compared to the magnetic resonance, in fact following the Gaussian shape of the ESR. However, as we have extensively seen, the position of the magnetic resonance varies with the orientation of the NV spins and so with the orientation of the diamond. Since the torque applied by NV spins is proportional to the population in the magnetic state, the torque therefore also depends on the angular position.

This mechanism is analogous to optomechanical systems where the motion of the mirror of a high finesse cavity constitutes a harmonic oscillator [172]. As a detuned laser is injected in the cavity, the radiation pressure applies a force that depends on its detuning, which itself depends on the mirror position therefore yielding a back-action on the mirror position.
The formalism from these well-studied systems can in fact be used in our experiment by replacing the photons inside the cavity by the NV spins in a magnetic state and the mirror position by the micro-diamond angular position.

We will not give in this work the full theoretical description but rather emphasize the causes of the two main effects in the linear case. A complete description of the model that we use to fit our experimental data or simulate the system can be found in the supplementary information of reference [77].

Here we make the following simplifications: we consider a single rotation axis orthogonal to both the NV spins and the magnetic field and only consider small shifts of the angle ϕ around the equilibrium position. We also consider that only two spin states are populated: the $m_s = 0$ non-magnetic state and the $m_s = -1$ magnetic state.

Spin-spring effect

Let us first assume that the spin dynamics is fast compared to the mechanical oscillator. Accordingly, for a constant microwave the spin population in the magnetic state only depends on the angle ϕ. Since the spin-induced torque Γ_s is proportional to this population, it also depends on ϕ.

We therefore obtain that the spin-induced torque derives from the potential energy

$$U_s = -\frac{\partial \Gamma_s}{\partial \phi}\phi^2 + \mathcal{O}(\phi^3).$$

This potential is at the first order a confining or anti-confining harmonic potential (depending on the sign of $\partial\Gamma_s/\partial\phi$).

In optomechanics this effect is named the optical-spring effect: it enhances or diminishes the frequency of the mechanical oscillator when the laser is blue or red detuned respectively. Here we will mention the first order conservative back-action of the NV spins as the spin-spring effect. Its sign depends similarly on the detuning of the microwave compared to the spin magnetic resonance.

Non-conservative torque

The assumption of fast spin dynamics that we previously made is not entirely valid. Figure 4.4.b) and c) show the time it takes for the spin populations to reach their steady state when a resonant microwave is turned off and on respectively. The measurements are carried out using the sequences described in figure 4.4.a) on a levitating micro-diamond. Both time constants are around 100 µs, which is only one order of magnitude faster than the typical period of a libration (1-2 ms).

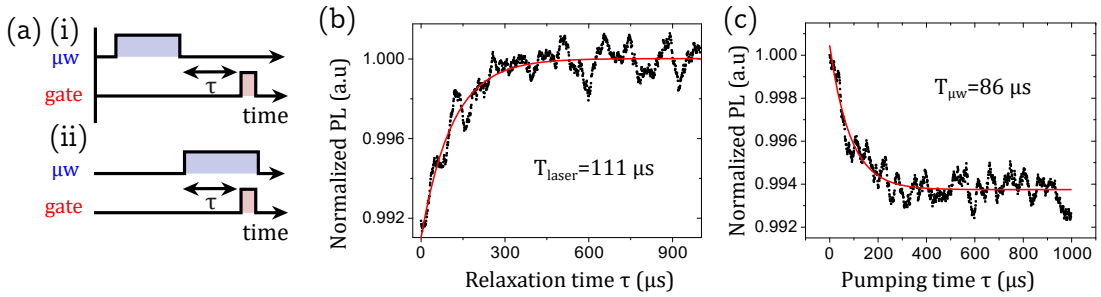

Figure 4.4: a) Sequences used to measure the time necessary for the spin population to reach their steady states when a resonant microwave is turned (i) off and (ii) on. b) Polarization time of the spins in the non-magnetic bright state. c) Polarization time of the spins in the magnetic dark state under continuous microwave pumping (0 dBm). Curves are fitted by exponential decays.

The consequence of this non-zero polarization time is that the population of the spin states also depends on time: they are slightly delayed compared to their steady state -which only depends of ϕ. It follows that the spin-induced torque cannot derive from a potential energy: the spins instead apply a non-conservative torque.

Similarly to the spin-spring effect, the torque will oppose or support the velocity of the particle depending on the sign of $\partial\Gamma_s/\partial\phi$. When the microwave is red detuned, one will expect a cooling of the motion and conversely a blue detuned microwave will cause its amplification.

4.2.2 Ring-down measurements

In a first set of experiments, we excite the mechanical oscillator while observing the relaxation of its angular degrees of freedom. In the underdamped regime -when the damping

rate is lower than the mechanical resonance- one can observe the so-called ring-down of the mechanical oscillation: strong oscillations at the resonance frequency of the oscillator.

Figure 4.5.b) illustrates the sequence we use for a ring-down measurement: starting at the diamond equilibrium position and under a magnetic field, we periodically excite NV spins by turning on and off a microwave with a period of $2\pi/\omega_\phi$, where ω_ϕ is the angular frequency of one librational mode of the levitating diamond. As the spins go from their magnetic state when the microwave is turned on to their non-magnetic state when it is turned off, we apply a periodic torque on the particle. We choose the period of this torque to be resonant with one librational mode so that it is excited far from equilibrium after a few excitations (typically 5). We then let the microwave turned on and observe the angular position of the diamond using the back-scattered light from the diamond. We keep the diamond under continuous green laser excitation during the whole experiment.

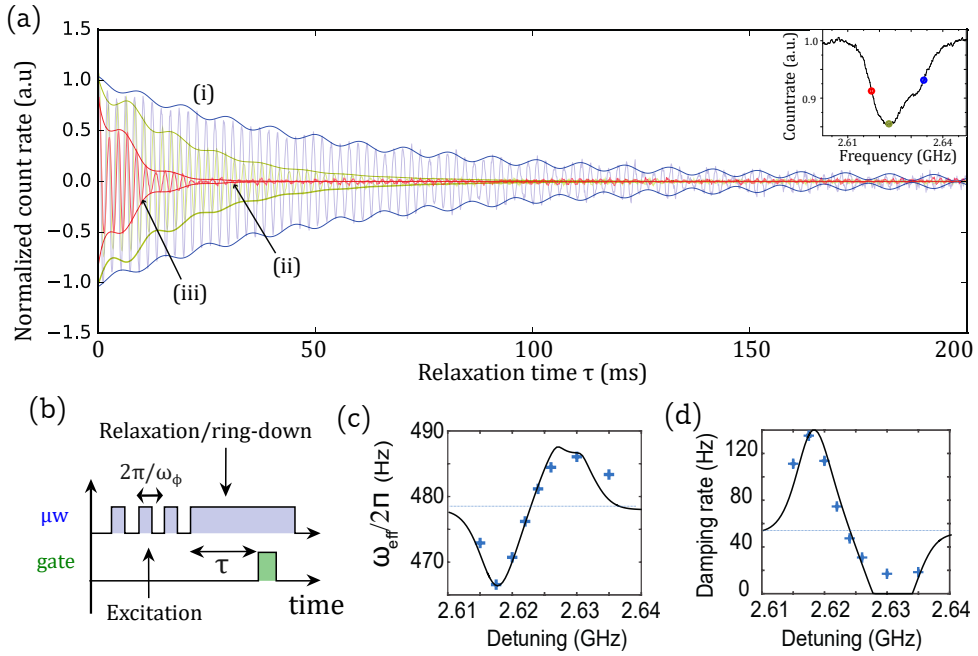

Figure 4.5: a) Ring-down of the librational modes of a levitating micro-diamond observed when a microwave is turned on and (i) blue detuned, (ii) resonant and (iii) red-detuned from the magnetic resonance of a spin ensemble. Upper right caption: magnetic resonance mechanically detected, the three microwave frequencies (red, blue detuned and resonant) are marked by dots on the curve. b) Sequence we use for a ring down measurement. c) Frequency and d) damping rate of a librational mode during a ring-down as a function of the microwave detuning. Lines are simulation according to the model described in [77].

Figure 4.5.a) shows measurement of the ring-down of the librational modes of a levitating diamond for three different microwave frequencies: on the magnetic resonance, red-detuned and blue detuned. The measurements are done at a vacuum pressure of 2 mbar and the ring-down sequence is repeated 500 times for each curve (∼100 s), with a period for the microwave pulses corresponding to a librational mode at 480 Hz. During the relaxation, we observe oscillations of this librational mode with a small contribution from neighboring modes at 590 Hz creating a small beating. We can already clearly see

the change of the damping rate, which depends on the sign of the detuning. In order to extract the values of the damping rates and frequencies, we fit the ring-down with the formula

$$S(t) = A_1 \sin(\omega_{\text{eff}} t + \phi)\exp(-\gamma_{\text{eff}} t/2) + A_2 \sin(\omega_2 t + \phi_2)\exp(-\gamma_2 t/2) + A_0,$$

where ω_{eff} and γ_{eff} are the modified frequency and damping rate of the 480 Hz librational mode and the second sinus describes the other slightly excited mode at 590 Hz.

We carried out such measurements for different detunings and the resulting modified frequencies and damping rates are presented in figure 4.5.c) and 4.5.d). As expected from the theory, the NV spins apply a back-action to the librational mode. First, a conservative effect, the spin-spring effect increases (decreases) confinement when the microwave is blue (red) detuned. Secondly the spins also exert a non-conservative torque that causes the damping rate to decrease (increase) when the microwave is blue (red) detuned. The damping can thus be enhanced by a factor of ~ 3 compared to the damping due to friction with the gas. The experimental points are fitted using the model described in the SI of [77], with a remarkable discrepancy when the damping becomes negative for a blue-detuned microwave. As we will latter see, this corresponds to an amplification of the librational motion which becomes self-sustained (see section 4.3.2). These oscillations appears, however necessarily damped in our ring-down measurement because each iteration of the sequence undergoes a different dephasing over time.

4.2.3 Cooling of the thermal fluctuations

The enhanced damping that we observe during the ring-down of the librations means that thanks to NV spins, the motion of the mechanical oscillator can be cooled down below the thermal fluctuations due to gas collisions. In order to do so, one simply needs to turn a microwave on, red detuned to one of the NV spin magnetic resonance.

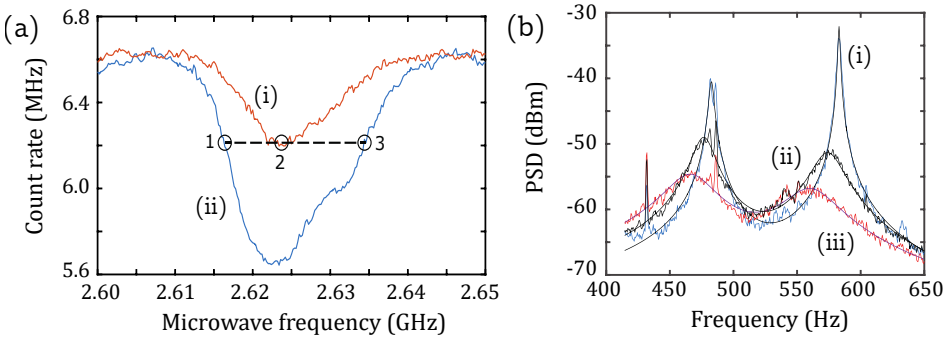

Figure 4.6: a) Mechanically-detected electron spin resonance of a single orientation of NV spins under two different microwave powers (i) -20 dBm and (ii) -10 dBm. The three labelled points correspond to different pairs of microwave frequencies and powers (detuned at -10 dBm and on resonance at -20 dBm) which apply the same torque and for which the angular position is the same. b) Power Spectral Density (PSD) of the optically measured angular position, for three different microwave detunings and frequencies: (i) 2.634 GHz at -10 dBm (blue), (ii) 2.623 GHz at -20 dBm (resonant) and (iii) 2.617 GHz at -10 dBm.

To confirm cooling below thermal fluctuations, we need to measure the temperature of the librational modes. This can be achieved by comparing the Power Spectral Density (PSD) of the angular position of the diamond with and without the red detuned microwave. However in our case the sensitivity of the angular position measurement is not easily calibrated and can vary as the angular position is shifted when we apply a spin-induced torque. We counteract this by realizing three measurements of the PSD at the same angular position with different microwave detunings and powers. Figure 4.6.a) shows the magnetic resonance for an NV spin ensemble in a levitating diamond detected through the shift of the angular position. Under two different microwave powers, we can find three pairs of frequencies and powers (labels 1, 2, 3 on the figure) that induce the same torque on the particle. The particle is then at the same angular position, thereby insuring equal sensitivity for measurement of the angular position and of its PSD.

Figure 4.6.b) shows the PSD of the angular position for these three points. Here, we detect simultaneously two librational modes whose frequencies are close to each-other (480 Hz and 590 Hz), the vacuum pressure is 2 mbar and the spectra are averaged for about 100 seconds. The height of the peaks are clearly smaller for the PSD when the microwave is red detuned, which indicates a lower temperature than when the microwave is resonant or blue detuned.

We fit the data using equations from section 2.4.3, assuming the temperature of the librational modes is 300 K under resonant microwave, we obtain a final temperature of 80 K under a red detuned microwave. As explained in section 2.4.3 we cannot check that without microwave the particle is thermalized by changing the pressure as the sensitivy to angular motion would drift. We however verified that the radiation pressure has a negligeable impact by ramping up the laser power from 100 µW to 1 mW while monitoring the PSD at the same average count rate. We observed no change of the PSD

4.3 Non linear back-action

We now consider the non-linear effects at play when the spin torque is strong enough for the angle to be strongly modified. We distinguish two effects when the microwave is red and blue detuned respectively: bistability and phonon lasing. Once again, the analogy with cavity optomechanics experiments holds and both of these effects can be observed in such systems [172].

4.3.1 Bistability

In our system a bistable behavior arises when the energy shift of the NV spins due to the spin torque is in the same order of magnitude as the linewidth of the electron spin resonance. When the microwave is strongly red detuned, there are then two stable angular positions: one where the microwave is too far from the resonance so the spins are not polarized and the other where the microwave polarizes the NV spins thus generating a torque that is sufficient for maintaining the magnetic resonance close to the microwave frequency.

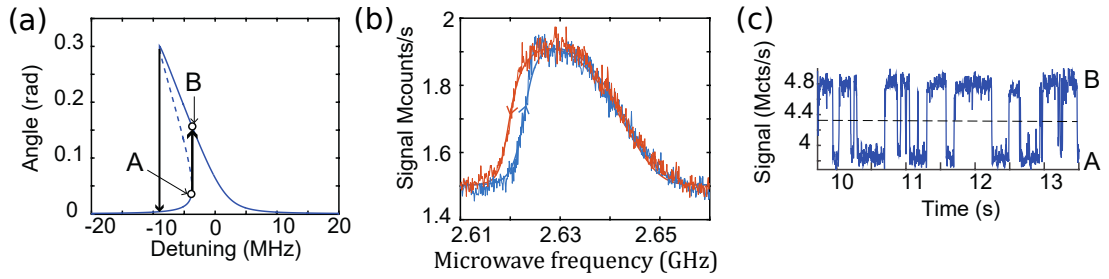

Figure 4.7: a) Expected bistable behaviour: the continuous line shows stable angular position as a function of the detuning from the magnetic resonance. For a range of parameters, two stable sites exist (*eg* A and B). b) Mechanically detected magnetic resonance realized by sweeping towards higher (blue) and lower (red) frequencies. c) Trace of the signal measuring the angular position under a strong red-detuned microwave.

Figure 4.7.a) displays the expected bistability as the microwave is swept across the ESR. When the frequency is red detuned compared to the initial resonance frequency, two stable sites can be found *eg* A and B. The angular position will then depend on the history of the angular trajectory. We observe this hysteretic behavior in figure 4.7.b) where we perform two ESR sweeps from low to high frequencies and from high to low frequencies. The mismatch between the two curves -on the red of the resonance- results from the bistability. These experiments were carried out under atmospheric pressure. Figure 4.7.c) shows the evolution of the angle of a particle as a function of time when the microwave is turned on. We can see that due to thermal fluctuations caused by the Brownian motion of the gas molecules, the particle can jump from one site to the other.

4.3.2 Lasing of a librational mode

We now examine the case of a blue detuned microwave under vacuum conditions. Here the non-conservative torque does not only heat up the particle motion but more singularly amplifies it.

Figure 4.8.a) shows the angular position when a blue detuned microwave is turned on. The experiment is carried out at 2 mbar of vacuum pressure, under a magnetic field of ~ 100 G and we typically detune the microwave 5 MHz from the magnetic resonance. When the microwave is turned on, the motion of the particle changes from thermal motion -governed by collisions with gas molecules- to self-sustained coherent oscillations of large amplitude at the frequency of the librational mode. The signature of this motion is clearly visible in the histogram of the angular position plotted in figure 4.8.b): the particle at rest follows a Boltzmann distribution in the harmonic well while for the amplified motion the distribution tends toward a sinusoidal distribution.

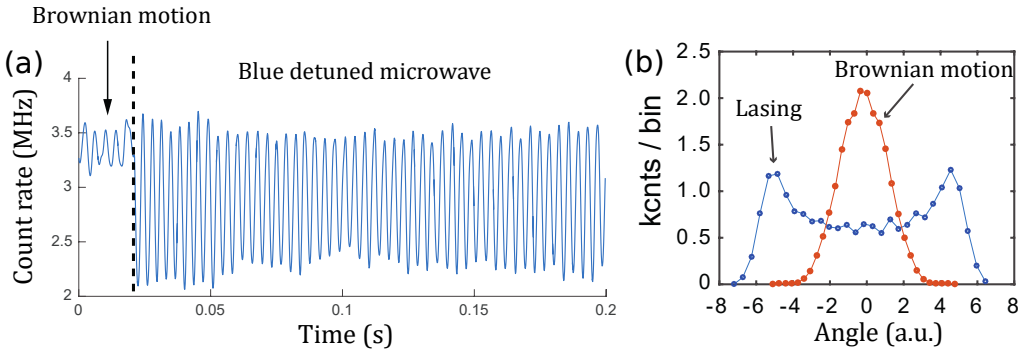

Figure 4.8: a) Evolution of the angular position of a particle when a blue-detuned microwave is turned on (dotted vertical line). b) Distribution of the angular positions for Brownian motion (Boltzmann distribution) and lasing.

This behavior has been previously shown in a Paul trap with a single ion [173] and more recently with a nano-particle levitated in optical tweezers [174]. In the latter experiment, a feed-back loop is used to amplify one mechanical mode, however in both experiments, continuous cooling is applied to all modes in order to introduce non-linearity in the gain and to prevent the particle from escaping the trap. In our case the non-linearity comes directly from the limited width of the ESR: the back-action stops when the spins are too far from the magnetic resonance.
One can describe these experiments as a phonon laser in analogy with the optical laser: here, the NV spins give rise to stimulated emission of phonons in a single mechanical mode therefore creating a coherent oscillation. As for optical lasers, this effect has a power threshold and saturates.

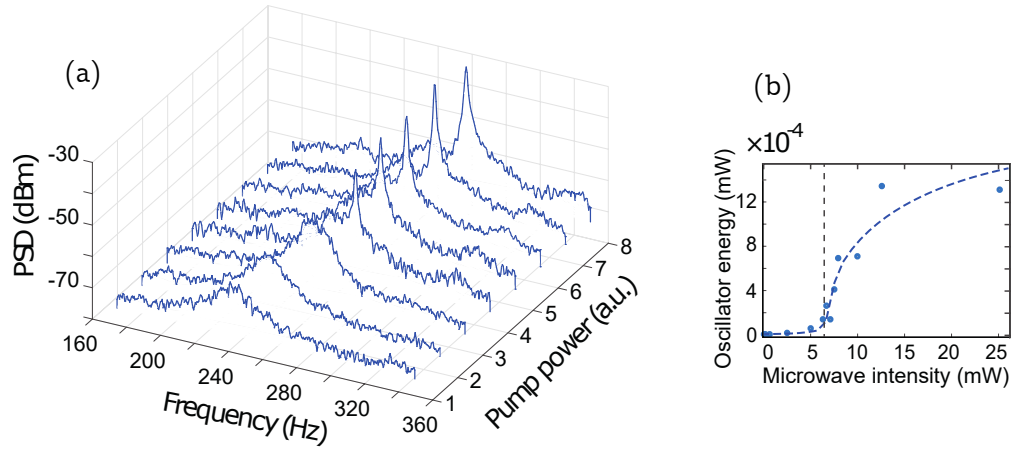

Figure 4.9: a) Evolution of the PSD with the pump power of the blue detuned microwave. b) Threshold behavior of the oscillator energy as a function of the microwave power.

Figure 4.9.a) shows the power spectral density of the angular position of a levitating diamond under vacuum conditions (2 mbar) when the microwave is blue detuned for different microwave powers. A librational mode can be identified at 240 Hz and is found to grow in amplitude as the microwave power is increased. Above a critical value (~ 5), a much sharper peak corresponding to the lasing mode appears in the PSD. This threshold

behaviour is better elucidated in figure 4.9.b) where the energy of the oscillator is plotted as a function of the microwave power: above 5 mW of microwave power, the gain compensates the losses and lasing occurs. The energy in the librational mode then substantially increases until it saturates due to the non-linearity.

4.4 Spin-mechanics in the quantum regime

Inasmuch as the mechanical oscillator in our experiment is in the classical regime, we have so far overlooked the study of the spin-mechanical coupling using quantum mechanics. However, one of the long-term goals of this experiment is to enter the quantum regime where the energy of the mechanical oscillator is quantified. Moreover, the spin-mechanical coupling between librational modes and NV spins was first proposed for ground state cooling and coherent coupling in [73] with a Paul trap and simultaneously in [60] with an optical tweezer. These protocols are largely inspired from a similar theoretical proposal put forward in [43], where the coupling between an NV spin and the center of mass of a cantilever is realized using a strong magnetic gradient.

We will here present a theoretical description of the spin-mechanical coupling between a librational mode and an NV spin in the quantum regime. We consider a single spin for simplicity but as this scheme does not require a magnetic field gradient, it could be extended to an ensemble of spins. We will also consider a magnetic field perpendicular to the NV axis, such condition allowed us to present more comprehensive analytical results in our initial proposal [73]. However working with a different angle should actually yield an increased coupling rate [60].

We will first present the Hamiltonian of the spin-mechanical system and then discuss two main issues: how to increase the coupling and mechanical frequencies above the decoherence rates and how the cooling efficiency is impacted by adverse effects that the transverse magnetic field has on the NV spins.

4.4.1 Spin-mechanical Hamiltonian

The scheme that we propose is depicted in figure 4.10.a): a diamond particle is levitated in a Paul trap (here a needle trap) with an NV spin embedded in it. We consider rotation around the y axis and designate ϕ the shift of the particle's angle from the center of the harmonic confinement. An external homogeneous magnetic field of intensity B is applied and is orthogonal to the NV spin axis when $\phi = 0$. Finally, an oscillating magnetic field at microwave frequencies can be applied along the y axis to control the NV spin and a green laser can be used to polarize the spin in the $m_s = 0$ state.

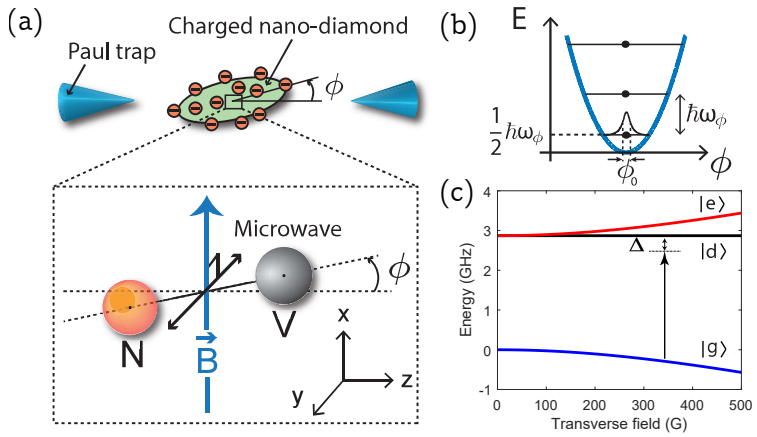

Figure 4.10: a) Scheme for the spin-mechanical coupling between an NV spin and the librational mode of a Paul trap. b) Harmonic potential for ϕ, with the energies of the first phonon Fock states and ϕ_0 the amplitude of the zero-point fluctuations. c) Energies of the eigenstate of H_{NV} as a function of the intensity of the transverse magnetic field.

Quantization of the angular degree of freedom

We quantify the angular degree of freedom similarly to what is done for the center of mass mode of a particle in a harmonic potential well. For small rotations, we consider a harmonic potential for ϕ and the mechanical Hamiltonian reads

$$H_{\mathrm{meca}} = \frac{1}{2} I_y \omega_\phi^2 \hat{\phi}^2 + \frac{\hat{L}^2}{2I_y}, \tag{4.3}$$

where ω_ϕ is the rotational frequency, I_y the moment of inertia with respect to the y axis and $\hat{L}$ the angular momentum.

In analogy with the center of mass mode (see section 1.2), we define the annihilation and creation operators $\hat{a}$ and $\hat{a}^\dagger$ such that $\hat{\phi} = \phi_0(\hat{a}^\dagger + \hat{a})$, where $\phi_0 = \sqrt{\hbar/(2I_y\omega_\phi)}$ is the amplitude of the zero-point fluctuations, and $\hat{L} = I_y\dot{\hat{\phi}} = iL_0(\hat{a}^\dagger - \hat{a})$ with $L_0 = \sqrt{\hbar I_y \omega_\phi/2}$.

Using these operators the Hamiltonian can be rewritten

$$\hat{H} = \omega_\phi \left(\hat{a}^\dagger \hat{a} + \frac{1}{2}\right). \tag{4.4}$$

Its eigenstates are the so-called phonon number Fock states and can be obtained from the ground state using the creation operator:

$$|\mathrm{n}\rangle = \frac{\left(\hat{\mathrm{a}}^\dagger\right)^{\mathrm{n}}}{\sqrt{\mathrm{n!}}} |0\rangle, \tag{4.5}$$

with n a positive integer. The first eigenstates are depicted in figure 4.10.b), their energies are $\omega_{\mathrm{n}} = \hbar(\mathrm{n} + \frac{1}{2})$. Note that the ground state will here have an angular extension ϕ_0 inversely proportional to the square root of the moment of inertia I_y.

NV spin Hamiltonian

The Hamiltonian for the NV spin reads

$$H_{\mathrm{B}}/\hbar = D\hat{S}_z^2 + \gamma_e \mathbf{B}.\hat{\mathbf{S}}$$

where the first term is the zero-field splitting (spin-spin coupling) while the second term is the Zeeman effect. Since the zero-field splitting $D = 2.87$ GHz originates from the diamond crystal and the NV orientation in it, we must write the Pauli vector $\hat{\mathbf{S}}$ and the corresponding Pauli operators in the frame fixed to the diamond.

We obtain the following Hamiltonian

$$\hat{H}_{\mathrm{B}}/\hbar = D\hat{S}_z^2 + \gamma B\left(\sin\hat{\phi}\hat{S}_z + \cos\hat{\phi}\hat{S}_x\right).$$

Considering only the first order in $\hat{\phi}$, the Hamiltonian becomes

$$\hat{H}_{\mathrm{B}}/\hbar = \underbrace{D\hat{S}_z^2 + \gamma B\hat{S}_x}_{H_{\mathrm{NV}}} + \underbrace{\gamma B\phi_0}_{\lambda_\phi}\left(\hat{a} + \hat{a}^\dagger\right)\hat{S}_z. \tag{4.6}$$

We have here distinguished two terms: a spin-only Hamiltonian H_{NV} and the spin-mechanical coupling term characterized by the coupling rate λ_ϕ proportional to the magnetic field.

We first diagonalize the spin-only Hamiltonian H_{NV} and find the eigenstates to be the mixed states

$$\begin{aligned} |d\rangle &= \left(|-1\rangle - |1\rangle\right)/\sqrt{2} \\ |g\rangle &= \cos\theta|0\rangle - \sin\theta|b\rangle \\ |e\rangle &= \sin\theta|0\rangle + \cos\theta|b\rangle, \end{aligned} \tag{4.7}$$

where $|b\rangle = \left(|-1\rangle + |1\rangle\right)/\sqrt{2}$ and $\tan 2\theta = 2\gamma B/D$.
Figure 4.10.c) shows the energies of these mixed states $\omega_{e/g} = 2\pi D\left(1 \pm \sqrt{1 + (2\gamma B/D)^2}\right)/2$ and $\omega_d = 2\pi D$.

A direct spin-mechanical coupling between these states and the mechanical oscillator is however not efficient because the spin-mechanical resonance is not satisfied: the energy between two spin states must match the energy between two phonon states $\hbar\omega_\phi$. Here, at a field of about 0.01 mT (100 G), the two closest spin states $|e\rangle$ and $|g\rangle$ are already dozens of MHz apart.

Microwave-assisted resonance condition

A microwave is thus added to create new eigenstates at the proper energies. Another point of view is that we will use the microwave to drive diagonal transitions between different spin states and different phonon states (the red or blue sidebands). Here, in order to maximize the coupling we will however not drive the spin transitions with a detuning ω_ϕ. Writing the Hamiltonian using the new eigenstates is therefore more relevant.

We set the microwave at a frequency $\omega \sim \omega_{dg} = \omega_d - \omega_g \neq \omega_{ed}$ so that the microwave only drives the transition between the $|g\rangle$ and $|d\rangle$ mixed states, as depicted in figure 4.10.c). The Hamiltonian with the added microwave now reads

$$H_{\mathrm{NV}}/\hbar = D\hat{S}_z^2 + \gamma B\hat{S}_x + \Omega_R\hat{S}_y\cos(\omega t),$$

where Ω_R is the microwave Rabi frequency and $\Delta = \omega - \omega_{dg}$ is its detuning.

In a frame rotating at the microwave frequency it becomes:

$$\hat{H}_{\mathrm{NV}} = \hbar/2\begin{pmatrix} -\Delta & 0 & 0 \\ 0 & \Delta & 0 \\ 0 & 0 & \omega_{e'} \end{pmatrix} + \hbar/2i\begin{pmatrix} 0 & -\Omega_R & 0 \\ \Omega_R & 0 & 0 \\ 0 & 0 & 0 \end{pmatrix}, \tag{4.8}$$

where $\omega_{e'} = \omega_e - (\omega + \omega_g + \omega_d)/2$ and the energy origin has been set to $(\omega_g + \omega_d)/2$.

The new eigenstates of this Hamiltonian are now $|e\rangle$, $|+\rangle = i\sin\psi|g\rangle + \cos\psi|d\rangle$ and $|-\rangle = -i\cos\psi|g\rangle + \sin\psi|d\rangle$, where $\tan 2\psi = \Omega_R/\Delta$ and with $\omega_{+/-} = \pm\sqrt{\Delta^2 + \Omega_R^2}/2$.

We finally obtain a Rabi Hamiltonian, which we write in the $(|e\rangle, |+\rangle)$ subspace for simplicity:

$$\hat{H_{\mathrm{SM}}}/\hbar = \underbrace{\omega_\phi\hat{a}^\dagger\hat{a}}_{\text{mechanics}} + \underbrace{\omega_+|+\rangle\langle+| + \hbar\omega_{e'}|e\rangle\langle e|}_{\text{spin}} + \underbrace{\tilde{\lambda}_\phi\left(\hat{a} + \hat{a}^\dagger\right)(|e\rangle\langle+| + \text{h.c.})}_{\text{spin}-\text{mechanics}}, \tag{4.9}$$

where $\tilde{\lambda}_\phi = \lambda_\phi\cos\theta\sin\psi$ is the effective spin-mechanical coupling rate.

Figure 4.11.a) depicts the $|+, N\rangle$ and $|e, N+1\rangle$ states in the dressed state basis under the resonant condition $\omega_{e'} - \omega_+ = \omega_\phi$. The Hamiltonian 4.9 and more precisely its spin-mechanical part describes a coherent exchange between the phonons of the librational mode and spin states at a rate $\tilde{\lambda}_\phi$.

In practice, two conditions are required to allow such coherent spin-mechanical coupling. First, one needs to be in the resolved sideband regime (RSB), where the frequency of the mechanical oscillator is stronger than the decoherence rate of the NV spin. Secondly, the so-called strong coupling regime must be reached: the spin-mechanical coupling rate must exceed the decoherence rates of both the spin and the librational mode of the mechanical oscillator.

4.4.2 Coupling rate

The effective coupling rate reads

$$\tilde{\lambda}_\phi = \gamma B\sqrt{\hbar/(2I_y\omega_\phi)}\cos\theta\sin\psi, \tag{4.10}$$

in particular, it increases for a stronger magnetic field and smaller particles.

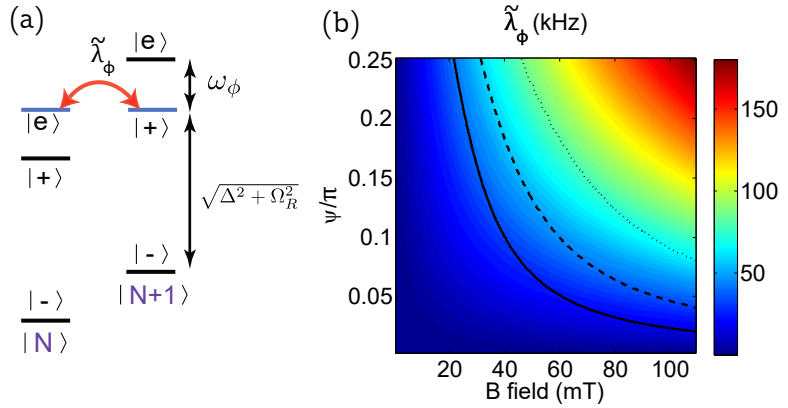

Figure 4.11: a) Level diagram and coupling between the spin states with librational phonon numbers N + 1 and N. b) Coupling rate as a function of the B-field and ψ for $\omega_\phi = 5$ MHz and a 20 nm diameter prolate particle. The black continuous, dashed and dotted lines are the parameter ψ required for the spin-mechanical resonance as a function of the B-field for Rabi frequencies of 250, 500 and 1000 MHz respectively.

Figure 4.11.b) shows the coupling rate $\tilde{\lambda}_\phi$ as a function of the magnetic field and of the ψ parameter, which depends on the microwave Rabi frequency and detuning. Here we consider a spheroid-shaped nano-diamond with a diameter of 20 nm and an aspect ration of 2 (see below, section 4.4.4). The coupling rate can be optimized by taking a resonant microwave ($\psi = \pi/4$) and a strong magnetic field. There is however a practical limitation to these parameters: as the magnetic field is increased, the spin-mechanical resonance condition ($\omega_{e'} - \omega_+ = \omega_\phi$) requires a large splitting $\sqrt{\Delta^2 + \Omega_R^2}$ between the $|+\rangle$ and $|-\rangle$ states. Since it is technically challenging to increase Ω_R above the GHz range [175], one will have to increase Δ, therefore limiting oneself to lower ψ values.

The ψ parameter needed to obtain the resonant condition as a function of the magnetic field given certain Rabi frequencies has been plotted above $\tilde{\lambda}_\phi$ in figure 4.11.b). We find that reaching coupling rates in the 50 kHz range could be feasible under these conditions. Note that we consider here the coupling rate of a single spin: using N spins will enhance the coupling by a factor of $\sqrt{N}$ [60].

4.4.3 Decoherence sources

Before studying how the experiment can be optimized to enter both the sideband resolved regime and the strong coupling regime, we give a small overview of the decoherence sources.

NV spin decoherence

The coherence time T_2 of the spin of the NV center can be written $T_2^{-1} = (2T_1)^{-1} + (T_2^*)^{-1}$ where T_1 is the spin lifetime -longitudinal relaxation- and $(T_2^*)^{-1}$ the inhomogeneous decoherence rate due to the coupling between the NV spin and the nuclear spin bath.
Even for very shallow (5 nm deep) NV centers, T_1 generally ranges from several hundreds of microseconds to milliseconds [164], the main constraint is therefore the T_2^* time.

The decoherence of the NV center spin is described in section 3.1.7. We will here summarize the relevant points. The best NV spin coherence is obtained in bulk, high-purity CVD diamonds made of isotopically purified carbons so as to remove as many nuclear spins as possible [161, 162]. A record-high coherence time of 500 µs was observed using a single NV in a bulk ^{12}C-enriched sample [18].
The NV spins inside nanostructures however suffer from the magnetic noise produced by surface impurities [151, 164], and even working with isotopically purified nano-diamonds implies a T_2^* in the range of a few µs [167].

A longer coherence time can however be recovered by decoupling the NV spin from the spin bath. Using a single decoupling π pulse (Hahn echo sequence) one can then reach coherence times up to 200 µs for 5-nm-deep NV spins and of 800 µs for 50-nm-deep NV spins [165]. That being said, retaining the spin-mechanical coupling sets conditions to the decoupling sequence that we can apply: a dynamical sequence faster than the period of the mechanical oscillator will indeed also decouple the mechanical oscillator from the NV spin and be counter-productive.
It should be noted that in the present protocol, we use a microwave to drive the NV spin at a Rabi frequency $\Omega_R \sim \omega_\phi$ which is in fact already a spin decoupling sequence (spin locking [157]) and will provide decoupling from the spin bath, as mentionned in [43].
Experiments should be carried out on high purity isotopically purified nano-diamonds to precisely determine how efficient this decoupling will be and if it is insufficient, a more advanced protocol could be designed. Still, the results mentioned above (single Hahn echo) indicate that a decoupling frequency in the 10 kHz range (below what is attainable for the mechanical frequency ω_ϕ) should be sufficient to reach a coherence time between 200 and 800 µs depending on the size of the diamond.

Heating rate of the mechanical oscillator

Regarding the mechanical oscillator, the strong coupling regime requires $\tilde{\lambda}_\phi \gg 1/T_2^{\text{mec}}$, where T_2^{mec} is the coherence of the mechanical oscillator. Here, gas collisions will limit the coherence of the mechanical oscillator. Although some theoretical tools are being developed to estimate the decoherence rate [176–178] of librational states, it will highly depend on the shape of the levitating particle, its roughness and eventually the energy potential governing the scattering of molecules impacting it [176]. It can be strongly mitigated at high enough vacuum. Here to give a rough estimate of the heating rate and hence of the lifetime of a mechanical state, we calculate the damping rate of the levitating particle Γ_{gas} due to air molecules in the classical regime.

In the Knudsen regime, when the mean free path of the gas molecules is higher than the size of the levitating particle, one gets [179]:

$$\Gamma_{gas} = \sigma_{eff} \frac{10\pi}{a\rho} \frac{P}{\bar{c}} \tag{4.11}$$

with $\sigma_{eff} \sim 1.1$ the accommodation coefficient, a the radius of the particle, P the pressure in Pa, ρ its density and $\bar{c}$ the molecular velocity of the gas molecules considered. We obtain a relatively low heating rate. For example, we find a heating rate of about 1Hz for a $1\mu m$ radius particle at $P = 10^{-3}$mbar.

4.4.4 Role of the geometry

Both the decoherence rate of NV spins and the spin mechanical coupling rate increase when using smaller particles. The frequency of the mechanical oscillator also increases for smaller particles as mentioned in section 2.1.2. In short this means that micron-size diamonds do not lend themselves easily to spin-mechanics since they are heavier, but they will retain the superior spin properties of bulk diamonds. Conversely, nanodiamonds have shorter coherence time than in the bulk but higher spin-mechanical coupling can be reached. Here we will discuss how to reach a compromise by tuning the geometry of the particles.

The crucial parameters to attain the resolved sideband regime and the strong coupling regime can be extracted from the formulas

$$\begin{aligned} \tilde{\lambda}_\phi = & \quad \gamma B \sqrt{\hbar/(2I_y\omega_\phi)}\cos\theta\sin\psi, \\ \omega_\phi = & \underbrace{\sqrt{\frac{q_0}{2}+\frac{a_0}{q_0}}}_{\text{stability}} \underbrace{\sqrt{\frac{(3+\delta)\,V_{ac}\eta_z}{z_0^2}}}_{\text{Paul trap}} \underbrace{\sqrt{\frac{QS_X}{I_X}}}_{\text{particle}}. \end{aligned} \tag{4.12}$$

Both ω_ϕ and $\tilde{\lambda}_\phi$ depend on parameters that are both intrinsic and extrinsic to the diamond. Because of the $\cos\psi$ term in $\tilde{\lambda}_\phi$, the Rabi frequency Ω_R has to be as large as possible with no detuning Δ. Here we consider $\Omega_R/2\pi = 500$ MHz, which is technically challenging but has been achieved [175]. This in turn limits the intensity of the B-field that we can use while fulfilling the spin-mechanical resonance to ∼30 mT= 300 G.
As discussed in section 2.1.2 the other extrinsic parameters such as the Paul trap parameters V_{ac}, z_0 and Ω can be increased to tune the frequency ω_ϕ. Technical limitations will however set an upper bound: the Paul trap should not be smaller than a few tens of microns and reaching a voltage higher than a few thousands volts at high frequencies will be challenging.

The intrinsic parameters of the diamond particle are then the only parameters we can tune. First of all, the geometry of the diamond must be chosen to minimize the moment of inertia I_y which impacts both the confinement and the coupling. Assuming the charge density on the diamond surface is shape-independent, one must however retain a sufficient surface and asymmetry.

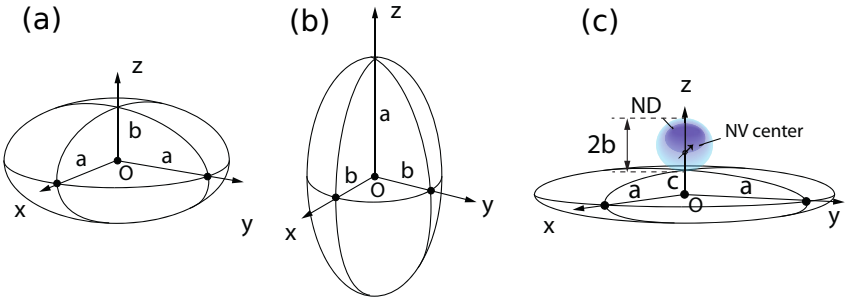

Figure 4.12: Proposed shapes for the levitating particles: a) Diamond oblate spheroid, b) Prolate spheroid and c) Composite particle made of a diamond sphere laying on a thin disk, approximated by an oblate spheroid.

Figure 4.12 depicts three geometries that we propose using: oblate and prolate spheroids, and composite particles formed by a diamond sphere laying on a thin disk. The advantage of the latter composite particle is that the shape and material of the disk can be chosen to optimize the number of charge and the asymmetry while retaining a low moment of inertia and a minimum thickness for the diamond. For all shapes, the b and a parameters always correspond to the minimum and maximum particle radii respectively.

We calculated the trapping frequencies and moment of inertia for these shapes and listed them in table 4.1. They are normalized with respect to the trapping frequencies (ω_0) and moment of inertia (I_0) of a sphere with the same radius b. One can indeed expect similar spin properties for particles with the same minimum radius. The librational frequency is also compared to the center of mass mode ω_{com}, for the same b and for an aspect ratio $a/b = 2.5$. The trapping frequencies are calculated according to the results from section 2.1.2, considering a homogeneous surface charge. Looking at table 4.1, one sees that particles with a higher asymmetry and spatial extent experience a higher libration frequency. They however also have a greater moment of inertia, which will reduce the coupling λ_ϕ. The proposed composite particle comprising a spherical diamond of size b within or deposited on a thinner disk of silica allows to considerably increase the confinement of the particle with a moment of inertia much smaller than with simpler shapes.

particle type	c/b	ω_{com}/ω_0	ω_ϕ/ω_0	ω_ϕ/ω_{com}	I_y/I_0
sphere	-	1	0	0	1
oblate ellipsoid	-	0.64	1.8	2.9	23
prolate ellipsoid	-	0.83	2.3	2.8	9
composite	0.125	2.8	19	5.3	2.4
composite	0.0625	3.3	27.6	6.3	1.2

Table 4.1: Comparison of the mechanical parameters of different particle shapes, as shown in figure 4.12 for the same b, the same aspect ratio $a/b = 2.5$ and an identical surface charge density. ω_0 and I_0 are the secular frequency of the center of mass and the moment of inertia of a sphere with radius b respectively. For each considered particles, ω_{com} and ω_ϕ are the secular frequencies of the center of mass and the librational modes respectively while I_y is the moment of inertia along the y axis.

The last parameter we have not yet tuned is the number of charges on the diamond surface. In order to obtain an order of magnitude for the needed total surface charge, we compute the trapping frequencies according to equation 4.12 obtained in section 2.1.2. The shape and size of the electrodes determine the electric field: we take a needle trap with a distance between the electrodes of 10 μm which yield an efficiency parameter $\eta = 0.3$ and consider a voltage V_{ac}=5000 V at a trapping frequency Ω =5 MHz.

With a prolate nano-diamond of aspect ratio 2.5 and small radius $b = 80$ nm, we find that in order to reach a trapping frequency of 0.5 MHz the diamond surface must host at least 60 elementary charges. This corresponds to about 1000 e/µm^2. In our current experiment, we measure approximately 15 e/µm^2 on the surface of the levitated micro-diamond, which is far from what would be required. Recent experiments with levitated nano-diamonds and a different loading technique however yielded a surface charge of 20000 e/µm^2 [52].

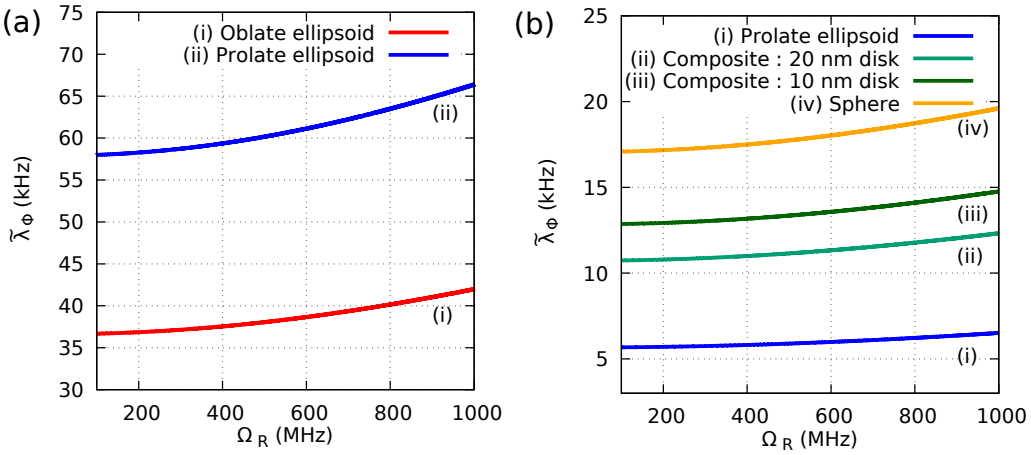

Figure 4.13: Coupling rate $\tilde{\lambda}_\phi$ for nanodiamonds of different shapes, with dimensions and confinement frequencies: a) $b = 20$ nm and $\omega_\phi = 5$ MHz; b) $b = 80$ nm and $\omega_\phi = 0.5$ MHz. The microwave is resonant wirh the $|g\rangle$-$|d\rangle$ magnetic resonance and has a varying Rabi frequency Ω_R. The magnetic field is tuned to match the spin-mechanical resonance condition (*eg* B$\sim$30 mT at $\Omega_R/2\pi$ =500 MHz). The aspect ratio of the proposed particles is $a/b = 2.5$ for all particles and $c/b = 1/8$, $1/16$ for the composite 20 nm and 10 nm disks respectively. The coupling rate for a zero-mass disk (*i.e.* for a sphere) is plotted as a limit for such particles (trace iv).

Let us now estimate the spin-phonon coupling rate for geometries of the particles described above: oblate, prolate or composite particles. We compare two different particle sizes with a minimum radius of 20 and 80 nm. In figure 4.13, the coupling rate $\tilde{\lambda}_\phi$ is plotted as a function of the Rabi frequency. We tune the magnetic field to achieve the spin-mechanical resonance condition. Figure 4.13.a) shows the coupling rate for particles with a radius $b = 20$ nm and and aspect ratio of $a/b = 2.5$. As expected we obtain a better coupling with a higher Rabi frequency as it allows a higher magnetic field under the resonance condition. Here for a Rabi frequency $\Omega_R/2\pi = 500$ MHz and a magnetic field $B \sim 30$ mT, $\tilde{\lambda}_\phi$ ranges between 35 to 60 kHz. In figure 4.13.b) we consider particles with a larger radius of $b = 80$ nm. Due to the high mass, the coupling rate is then smaller, barely exceeding 5 kHz. It can however be increased using a composite particle made out of a silica pancake-like shape with a nanodiamond laying on top. The coupling strength will then depend crucially on how thin the disk of the composite particle can be.

4.4.5 Cooling efficiency

We have for now solely focused on the conditions for obtaining a coherent spin-mechanical coupling, which would allow us to fully control the mechanical oscillator at the single phonon level using NV spins. This proposal then relies on an efficient control of the NV spin in order to first cool down the mechanical oscillator to its ground state and from there generate an arbitrary mechanical state. We focus here on the efficiency of the cooling mechanism: the ability to reach the ground state is a key to more advanced protocols.

A cooling scheme can be set up similarly to [43] by adding an optical field to excite the NV electronic states. Optical pumping polarizes the spin state to the $|0\rangle$ state through

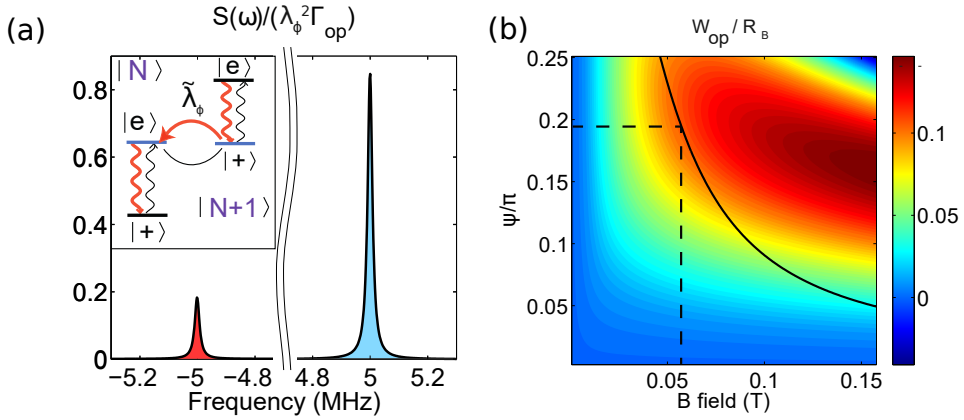

Figure 4.14: a) Spin excitation spectrum showing the emission ($\omega < 0$) or absorption ($\omega > 0$) of phonons under resonant conditions $\omega_{e'} - \omega_+ = \omega_\phi$. The inset shows the cooling mechanism as a cascade between the dressed states from librational phonon numbers $N+1$ to N. The parameters are: $B = 2.6$ mT, $\Omega_R/(2\pi) = 0.5$ MHz, $\Delta/(2\pi) = 3$ MHz and Γ_{op} =10 kHz. b) Normalized cooling rate as a function of the B-field and Ψ/π for Γ_{op}=100 kHz and $\omega_\phi/(2\pi)$=5 MHz. The black line is the ψ parameter under the resonance condition as a function of the B-field for $\Omega_R/(2\pi) = 1$ GHz.

non-radiative decay via a metastable state [142] (see section 3.1.3). This process is at the core of the cooling scheme which extracts energy from the librational mode using the NV spin. Note that the transverse magnetic field mixes the $|0\rangle$ and $|\pm1\rangle$ states, which lowers the polarization efficiency.

To obtain the cooling rate, we calculate the fluctuation spectrum of $\hat{S}_z$, taking into account both the unitary evolution (magnetic field, microwave) and the dissipative process (laser polarization) [43, 180]. We present, in annex B, the full derivation which includes the excited orbital states and the metastable states to account for the influence of the transverse magnetic field in both the ground and excited orbital manifold.

The optical polarization into the $m_s = 0$ state results in unbalanced populations between the $|+, N+1\rangle$ and $|e, N\rangle$ states from the Hamiltonian 4.9. The spin-mechanical coupling will thereby enable continuous cooling through spin-mechanical coupling, as depicted in the inset of figure 4.14.a). Figure 4.14.a) shows the fluctuation spectrum $S(\omega)$ of $\hat{S}_z$ under 2.6 mT of transverse magnetic field and the spin-mechanical resonance. A clear asymmetry is obtained between the negative frequency part (heating) and positive frequency part (cooling) of the spectrum showing that cooling dominates. Figure 4.14.b) shows the normalized cooling rate W_{op}/R_B, where $R_B = (h\gamma B_0\phi_0)^2/\Gamma_{\text{op}}$, $B_0 = 60$ mT and $W_{\text{op}} = S(\omega_\phi) - S(-\omega_\phi)$ when varying the B-field and the microwave detuning (ψ parameter). The highest cooling rate is achieved for $\psi/\pi = 0.15$ and under strong magnetic fields. As mentionned before, there is however a practical limitation to accessing this range of parameters: as the magnetic field is increased, the resonance condition ($\omega_{e'} - \omega_+ = \omega_\phi$) requires a large splitting $\sqrt{\Delta^2 + \Omega_R^2}$ between the $|+\rangle$ and $|-\rangle$ states. Since it is technically challenging to increase Ω_R above the GHz range [175], one will have to increase Δ therefore limiting oneself to lower ψ values.

To study how the cooling efficiency varies with the B field and microwave parameters, we now look for the phonon mean occupation number. The ψ parameter that allows

resonant conditions for a Rabi frequency of 1 GHz is plotted in figure 4.14.b) as a function of the magnetic field. This line shows that for such a Rabi frequency the cooling rate reaches an optimum for a magnetic field of only 60 mT, as shown by the dashed lines. We will use this value to extract the final phonon occupation number under continuous cooling. The mean phonon number is given by :

$$\langle n \rangle_0 = \frac{A_{\rm op}^+ + W_{\rm gas}}{W_{\rm op}}, \tag{4.13}$$

with $A_{\rm op}^+ = S(-\omega_\phi)$ the optical heating rate and $W_{\rm gas}$ the heating rate due to collisions with a residual gas [43]. The heating rate due to gas collision was estimated in section 4.4.3 to be about 1 Hz at 10^{-3} mbar.

Here, we consider a diamond of 70 nm diameter under a vacuum pressure of 10^{-8} mbar. Under a magnetic field $B_0 = 60$ mT, with a Rabi frequency of 1 GHz and an optical excitation rate $\Gamma_{\rm op} = 100$ kHz, the final phonon number is found to be $\langle n \rangle_0 = 10.7$, far from the ground state. The mechanism limiting this number is not heating by gas collision but the mixing of the spin states, which prevent us from reaching the usually high polarization efficiency of NV spins. An option to get closer to the ground state is to tune the B-field again. Provided $W_{\rm gas}$ is much smaller than $W_{\rm op}$, we can decrease the B field and even though the cooling rate will be lower, a lower $\langle n \rangle_0$ will be reached due to a better polarization efficiency.

For a Rabi frequency of 0.5 MHz at a magnetic field of 2.6 mT and with $\Gamma_{\rm op} = 10$ kHz we actually find a final phonon number $\langle n \rangle_0 = 0.30$, close to the ground state. Those conditions differ from the one derived to obtain a coherent spin-mechanical coupling. In its current state, this proposal therefore requires a pulsed scheme where one would ramp up and down the magnetic field between cooling/spin polarization stages and spin-mechanical coupling stages. Although this adds experimental constraints, the high lifetime of both the NV spin and the mechanical oscillator only impose them relatively long timescale (ms).

Conclusion

In this chapter, we have successfully observed the coupling of spin ensembles to the motion of levitated micro-particles. Here, a key point is that we exploit the angular degree of freedom to achieve coupling between the NV spins and the libration of the particle under a homogeneous magnetic field. We are therefore able to use large spin ensembles, whereas for the center of mass motion, strong magnetic gradients entail the use of a single spin.

We first observed a spin-induced torque, which depends on the state of the NV spins. The long lifetime of the NV spins then enabled us to cool down the librational modes of a levitating diamond to about 80 K, despite a relatively low frequency for the mechanical oscillator. In strong analogy with cavity opto-mechanics, we also observed a broad range of effects, including a spin-spring effect, bistability and lasing of the librational modes. Finally, we theoretically described this spin-mechanical coupling in the quantum regime. It is similar to sideband cooling, although our experimental scheme is, for now, far from the resolved sideband regime. Further, we derived the conditions to enter the sideband resolved and strong coupling regimes, which are required to achieve ground state cooling. We found that reducing the size of the levitating diamonds and improving their purity

would allow those conditions to be satisfied.

Chapter 5

Levitating ferromagnets

The spin-mechanical effects that we have observed show that the NV spin is a potent system to manipulate the motion of a levitating particle. However, the low frequency of our mechanical oscillator limits for now these effects. Working with smaller particles could leverage this issue but does require non-trivial experimental progress regarding the injection mechanism. Ferromagnetic particles provide an additional access route to enhance the frequency of the librational modes of a levitating oscillator.

In this work, levitation of ferromagnetic particles is carried out using a Paul trap, but other trapping mechanism could also be used to observe the enhanced confinement that we describe. Just like the Laplace equation shows a charged particle cannot be trapped solely by an electric field, the Earnshaw theorem shows that a magnetic field alone cannot confine a magnet in three dimensions. This constraint can however be bypassed by building a magneto-gravitational trap where two dimensions are confined solely by the magnetic force while gravity provides confinement for the third dimension [181]. In practice this is realized by using the repulsive force between a ferromagnetic material (usually a magnet) and a diamagnetic one. Both diamagnetic and ferromagnetic particles can be levitated this way. Objects from a living frog [181] to micro-particles [182, 183], nano-diamonds[49, 184] or silica nanospheres [185] were thus levitated. One can then use electric or magnetic forces to control their motion, in particular, cold damping for center of mass motion reached mK temperature [49, 184, 185] thanks to ultra high-vacuum [185]. Because of weak diamagnetism, the frequency of the center of mass motion in magneto-gravitational traps is however low (100 Hz). In this regard working with the angular degree of freedom could be quite oportune: using a homogeneous field one can apply a strong confining torque to a levitating magnet.

In this chapter, we will first elaborate on the theoretical principle of magnetic confinement of the angular degrees of freedom, before showing experiments with levitated ferromagnet and hybrid particles composed of a ferromagnet combined with a diamond.

5.1 Magnet libration in a hybrid trap

A ferromagnetic particle that aligns itself with an external magnetic field is in essence a compass. However, when the particle size is in the micron range, the magnetic torque becomes strong compared to the inertia momentum of the particle, resulting in a high

frequency mechanical oscillator.

In our case, we use a hybrid trap: the center of mass is confined as in previous chapters by a Paul trap while the magnetic field provides an additional angular confinement. We first describe confinement of hard ferromagnets before moving to the case of soft ferromagnets. Although the latter do not provide a confinement as strong as the former, its experimental implementation is less challenging: the experiment presented in the next section were indeed carried out using soft ferromagnets.

5.1.1 Hard ferromagnet

Let us consider a particle of volume V and magnetisation M that is submitted to a homogeneous magnetic field $\vec{B} = B\vec{e}_y$. For simplicity we will consider only one angle of rotation ϕ, around the x axis and assume the other angular degrees of freedom to be frozen. In practice, two angular degrees of freedom are confined by the magnetic field while confinement of the third one (rotation around the magnetic field) solely relies on the Paul trap.

Figure 5.1.a) depicts a levitated magnet under a homogeneous magnetic field. When $\phi = 0$ we take the magnetisation anti-aligned with the y axis. Let I_ϕ be the inertia momentum of this particle along the x axis, the magnetic energy and magnetic torque applied to this particle are then:

$$\begin{aligned} E_m &= -\frac{BVM}{\mu_0}\cos\phi \\ \Gamma_m &= \vec{M} \times \vec{B}, \end{aligned} \tag{5.1}$$

where $\mu_0 = 4\pi \times 10^{-6}$ T.m/A is the vacuum permeability, B and M are in Tesla and V is the volume of the particle in m^3.
In the small angle approximation we therefore obtain near-harmonic confinement for ϕ:

$$\begin{aligned} E_m &= \frac{I_\phi}{2}\omega_\phi^2\left(\phi^2 - 1 + \mathcal{O}\left(\phi^4\right)\right) \\ \omega_\phi &= \sqrt{\frac{BVM}{\mu_0 I_\phi}}. \end{aligned} \tag{5.2}$$

We now see that the angular frequency of the confinement ω_ϕ scales as the inverse of the size of the magnet. We apply this formula to a spheric neodynium magnet with a magnetisation $M = 1.4$T and a volumic mass $\rho = 4.5 g.cm^{-3}$ under an external field of 1000 G. We find confinement frequences $\omega_\phi > 2\pi \times 100$kHz with a $10\mu m$ radius particle and $\omega_\phi > 2\pi \times 1$MHz with a $1\mu m$ radius particle.

Levitation of micro-magnets is however not a trivial task: although one can fabricate magnets in the micro-size range, they tend to aggregate due to magnetic forces if they are too close to each other and if one tries to inject a single one in a trap it is likely to remain stuck on the fabrication substrate because of van der Waals forces [182]. So far, experiments with levitated micro-magnets have mostly used magnetic traps. In [186], a ~ 25 µm hard ferromagnet was levitated above a superconductor, only weak fields were however applied to the magnet because any external magnetic field is shielded by the superconductor.

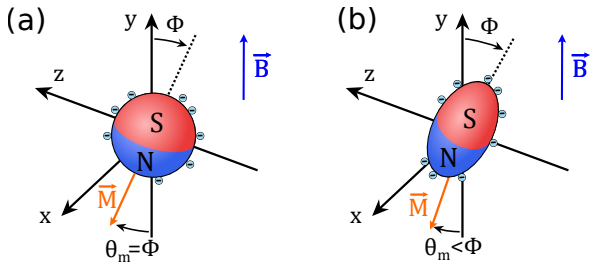

Figure 5.1: a) Round hard and b) asymmetric soft ferromagnets levitating *via* electric forces. Under a homogeneous external magnetic field the magnetic moment of both particles anti-aligns itself with the field due to the magnetic torque. The hard ferromagnet has its magnetic moment fixed to the particle axes (below coercitive fields), the magnetic moment of the soft ferromagnet lies between the magnetic field z axis and the long axis of the particle. θ_m is the angle between the z axis and the magnetic moment, ϕ is the displacement of the particle from its equilibrium position.

5.1.2 Soft ferromagnets

Using a magnetic-field-free trap (*eg* a Paul trap) and soft ferromagnetic particles provides an appreciable escape route from the above-mentioned obstacles. A soft ferromagnet is characterized by a very small remanent magnetization: the material acquires a magnetization when subjected to an external magnetic field but loses most of it if the external field is turned off. One can therefore use a large number of soft ferromagnetic particles, inject them in a Paul trap and only then turn the magnetic field on.

Here we consider a soft ferromagnetic particle levitating in a Paul trap. The amount of anisotropy determines how much the magnetic moment of a soft ferromagnet deviates from the external magnetic field. For example one could use crystalline anisotropy, but here we consider prolate spheroid (ellipsoid of revolution) and only take into account their shape anisotropy. The calculation of the magnetisation and the resulting torque for such particles have been treated both theoretically and experimentally in [187].

Let us note ϕ the angle between the long axis of the ellipsoid and the external magnetic field as described in figure 5.1.b). When the external magnetic field is weak enough so the ferromagnet doesn't reach its saturation magnetization, the magnetic moment of the particle will align itself in-between the external magnetic field and the particle long axis giving rise to a magnetic torque T. The magnetic torque T applied to a spheroid of long axis a and short axis b can be obtained from the formula [187]:

$$T(\phi) = \frac{V(n_r - n_a)}{2\mu_0 n_a n_r} B^2 \sin(2\phi), \tag{5.3}$$

where a and b are the long and short radii respectively, $V = \frac{4\pi}{3}ab^2$ is the volume of the particle, μ_0 is the vacuum magnetic permeability and n_r, $n_a \in [0, 1]$ are the so-called demagnetisation factors. Those are purely geometrical and can be calculated analytically for ellipsoidal bodies [188]:

$$\begin{aligned} n_a &= \frac{1}{R^2-1}\left(\frac{R}{2\sqrt{R^2-1}} ln\left(\frac{R+\sqrt{R^2-1}}{R-\sqrt{R^2-1}}\right) - 1\right) \\ n_r &= \frac{1}{2}(1 - n_a), \end{aligned} \tag{5.4}$$

where $R = a/b > 1$ is the aspect ratio of the particle. This expression of the torque is valid for a soft ferromagnetic material with large magnetic susceptibility ($\chi \gg 1$) and a magnetic field such as

$$B < \mu_0 m_s \frac{n_a n_r \sqrt{2}}{\sqrt{n_a^2 + n_r^2}}$$

where m_s is the magnetisation at saturation of the material. It is quite remarkable that, under those conditions, the torque does not depend on the magnetic properties of the body but only on its geometry.

From kinematics principles, we find that the confinement frequency for the angle ϕ resulting from the magnetic torque T_{soft} is given by

$$\omega_\phi = \sqrt{\frac{V(n_r - n_a)}{I_\phi \mu_0 n_a n_r}} B \tag{5.5}$$

where $I_\phi = \rho V(a^2 + b^2)/5$ is the relevant component of the particle moment of inertia and ρ is the particle density.

The angular confinement frequency is proportional to the applied magnetic field and, for a given aspect ratio, it is inversely proportional to the particle size. This latter property can be seen by writing

$$\frac{V}{I_\phi} = V^{-\frac{2}{3}} \frac{5}{\rho} \left(\frac{4\pi}{3}\right)^{\frac{2}{3}} \frac{R^{\frac{2}{3}}}{R^2 + 1}.$$

Two opposing effects impact the dependency of confinement on the aspect ratio: when the particle is more elongated its torque is stronger but so is its moment of intertia. An optimum is actually found at the value of $R \approx 2.606$ [76].

Under an external field of 1000 G and for pure iron with a volumic mass $\rho = 7.86.cm^{-3}$ we obtain a confinement frequency of $\omega_\phi \approx 2\pi \times 150$ kHz for a particle of dimensions 4μm $\times$ 10.4μm. For submicron particles, frequencies higher than the MHz are attainable.

5.2 Libration of iron rods

As mentioned above, we focused on soft ferromagnets to avoid the experimental constraints associated with hard ferromagnets. In the first experiments we carried out, we inject iron particles in a Paul trap, assemble them *in situ* into rods and observe their librational mode following excitation during a ring-down sequence.

5.2.1 Levitation of asymmetric iron particles

The set-up used for levitation, visualization and vacuum conditions is the same as already described in section 2.2. Here the trap electrodes that we use are rings of varying sizes, mostly in the 150-300 µm range for the inner diameter. We levitate particle made of 98% pure iron that have a spherical shape (Goodfellow, ref. FE006045). Figure 5.2 shows a scanning electron microscopy image of these particles: although their diameters is rated to be from 1 to 6 µm, we observe that it varies roughly from 0.5 to 3 µm with most of the particles having a diameter around 1 µm.

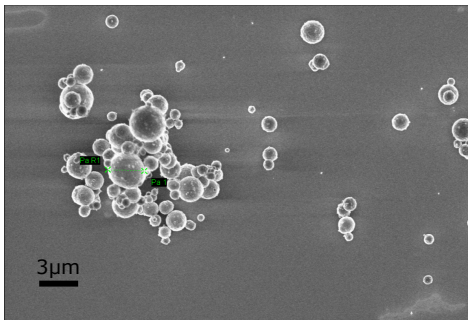

Figure 5.2: Scanning electron microscopy image of iron micro-spheres laying on a coverslip.

As explained in previous section we aim at using the shape anisotropy of the levitated particle to fix its magnetic moment to the particle axes. We obtain asymmetric particles from our sample by assembling several levitated iron sphere in the Paul trap.
In order to do so, we proceed as follows:

1. We inject several iron particles simultaneously in the Paul trap. A large enough trap can simultaneously levitate tens of particles that form a Coulomb crystal [189] as they are both attracted toward the trap center but repulse each other.

2. We eliminate all but a few particles (typically 2-4) by lowering the trap potential.

3. We increase the Paul trap confinement by tuning the trap frequency and voltage to decrease the distance between each particles.

4. We apply a magnetic field by bringing manually a permanent magnet next to the trap. Each particle becomes magnetized thereby creating attractive forces between the particles. For a sufficiently high magnetic field, of the order of hundreds of Gauss, magnetic forces overcome the repulsive electrostatic ones and the particles bind together, forming a rod aligned with the direction of the magnetic field.

During the assembly, the eventual presence of charge patches of different polarities on the particles might assist the binding process by mitigating the Coulomb repulsive forces. This method allows us to obtain elongated rods as such shape minimize the magnetic energy.

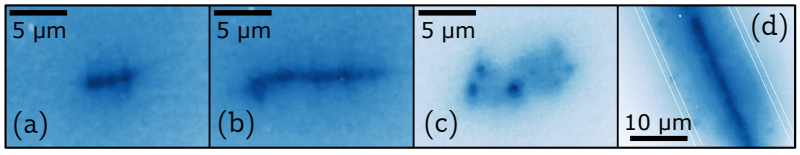

Figure 5.3: Images of a), b), c) a levitated micro-rod and d) a 15 µm wire taken for calibration of the magnification.

We characterize the size and shape of the levitated particle by shining incoherent light onto the particles and use the aspheric lens to image the particles onto a CCD camera. Figure 5.3.a-c) shows images of levitated rods obtained using this imaging system, we calibrate its magnification by imaging a 15 µm wire (figure 5.3.d)). We obtain elongated rods, ~ 4 µm long for the shorter one and 15 µm long for the larger one.

5.2.2 Ring-down of the librational mode

We observe the librational mode of a levitated ferromagnetic particle *via* its ring-down following an excitation sequence. The ring-down of the mechanical oscillator can be observed in the underdamped regime: when the damping rate is lower than the mechanical resonance. Here, contrary to the case of a levitating diamond, the libration occcurs at a higher frequency than the damping rate even under atmospheric pressure. Most ring-down experiments therefore do not require vacuum conditions and are carried out under atmospheric pressure.

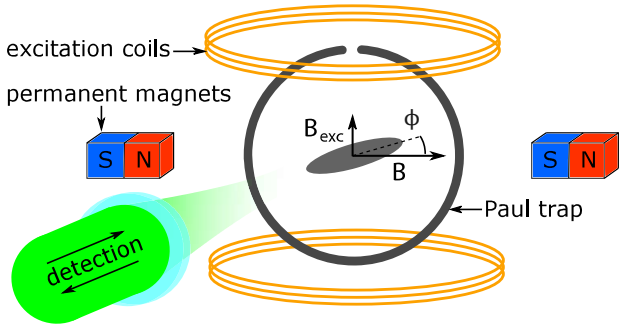

Figure 5.4: Set-up for a ring-down measurment: permanent magnets generates a static homogeneous magnetic field B while two coils in a Helmotz configuration generates a time varying homogeneous field B_{exc}.

Figure 5.4 describes the set-up allowing excitation of the librational mode and observation of its ring-down. We generate the static magnetic field which confines the angular degree of freedom with two permanent magnets positioned in a Helmholtz configuration on each side of the trap at a distance of ∼1-5 cm. The magnetic field gradients are thus minimized: at high field, when the magnets are brought close to the levitating particle, the magnetic force of a single magnet would pull the particle out of the trap.

The optical set-up is similar to the one described for levitating diamond in section 2.2: we focus a green laser close to the particle using an aspheric lens. This allows direct visualization (see section 2.2.1) as well as measurement of the angular position of the magnet ϕ, using the speckle pattern of the back-scattered light (see section 2.4.2).

Finally two coils are placed on top and at the bottom of the trap in a Helmholtz configuration to generate a homogeneous time varying magnetic field B_{exc} in a direction perpendicular to the static magnetic field. Applying a current on the coils changes the orientation of the magnetic field and therefore rotates a levitating iron rod out of its initial equilibrium position.

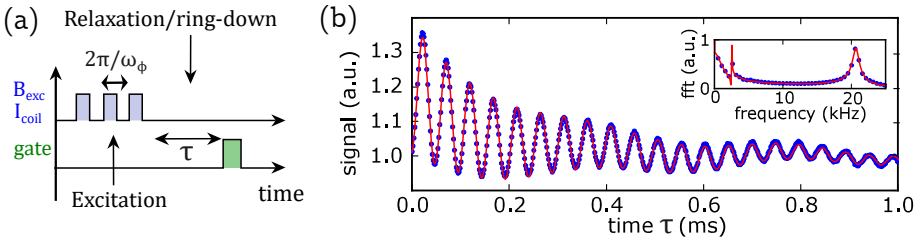

Figure 5.5: a) Ring-down sequence: I_{coil} generates a periodic exciting field B_{exc} and we detect the following ring-down of the mechanical oscillator at the frequency ω_ϕ. b) Ring-down of an iron rod under atmospheric pressure. Points are experimental datas and the solid line is a fit. The inset shows the Fourier transform of the temporal signal.

Figure 5.5.a) depicts the sequence that we use to observe the ring-down of the librational mode. We switch the current (0.5 A) in the coils on and off a few time (typically 5 times) with a period corresponding to the frequency of the librational mode ω_ϕ. Once the angle of the iron rod is far from its initial position, the current is turned off and we observe relaxation of the mechanical oscillator through the optical measurement.

Figure 5.5.b) shows the result of such ring-down measurement under atmospheric pressure and for a small magnetic field of 10 mT. The frequency of the ring-down is obtained either by a Fourrier transforming the signal or by fitting the time trace with an exponentially decaying sinus. Here we find a frequency ω_ϕ of $2\pi \times 20.7$ kHz, already more than one order of magnitude higher than the confinement of non-magnetic micro-particles in a Paul trap.

Remarkably, we also observe small oscillations at a lower frequency (~ 250 Hz), which we identify to be a center of mass mode. Two effects can cause this excitation of a CoM mode following a ring down. First, the two coils that we use to generate the exciting magnetic field can be misaligned, therefore producing a small magnetic gradient. Secondly, it can come from coupling between the libration and the CoM. In particular, if there is a mismatch between the centroid of charges and the center of mass, large rotations around the center of mass will displace the centroid of charges. The Paul trap will therefore exert a spring force to the particle. Here this coupling is small as the frequency of the exciting magnetic field is on resonance with the librational mode, the frequency of which is two orders of magnitude higher than the confinement of the Paul trap.

5.2.3 Characterization of the mechanical properties

We now take a closer look at the mechanical properties of these levitating iron rods.

High libration frequency

Within the context of spin-mechanics, we are especially interested in increasing the frequency of the mechanical oscillator. The formula for the frequency of the librational mode of a soft ferromagnet (obtained in section 5.1.2) reads:

$$\omega_\phi = \sqrt{\frac{V(n_r - n_a)}{I_\phi \mu_0 n_a n_r}} B, \tag{5.6}$$

so the magnetic confinement is proportional to the magnetic field. As mentioned in section 5.1.2, in the case of a prolate spheroid, the magnetic confinement is also optimized for a moderate aspect ratio (2.6). Finally the factor V/I_ϕ implies that a stronger confinement is obtained for smaller particles.

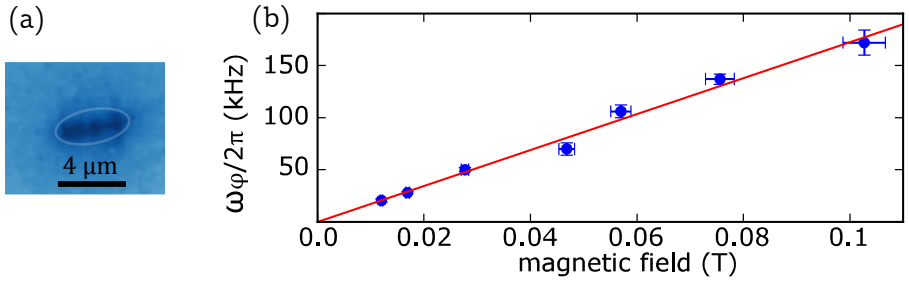

Figure 5.6: a) Image of a small elongated particle. The particle is fitted well by an ellipse of size 5.4µm×2.5µm. b) Angular frequency ω_ϕ of the libration mode of the particle as a function of the magnetic field.

Due to the inhomogeneous sizes of the iron spheres in our sample, we accomplish levitation of smaller particle by simply iterating the injection and post-selecting smaller particles. Figure 5.6.a) shows an image of such particle, we approximate its shape by a prolate spheroid and find a size of 5.4µm×2.5µm. Once such a small particle is levitated, we tune the magnetic field by bringing the permanent magnets closer to the trap. Note that for strong magnetic fields, the magnets need to be carefully aligned in a Helmholtz configuration: small deviations will produce a substantial shift of the particle in the trap due to magnetic gradients and can easily pull the particle out of the trap.

Figure 5.6.b) shows the frequency of the librational mode for this particle as a function of the magnetic field. Its is measured by fitting relaxation of the angular degree of freedom during a ring-down sequence under atmospheric pressure and the magnetic field is calibrated for each positions of the magnet using NV magnetometry. We confirm the linear dependency of the confinement with the magnetic field and for the highest field of 0.1 T we reach a frequency of $\omega_\phi = 2\pi \times (170 \pm 10)$ kHz. Calculations taking the fitted spheroidal shape yield a confinement of $\omega_\phi = 2\pi \times 240$ kHz, in reasonable agreement with the experiment given the approximate shape. Further improvement of the frequency could be reached with smaller levitated particles.

Quality factor

A levitated mechanical oscillator with a high frequency is also an attractive system because it can reach a high quality factor as the vacuum pressure is reduced. Figure 5.7 shows the result of a ring-down sequence at a vacuum pressure of 1 mbar. The reduced damping allows us to increase the quality factor to $1.3\,10^3$.

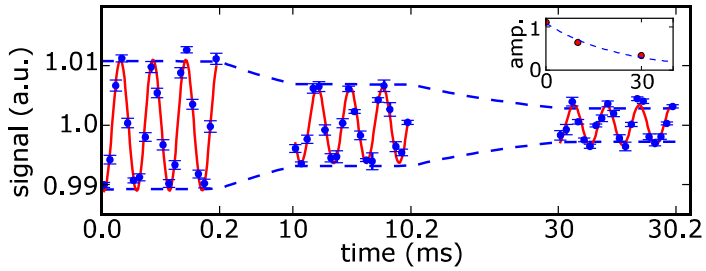

Figure 5.7: Ring-down of the librational mode of a levitated ferromagnet under a vacuum pressure of 1 mbar. Points are taken around 0, 10 and 30 ms. The inset shows the evolution of amplitude of the libration as a function of the relaxation time.

A higher quality factor will be reached at higher vacuum but further experiments are required to measure it. For now, at $\sim 10^{-1}$ mbar, we observe trap-driven rotations of the iron rods about the axis of the magnetic field, which is solely confined by the Paul trap. This instability was already observed in the case of micro-diamonds and presents a strong limitation, as discussed in section 2.5.2. In the case of a ferromagnet, they are not necessarily an issue as we are mostly interested in confinement along axes that are perpendicular to the rotation axis. In the present scheme they however blur out the speckle patterns that we use to detect the angular motion.

5.3 Hybrid diamond-ferromagnet particles

We now examine how to combine magnetic confinement together with NV spins. The most direct approach is to use hybrid particles composed of a diamond with embedded NV spins and a ferromagnetic material. Following this idea, we followed two directions: firstly we deposited nano-diamonds on iron spheres and secondly we deposited a nickel coating on micro-diamonds.

5.3.1 Nano-diamonds on iron micro-spheres

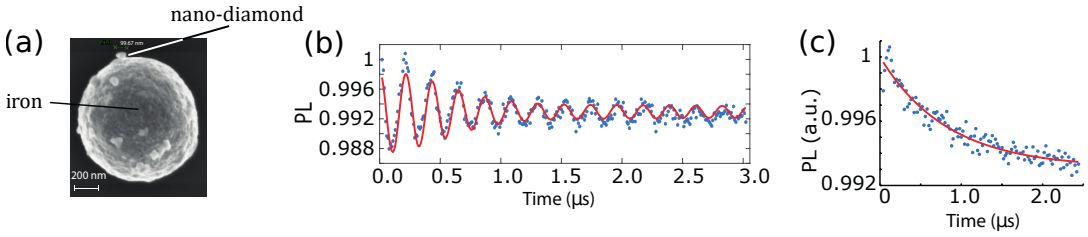

Figure 5.8: a) SEM image of a hybrid particle, with nano-diamonds on the surface of an iron sphere. b) Rabi oscillations and c) Hahn echo from NV spins embedded in a nano-diamond lying on the surface of an iron sphere levitating in a Paul trap under atmospheric pressure.

Figure 5.8.a) shows a scanning microscope image of a hybrid particle made of nano-diamonds laying on an iron micro-sphere. We use the same sample as in previous section for the iron spheres and 100 nm nano-diamonds (brFND-100 from FND biotech) which

each contains a large number of NV spins. The hybrid particle is obtained by using a nebulizer to spray a solution containing the nano-diamonds on a glass coverslip covered of iron spheres. We then follow the same injection method as before to inject the hybrid particles in the trap. Once inside the trap, even though the particles are close to isotropic, we observed that their orientation depends on the magnetic field.

This method was found to be poorly reliable for reasons we have not yet understood. Many injected particles showed a low photo-luminescence (PL) signal or a low ESR contrast compared with when they were outside the trap. Some particles however still displayed good PL and spin properties and under a moderate magnetic field and atmospheric pressure, we were able to measure well-resolved ESR lines and perform Rabi oscillations (see figure 5.8.b)) as well as spin echoes (see figure 5.8.c)) on NV spins embedded in such particles. We found coherence times in the µs range, in agreement to what is expected from these nano-diamonds.

5.3.2 Nickel coating on micro-diamonds

We made hybrid particles using a second method: we evaporated a nickel coating (∼200 nm) on top of micro-diamonds (∼ 10 µm MSY 8-12) laying on a glass coverslip. Figure 5.9.a) illustrates the resulting hybrid particles.

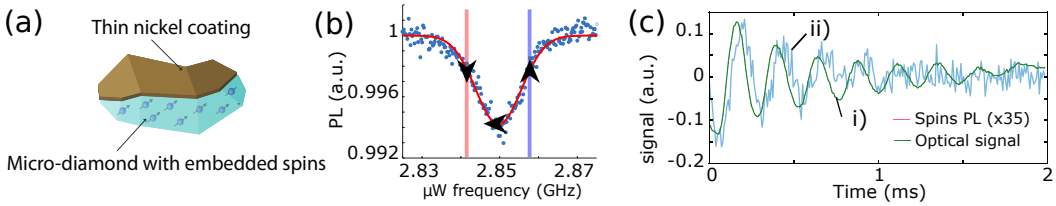

Figure 5.9: a) Illustration of the hybrid particle made of a micro-diamond with a nickel coating. b) Electron spin resonance from one class of NV centers embeded in such hybrid particle under a magnetic field. c) Libration of a hybrid particle during a ring-down sequence. Trace (i) is measured *via* the speckle patterns of the backscattered light. Trace (ii) is obtained by measuring the NV spins Photoluminescence (PL) while tuning microwaves on the two slopes of the ESR peak.

Once levitating in the trap, these particles display unaffected spin properties as well as magnetic confinement of their angular degree of freedom. Due to the small volume of magnetic material, frequencies of the librational modes are lower than for iron rods: typically a few kHz for $B \sim 100$ G.

We measure librations of these particles during a ring-down sequence where we excite the librational modes with a time-varying magnetic field as in section 5.2. Figure 5.9.c), trace (i) shows the ring-down measured using the backscattered light.

We were also able to measure this ring-down using the NV spins from the hybrid particles. To this end, we apply a microwave blue or red detuned from the magnetic resonance of a spin ensemble as depicted in the ESR of figure 5.9.b). As the particle rotates, the magnetic resonance shifts and so does the detuning thereby affecting the efficiency of the

microwave pumping. This implies that the spins population in the magnetic state and therefore the photoluminescence from the NV centers depend on the angular position of the particle. In particular, this variation has an opposite sign depending on whether the microwave is red detuned or blue detuned: for example, as depicted on the ESR from figure 5.9.b) if the frequency of the magnetic resonance decreases (horizontal black arrow), the PL decreases or increases when the microwave is red or blue detuned respectively (vertical black arrows).
In figure 5.9.c) trace (ii), we show the subtracted PL signal of two ring-down sequences where the microwave was blue and red detuned. This allows us to eliminate artefacts that would appear due to a change of the collection efficiency when the diamond rotates: here we only measure the spin-population. Both traces (i) and (ii) are accumulated during the same time but the signal originating from the NV spins is actually ~ 35 times smaller. Increasing the spins coherence would result in a sharper ESR line and could considerably improve it.

Remarkably one can observe a small delay between the NV spins' population (obtained from the PL signal) and the direct measurement of the angular position (back-scattered light). This delay originates from the finite polarization time and lifetime of the NV spins and it enables them to exert the non-conservative torque that we have used to cool down librational modes in the previous chapter.

Conclusion

In this chapter, we have shown that magnetic forces can produce a strong confinement of the angular degrees of freedom of levitating micro-magnets. We have levitated iron micro-rods in a Paul trap and observed librational frequencies up to 150 kHz, resulting from the confinement procured by the alignment of the rods with an externally applied magnetic field. At 1 mbar, we measure a quality factor for such oscillator of $\sim 10^3$, which is promising given the low vacuum conditions. We have finally levitated hybrid particles composed of both a diamond and ferromagnetic materials. These hybrid particles enabled us to combine the NV spins with an oscillator that has a higher frequency than what we attain without magnetic confinement.
The use of smaller particles, or hard ferromagnets would dramatically increase the confinement frequency; once combined with high-purity diamond, such platform has the potential to yield a spin-mechanical coupling in the resolved sideband regime.

General conclusion

At the beginning of the twentieth century, quantum mechanics arose as a theory to explain specific phenomena that contradicted classical physics. Since then, the application of these new laws in solid state physics and optics yielded tremendous advances in many technological fields. Now, even the most counter-intuitive predictions of quantum mechanics have been confirmed, and devices that were designed to test quantum mechanics are finding applications, in particular as sensors.
In an attempt to build new "quantum technologies", we are witnessing an increasing degree of control of quantum systems, which will also be beneficial to fundamental physics. For example, nitrogen vacancy (NV) spins in diamond have extensively been used as a point-like magnetometer [89] or as fluorescent markers [137, 138], but they have also been used to demonstrate the first loophole-free Bell inequality test [19]. The work of this thesis fits well in this broader context: we use the electron spins of Nitrogen Vacancy (NV) centers to control the motion of levitated diamonds, with both fundamental and more practical prospects.

During this thesis, we developed a practical platform to both levitate micro-diamonds and trap their angular degrees of freedom [74]. In order to manipulate NV spins in levitating diamonds, we integrated spin control tools to the trapping apparatus while retaining a relatively simple design with an ample margin for improvement [122]. Electron spin resonance have already been carried out in optical tweezer [62–64], but this system also allowed us to probe the coherence time of the NV spins in a levitating diamond, showing unaltered spin properties [75].
We then turned our focus to exploring the spin-mechanical coupling between the librational modes and the NV spins [73]. Such spin-mechanical coupling contrasts with more usual schemes that rely on high magnetic gradients to couple the center of mass of an oscillator to a single spin.
Here, we were able to use a large number of NV spins to apply a torque to the levitating diamond under a homogeneous magnetic field [77]. While the observation of a spin-induced force by a mechanical means is not new and was, in particular, achieved using a single spin [41], the spin properties of the NV center makes it particularly engaging for such experiments. So far, only detection of the excited [44] and thermal [45] motion of a mechanical oscillator had been achieved using single spins. Here, the long lifetime of the NV spins in a levitating diamond allowed us to exert a non-conservative torque to it, cooling down its librational modes to a final temperature of $\sim$80 K.
The main obstacle to achieving a lower temperature, and a coherent coupling, are the low frequency of our mechanical oscillator and the quality of our diamond samples.
Lastly, to overcome this limitation, we levitated iron micro-rods in a Paul trap and observed the confinement of their angular degrees of freedom when an external magnetic

field is applied, essentially realizing a micron-scale compass. Magnetic forces applied at this micron-scale allow a two orders of magnitude enhancement of the librational frequencies compared to the Paul trap librational confinement [76]. Moreover, this system can be integrated with NV spins by levitating a diamond-ferromagnet particle. This hybrid particle displays both a stronger confinement and efficient NV spin control.

The most immediate prospect of these experiments that comes to mind is the possibility to prepare a mechanical oscillator in an arbitrary quantum state using NV spins. However, this entails having a similar degree of control than trapped ion platforms, which means, in particular reaching the resolved sideband and the strong coupling regimes [43, 73]. Several improvements in the current system are required in order to do so. To begin with, the experiments should be carried out with isotopically purified CVD-grown diamonds: the NV spins coherence will be significantly enhanced in such samples. The size of the levitating diamond must also be decreased to about 100 nm to increase both the single spin coupling and the confinement of the Paul trap. Alternatively other confinement mechanisms may also be used: magnetic confinement, using a hybrid ferromagnetic-diamond particle [76] or gyroscopic stabilization using fast trap-driven rotations [116].

Reaching the sideband resolved regime with a single spin coupling stronger than the NV decoherence rate would also open up interesting perspective for quantum information and simulation. In this regime, NV spins embedded in the same levitating diamond could indeed be coupled to each other [60]. Here, the mechanical oscillator would be used as a bus, for example to mediate entanglement and perform a gate operation between two NV spins [190], in close analogy to gates protocols designed for ion traps [191].
Another intriguing possibility is to use the coupling of the NV electron spin to a nearby nuclear spin with longer coherence time [18, 20, 147]. One could envision experiments where several nuclear spins are coupled to the same mechanical oscillator *via* the NV electron spins and therefore coupled to each other.

Even out of the sideband resolved regime, a loose trap might provide opportunities as well. For example, the spin-induced torque that we have observed could be used as an efficient measurement of the spin population. In the single spin limit and with a sufficient sensitivity one could, for example perform a quantum non-destructive measurement of the spin state. In such experiment, a small particle and a deliberately loose trap maximizes the rotation induced by the torque. Similarly to magnetic-resonance force microscopy, one could also observe other defects, which possess a spin that have an intrisic asymmetry but that cannot be optically detected.
Finally it is also possible to devise matter wave interferometry experiments where the trap is turned off or softened [57, 60]: depending on the spin state the diamond would follow two different trajectories , recombined within the coherence time of NV spins.

To conclude, levitating diamonds constitutes a novel platform for experiments that aim at bridging the gap between the quantum and the classical worlds. We believe this hybrid system offers a fertile playground, giving rise to a rich physics with bright prospects in quantum information and solid-state physics.

Appendix A

Ring electrode

Ring fabrication

The ring electrodes are made from single wires bend to form the right shape. This is typically done by wrapping the wire around a bigger round wire the size of which determines the torus interior diameter. Once the shape of a loop is imprinted, the ring is held into place with a pressed caliper as described in figure 2.8-b) while the two tips of the wire are pulled toward the exterior of the ring, so they don't touch each other and allow *in fine* to hold the ring. The bigger, internal wire is retrieved either after the first branch is bent or when both are. Care is taken to let a small space between the two branches of the structure so an electrical current can be applied through the ring. Figure 2.8.a) displays a white light microscope image of a micro-ring thereby made.

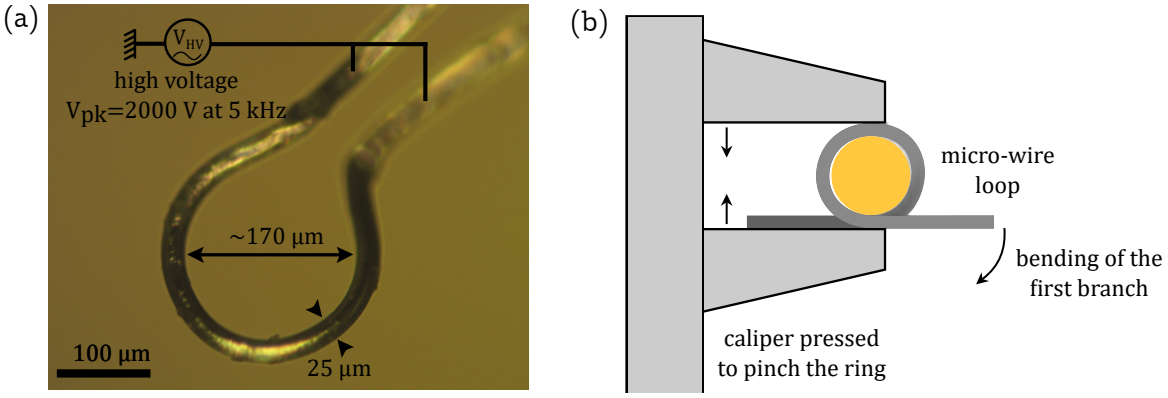

Figure A.1: a) White light microscope image of a tungsten micro-ring. b) Micro-ring fabrication procedure: bending stage when a caliper is used to maintain the torus structure while the branches are bent.

The smaller rings are made using either a 25 µm tungsten micro-wire or a 15 µm gold-coated tungsten wire. For larger ring we use copper alloy wire larger than 120 µm. Fabrication of a single functioning micro-ring takes from ten minutes to a few hours, depending on dexterity, luck and whether the caliper is for example mounted on a translation stage. Since the exact shape of the rings is quite variable, some ring allow better trapping than others, usually a few rings are made and tested before one has appropriate confinement and injection rate.

Impact of the ring experimental features

Although we did not attempt to precisely characterize the features of the electrodes which allow efficient trapping, we were able to discern several key points that impact confinement and injection rate. The empirical observations are discussed in the section below. We conclude that confinement along at least one direction is reduced if the ring is too asymmetric or the bottleneck too wide. On the other hand, the injection rate is lowered when the bottleneck is narrow compared to the size of the injected particles. When trapping in the bottleneck region, a better confinement is obtained for the center of mass when the bottleneck is narrow and the branches departing from the ring section are bent with a sharp angle. If they are not, center of mass confinement along the direction in between the two branches is lowered but the confinement of the angular degree of freedom is increased.

Note that it is possible to use two electrodes composed of two sharply bent wire in front of each other, to produce a similar trapping than in the bottleneck of a ring electrode. Because of the small size of the wire, flexibility of the two electrodes is however an issue: while using a ring firmly binds them to each other, a length of several millimeters for each electrode allows them to move away from each other when a high voltage is applied on both of them.

Rings made from micro-wires are quite fragile: they can easily be bent into another shape and typically suffer degradation of their surface, supposedly from corrosion caused by small electric arcs when particles are injected in the trap. As a result their surface appears darkened after a few weeks of use and trapping is less efficient (lower confinement or higher stray electric fields). This state can be reversed to some extend by plunging them in an acid bath (ammonia or piranha etch) but most often than not when a ring is too damaged -due to corrosion or deformation- so that trapping becomes difficult it is simply replaced by a new one.

Appendix B

Calculation of the cooling rate

To evaluate the cooling rate in presence of an optical field, we separate the spin dynamics [43, 180] by considering it to be much faster than the phonon one ($\omega_r/(2\pi), \Gamma_{\rm op} \gg \tilde{\lambda}_\phi$). The master equation for the spin degree of freedom therefore becomes

$$\dot{\hat{\rho}} = i\left[\hat{\rho}, \hat{H}\right]/\hbar + \hat{R}_{\rm op}, \tag{B.1}$$

where $\hat{R}_{\rm op}$ is the evolution caused by the optical dephasing processes. Typically, a green laser excites the ground spin states $|g\rangle$, $|d\rangle$ and $|e\rangle$ into excited electronic states $|g'\rangle$, $|d'\rangle$ and $|e'\rangle$ from where they decay to the ground states radiatively or through a metastable state $|m\rangle$. Note that since the coherence are systematically destroyed in the excited and metastable states, one needs only to treat their population without unitary evolution.

The optical term can be written:

$$\hat{R}_{\rm op} = \hat{R}_{\rm exc} + \hat{R}_{\rm rad} + \hat{R}_{\rm meta}, \tag{B.2}$$

with

$$\begin{array}{lcl} \hat{R}_{\rm exc} & = & \sum_{i=g,d,e}^{j=g',d',e'} k_{ij} D[|j\rangle\langle i|], \\ \hat{R}_{\rm rad} & = & \sum_{i=g',d',e'}^{j=g,d,e} k_{ij} D[|j\rangle\langle i|], \\ \hat{R}_{\rm meta} & = & \sum_{i=g',d',e'} k_{im} D[|m\rangle\langle i|] + \sum_{j=g,d,e} k_{mj} D[|j\rangle\langle m|], \end{array} \tag{B.3}$$

where k_{ij} is the transition rates between the i and j spin states and the Lindblad superoperator $D[\hat{c}] = \hat{c}\hat{\rho}\hat{c}^\dagger - \left(\hat{c}^\dagger\hat{c}\hat{\rho} + \hat{\rho}\hat{c}^\dagger\hat{c}\right)/2$ is used to describe the dissipative transitions between spin states. The rates k_{ij} for the mixed states $|g\rangle$, $|d\rangle$ and $|e\rangle$ depends on the magnetic field and can be calculated from the rates k^0_{ij} of the zero-field states $|0\rangle$, $|\pm1\rangle$ [143]. The optical excitation rate $\Gamma_{\rm op}$ is defined as the excitation rate of the zero-field states $k^0_{ii'} = \Gamma_{\rm op}$.

The effect of the spin lifetime and decoherence are neglected, since the considered rates are expected to be much slower than the spin dynamics. The total cooling rate is $W = W_{op} + W_{gas}$ where W_{gas} is the heating rate due to residual gas and $W_{\rm op} = S(\omega_\phi) - S(-\omega_\phi)$ is the optical cooling rate determined by the fluctuation spectrum [43]:

$$S(\omega) = 2\lambda_\phi^2 \int_0^\infty d\tau \langle \hat{S}_z(\tau)\hat{S}_z(0)\rangle e^{i\omega\tau}. \tag{B.4}$$

For a given set of parameters, we use the master equation and the quantum regression theorem to obtain the fluctuation spectrum and in turn the cooling rate. This was done numerically using Matlab. In fig. 4.14 the fluctuation spectrum is plotted under resonant

conditions for the $|e\rangle$ and $|+\rangle$ states and with a Rabi frequency larger than the microwave detuning. With such parameters, the red sideband is higher than the blue sideband showing continuous cooling (*i.e.* $W > 0$).

Contrary to [43] neither $|+\rangle$ nor $|e\rangle$ is orthogonal to $|0\rangle$ due to the spin mixing induced by the transverse magnetic field. As a result the spin polarization is less efficient: the optical excitation can change the spin states and the depopulation -and cooling- only occur if we ensure the probabilities $|\langle 0|e\rangle|$ and $|\langle 0|+\rangle|$ to be sufficiently unbalanced. This can be tuned using the magnetic field, the microwave and Rabi frequencies as well as the optical dephasing rate. A high cooling rate can be achieved for $\phi/\pi = 0.15$ and under magnetic fields above 100 mT. There is a practical limitation to accessing the area of this map however: as the magnetic field is increased, the resonance condition ($\omega_{e'} - \omega_+ = \omega_\phi$) requires a large splitting $\sqrt{\Delta^2 + \Omega_R^2}$ of the $|+\rangle$ and $|-\rangle$ states. Since it is technically challenging to increase Ω_R above the GHz range [175], one will have to increase Δ therefore limiting oneself to lower values of ψ.

Bibliography

[1] M. Planck, Annalen der Physik **309**, 553 (1901).

[2] A. Einstein, Annalen der Physik **323**, 639 (1905).

[3] A. Sommerfeld, Annalen der Physik **356**, 1 (1916).

[4] A. Einstein, B. Podolsky, and N. Rosen, Physical Review **47**, 777 (1935).

[5] T. H. Maiman, (1960).

[6] J. S. Bell, Physics Physique Fizika **1**, 195 (1964).

[7] S. J. Freedman and J. F. Clauser, Physical Review Letters **28**, 938 (1972).

[8] A. Aspect, P. Grangier, and G. Roger, Physical Review Letters **47**, 460 (1981).

[9] W. Paul, Reviews of Modern Physics **62**, 531 (1990).

[10] D. J. Wineland, R. E. Drullinger, and F. L. Walls, Physical Review Letters **40**, 1639 (1978).

[11] F. Diedrich, J. C. Bergquist, W. M. Itano, and D. J. Wineland, Physical Review Letters **62**, 403 (1989).

[12] E. L. Raab, M. Prentiss, A. Cable, S. Chu, and D. E. Pritchard, Physical Review Letters **59**, 2631 (1987).

[13] P. W. Shor, in *Proceedings 35th annual symposium on foundations of computer science* (Ieee, 1994) pp. 124–134.

[14] J. I. Cirac and P. Zoller, Physical Review Letters **74**, 4091 (1995).

[15] C. Monroe, D. M. Meekhof, B. E. King, W. M. Itano, and D. J. Wineland, Physical Review Letters **75**, 4714 (1995).

[16] T. Monz, P. Schindler, J. T. Barreiro, M. Chwalla, D. Nigg, W. A. Coish, M. Harlander, W. Hänsel, M. Hennrich, and R. Blatt, Physical Review Letters **106**, 130506 (2011).

[17] A. Morello, Nature nanotechnology **8**, 233 (2013).

[18] P. C. Maurer, G. Kucsko, C. Latta, L. Jiang, N. Y. Yao, S. D. Bennett, F. Pastawski, D. Hunger, N. Chisholm, M. Markham, D. J. Twitchen, J. I. Cirac, and M. D. Lukin, Science **336**, 1283 (2012).

[19] B. Hensen, H. Bernien, A. E. Dréau, A. Reiserer, N. Kalb, M. S. Blok, J. Ruitenberg, R. F. L. Vermeulen, R. N. Schouten, C. Abellán, W. Amaya, V. Pruneri, M. W. Mitchell, M. Markham, D. J. Twitchen, D. Elkouss, S. Wehner, T. H. Taminiau, and R. Hanson, Nature **526**, 682 (2015).

[20] C. E. Bradley, J. Randall, M. H. Abobeih, R. C. Berrevoets, M. J. Degen, M. A. Bakker, M. Markham, D. J. Twitchen, and T. H. Taminiau, arXiv:1905.02094 [cond-mat, physics:quant-ph] (2019), arXiv: 1905.02094.

[21] J. Clarke and F. K. Wilhelm, Nature **453**, 1031 (2008).

[22] L. DiCarlo, M. D. Reed, L. Sun, B. R. Johnson, J. M. Chow, J. M. Gambetta, L. Frunzio, S. M. Girvin, M. H. Devoret, and R. J. Schoelkopf, Nature **467**, 574 (2010).

[23] D. D. Awschalom, L. C. Bassett, A. S. Dzurak, E. L. Hu, and J. R. Petta, Science **339**, 1174 (2013).

[24] L. M. Vandersypen, M. Steffen, G. Breyta, C. S. Yannoni, M. H. Sherwood, and I. L. Chuang, Nature **414**, 883 (2001).

[25] C. J. Davisson and L. H. Germer, Proceedings of the National Academy of Sciences of the United States of America **14**, 317 (1928).

[26] M. Arndt, O. Nairz, J. Vos-Andreae, C. Keller, G. van der Zouw, and A. Zeilinger, Nature **401**, 680 (1999).

[27] S. Eibenberger, S. Gerlich, M. Arndt, M. Mayor, and J. Tüxen, Physical Chemistry Chemical Physics **15**, 14696 (2013).

[28] P. Rabl, S. J. Kolkowitz, F. H. L. Koppens, J. G. E. Harris, P. Zoller, and M. D. Lukin, Nature Physics **6**, 602 (2010).

[29] T. A. Palomaki, J. W. Harlow, J. D. Teufel, R. W. Simmonds, and K. W. Lehnert, Nature **495**, 210 (2013).

[30] E. Verhagen, S. Deléglise, S. Weis, A. Schliesser, and T. J. Kippenberg, Nature **482**, 63 (2012).

[31] S. Das and E. C. Vagenas, Physical Review Letters **101**, 221301 (2008).

[32] I. Pikovski, M. R. Vanner, M. Aspelmeyer, M. S. Kim, and a. Brukner, Nature Physics **8**, 393 (2012).

[33] V. B. Braginskii and A. B. Manukin, Sov. Phys. , 3 (1967).

[34] C. K. Law and J. H. Eberly, Physical review letters **76**, 1055 (1996).

[35] J. Chan, T. P. M. Alegre, A. H. Safavi-Naeini, J. T. Hill, A. Krause, S. Gröblacher, M. Aspelmeyer, and O. Painter, Nature **478**, 89 (2011).

[36] I. Marinkovic, A. Wallucks, R. Riedinger, S. Hong, M. Aspelmeyer, and S. Gröblacher, arXiv:1806.10615 [cond-mat, physics:physics, physics:quant-ph] (2018), arXiv: 1806.10615.

[37] J. D. Teufel, T. Donner, D. Li, J. W. Harlow, M. S. Allman, K. Cicak, A. J. Sirois, J. D. Whittaker, K. W. Lehnert, and R. W. Simmonds, Nature **475**, 359 (2011).

[38] C. F. Ockeloen-Korppi, E. Damskägg, J.-M. Pirkkalainen, M. Asjad, A. A. Clerk, F. Massel, M. J. Woolley, and M. A. Sillanpää, Nature **556**, 478 (2018).

[39] S. Camerer, M. Korppi, A. Jöckel, D. Hunger, T. W. Hänsch, and P. Treutlein, Physical review letters **107**, 223001 (2011).

[40] A. D. O'Connell, M. Hofheinz, M. Ansmann, R. C. Bialczak, M. Lenander, E. Lucero, M. Neeley, D. Sank, H. Wang, M. Weides, J. Wenner, J. M. Martinis, and A. N. Cleland, Nature **464**, 697 (2010).

[41] D. Rugar, R. Budakian, H. J. Mamin, and B. W. Chui, Nature **430**, 329 (2004).

[42] D. Lee, K. W. Lee, J. V. Cady, P. Ovartchaiyapong, and A. C. B. Jayich, Journal of Optics **19**, 033001 (2017).

[43] P. Rabl, P. Cappellaro, M. V. G. Dutt, L. Jiang, J. R. Maze, and M. D. Lukin, Physical Review B **79**, 041302 (2009).

[44] O. Arcizet, V. Jacques, A. Siria, P. Poncharal, P. Vincent, and S. Seidelin, Nature Physics **7**, 879 (2011).

[45] S. Kolkowitz, A. C. B. Jayich, Q. P. Unterreithmeier, S. D. Bennett, P. Rabl, J. G. E. Harris, and M. D. Lukin, Science **335**, 1603 (2012).

[46] V. Jain, J. Gieseler, C. Moritz, C. Dellago, R. Quidant, and L. Novotny, Physical Review Letters **116**, 243601 (2016).

[47] A. Ashkin, Physical Review Letters **24**, 156 (1970).

[48] R. F. Wuerker, H. Shelton, and R. V. Langmuir, Journal of Applied Physics **30**, 342 (1959).

[49] J.-F. Hsu, *COOLING THE CENTER-OF-MASS MOTION OF A DIAMOND NANOCRYSTAL IN A MAGNETO-GRAVITATIONAL TRAP*, Ph.D. thesis (2016).

[50] N. Kiesel, F. Blaser, U. Delic, D. Grass, R. Kaltenbaek, and M. Aspelmeyer, Proceedings of the National Academy of Sciences **110**, 14180 (2013).

[51] J. Gieseler, B. Deutsch, R. Quidant, and L. Novotny, Physical Review Letters **109** (2012), 10.1103/PhysRevLett.109.103603.

[52] G. P. Conangla, A. W. Schell, R. A. Rica, and R. Quidant, Nano Letters **18**, 3956 (2018).

[53] T. Li, S. Kheifets, and M. G. Raizen, Nature Physics **7**, 527 (2011).

[54] F. Tebbenjohanns, M. Frimmer, A. Militaru, V. Jain, and L. Novotny, arXiv:1812.09875 [physics] (2018), arXiv: 1812.09875.

[55] G. P. Conangla, F. Ricci, M. T. Cuairan, A. W. Schell, N. Meyer, and R. Quidant, arXiv:1901.00923 [physics] (2018), arXiv: 1901.00923.

[56] F. Tebbenjohanns, M. Frimmer, V. Jain, D. Windey, and L. Novotny, arXiv preprint arXiv:1908.05079 (2019).

[57] M. Scala, M. S. Kim, G. W. Morley, P. F. Barker, and S. Bose, Physical Review Letters **111**, 180403 (2013).

[58] Z.-q. Yin, T. Li, X. Zhang, and L. M. Duan, Physical Review A **88**, 033614 (2013).

[59] Z. Yin, N. Zhao, and T. Li, Science China Physics, Mechanics & Astronomy **58**, 1 (2015).

[60] Y. Ma, T. M. Hoang, M. Gong, T. Li, and Z.-q. Yin, Physical Review A **96**, 023827 (2017).

[61] L. Ge and N. Zhao, Physical Review A **98**, 043415 (2018).

[62] V. R. Horowitz, B. J. Alemán, D. J. Christle, A. N. Cleland, and D. D. Awschalom, Proceedings of the National Academy of Sciences **109**, 13493 (2012).

[63] L. P. Neukirch, J. Gieseler, R. Quidant, L. Novotny, and A. N. Vamivakas, Optics Letters **38**, 2976 (2013).

[64] T. M. Hoang, J. Ahn, J. Bang, and T. Li, Nature Communications **7**, 12250 (2016).

[65] A. Kuhlicke, A. W. Schell, J. Zoll, and O. Benson, Applied Physics Letters **105**, 073101 (2014).

[66] L. P. Neukirch, E. von Haartman, J. M. Rosenholm, and A. Nick Vamivakas, Nature Photonics **9**, 653 (2015).

[67] A. T. M. A. Rahman, A. C. Frangeskou, M. S. Kim, S. Bose, G. W. Morley, and P. F. Barker, Scientific Reports **6**, 21633 (2016).

[68] B. E. Kane, Physical Review B **82**, 115441 (2010).

[69] S. Kuhn, P. Asenbaum, A. Kosloff, M. Sclafani, B. A. Stickler, S. Nimmrichter, K. Hornberger, O. Cheshnovsky, F. Patolsky, and M. Arndt, Nano letters **15**, 5604 (2015).

[70] T. M. Hoang, Y. Ma, J. Ahn, J. Bang, F. Robicheaux, Z.-Q. Yin, and T. Li, Physical Review Letters **117**, 123604 (2016).

[71] B. A. Stickler, S. Nimmrichter, L. Martinetz, S. Kuhn, M. Arndt, and K. Hornberger, Physical Review A **94**, 033818 (2016).

[72] S. Kuhn, A. Kosloff, B. A. Stickler, F. Patolsky, K. Hornberger, M. Arndt, and J. Millen, Optica **4**, 356 (2017).

[73] T. Delord, L. Nicolas, Y. Chassagneux, and G. Hétet, Physical Review A **96**, 063810 (2017).

[74] T. Delord, L. Nicolas, L. Schwab, and G. Hétet, New Journal of Physics **19**, 033031 (2017).

[75] T. Delord, P. Huillery, L. Schwab, L. Nicolas, L. Lecordier, and G. Hétet, Physical Review Letters **121**, 053602 (2018).

[76] P. Huillery, T. Delord, L. Nicolas, M. V. D. Bossche, M. Perdriat, and G. Hétet, arXiv:1903.09699 [quant-ph] (2019), arXiv: 1903.09699.

[77] T. Delord, P. Huillery, L. Nicolas, and G. Hétet, arXiv:1905.11509 [cond-mat, physics:quant-ph] (2019), arXiv: 1905.11509.

[78] A. Einstein and W. J. d. Haas, , 17 (1915).

[79] S. J. Barnett, Physical Review **6**, 239 (1915).

[80] W. Gerlach and O. Stern, Zeitschrift für Physik **9**, 349 (1922).

[81] R. A. Millikan, Physical Review **4**, 73 (1914).

[82] J. Fraunhofer, Annalen der Physik **56**, 264 (1817).

[83] I. I. Rabi, J. R. Zacharias, S. Millman, and P. Kusch, Physical Review **53**, 318 (1938).

[84] I. I. Rabi, Physical Review **51**, 652 (1937).

[85] F. Bloch, W. W. Hansen, and M. Packard, Physical Review **70**, 474 (1946).

[86] E. L. Hahn, Physical Review **80**, 580 (1950).

[87] J. Brossel, S. Geschwind, and A. L. Schawlow, Physical Review Letters **3**, 548 (1959).

[88] J. Wrachtrup, C. v. Borczyskowski, J. Bernard, M. Orrit, and R. Brown, Nature **363**, 244 (1993).

[89] S. Hong, M. S. Grinolds, L. M. Pham, D. Le Sage, L. Luan, R. L. Walsworth, and A. Yacoby, MRS Bulletin **38**, 155 (2013).

[90] A. Gruber, A. Dräbenstedt, C. Tietz, L. Fleury, J. Wrachtrup, and C. v. Borczyskowski, Science **276**, 2012 (1997).

[91] J.-P. Tetienne, T. Hingant, J.-V. Kim, L. H. Diez, J.-P. Adam, K. Garcia, J.-F. Roch, S. Rohart, A. Thiaville, D. Ravelosona, and V. Jacques, Science **344**, 1366 (2014).

[92] M. S. Grinolds, M. Warner, K. De Greve, Y. Dovzhenko, L. Thiel, R. L. Walsworth, S. Hong, P. Maletinsky, and A. Yacoby, Nature Nanotechnology **9**, 279 (2014).

[93] D. F. Evans, Philosophical Magazine **1**, 370 (1956).

[94] O. Züger and D. Rugar, Applied Physics Letters **63**, 2496 (1993).

[95] S.-h. Chao, W. M. Dougherty, J. L. Garbini, and J. A. Sidles, Review of Scientific Instruments **75**, 1175 (2004).

[96] B. Diu, F. Laloe, and C. Cohen-Tannoudji, *Mécanique quantique -: Fermions, bosons, photons, corrélations et intrication* (EDP sciences, 2019) google-Books-ID: Cm2kDwAAQBAJ.

[97] W. Neuhauser, M. Hohenstatt, P. E. Toschek, and H. Dehmelt, Physical Review A **22**, 1137 (1980).

[98] D. Leibfried, R. Blatt, C. Monroe, and D. Wineland, Reviews of Modern Physics **75**, 281 (2003).

[99] F. Mintert and C. Wunderlich, Physical Review Letters **87**, 257904 (2001).

[100] A. Khromova, C. Piltz, B. Scharfenberger, T. F. Gloger, M. Johanning, A. F. Varón, and C. Wunderlich, Physical Review Letters **108**, 220502 (2012).

[101] B. E. King, C. S. Wood, C. J. Myatt, Q. A. Turchette, D. Leibfried, W. M. Itano, C. Monroe, and D. J. Wineland, Physical Review Letters **81**, 1525 (1998).

[102] Q. A. Turchette, C. S. Wood, B. E. King, C. J. Myatt, D. Leibfried, W. M. Itano, C. Monroe, and D. J. Wineland, Physical Review Letters **81**, 3631 (1998).

[103] J. Teissier, A. Barfuss, P. Appel, E. Neu, and P. Maletinsky, Physical Review Letters **113**, 020503 (2014).

[104] A. Barfuss, J. Teissier, E. Neu, A. Nunnenkamp, and P. Maletinsky, Nature Physics **11**, 820 (2015).

[105] S. Hong, M. S. Grinolds, P. Maletinsky, R. L. Walsworth, M. D. Lukin, and A. Yacoby, Nano Letters **12**, 3920 (2012).

[106] A. C. Frangeskou, A. T. M. A. Rahman, L. Gines, S. Mandal, O. A. Williams, P. F. Barker, and G. W. Morley, New Journal of Physics **20**, 043016 (2018).

[107] E. Hebestreit, R. Reimann, M. Frimmer, and L. Novotny, Physical Review A **97** (2018), 10.1103/PhysRevA.97.043803, arXiv: 1801.01164.

[108] D. V. Seletskiy, S. D. Melgaard, R. I. Epstein, A. D. Lieto, M. Tonelli, and M. Sheik-Bahae, Optics Express **19**, 18229 (2011).

[109] S. D. Melgaard, A. R. Albrecht, M. P. Hehlen, and M. Sheik-Bahae, Scientific Reports **6**, 20380 (2016).

[110] A. T. M. A. Rahman and P. F. Barker, Nature Photonics **11**, 634 (2017).

[111] N. Yu and W. Nagourney, Journal of Applied Physics **77**, 3623 (1995).

[112] R. Maiwald, D. Leibfried, J. Britton, J. C. Bergquist, G. Leuchs, and D. J. Wineland, Nature Physics **5**, 551 (2009).

[113] S. Seidelin, J. Chiaverini, R. Reichle, J. J. Bollinger, D. Leibfried, J. Britton, J. H. Wesenberg, R. B. Blakestad, R. J. Epstein, D. B. Hume, W. M. Itano, J. D. Jost, C. Langer, R. Ozeri, N. Shiga, and D. J. Wineland, Physical Review Letters **96**, 253003 (2006).

[114] T. Hasegawa and K. Uehara, Applied Physics B **61**, 159 (1995).

[115] F. G. Major, G. Werth, and V. N. Gheorghe, *Charged particle traps: physics and techniques of charged particle field confinement* (2005).

[116] Maxime Perdriat, T. Delord, P. Huillery, and G. Hétet, arxiv, to be submitted (2019).

[117] Q. A. Turchette, Kielpinski, B. E. King, D. Leibfried, D. M. Meekhof, C. J. Myatt, M. A. Rowe, C. A. Sackett, C. S. Wood, W. M. Itano, C. Monroe, and D. J. Wineland, Physical Review A **61**, 063418 (2000).

[118] J. B. Fenn, M. Mann, C. K. Meng, S. F. Wong, and C. M. Whitehouse, Mass Spectrometry Reviews **9**, 37 (1990).

[119] A. Ashkin and J. M. Dziedzic, Physical Review Letters **36**, 267 (1976).

[120] M. Frimmer, K. Luszcz, S. Ferreiro, V. Jain, E. Hebestreit, and L. Novotny, Physical Review A **95**, 061801 (2017).

[121] S. Schlemmer, J. Illemann, S. Wellert, and D. Gerlich, Journal of Applied Physics **90**, 5410 (2001).

[122] T. Delord, L. Nicolas, M. Bodini, and G. Hétet, Applied Physics Letters **111**, 013101 (2017).

[123] D. S. Bykov, P. Mestres, L. Dania, L. Schmöger, and T. E. Northup, arXiv:1905.04204 [physics] (2019), arXiv: 1905.04204.

[124] "Paschen's law," (2019).

[125] A. F. Izmailov, S. Arnold, S. Holler, and A. S. Myerson, Physical Review E **52**, 1325 (1995).

[126] V. Steixner, P. Rabl, and P. Zoller, Physical Review A **72**, 043826 (2005).

[127] Y. Roichman, B. Sun, A. Stolarski, and D. G. Grier, Physical Review Letters **101**, 128301 (2008).

[128] P. Wu, R. Huang, C. Tischer, A. Jonas, and E.-L. Florin, Physical Review Letters **103**, 108101 (2009).

[129] T. Li, in *Fundamental Tests of Physics with Optically Trapped Microspheres*, Springer Theses, edited by T. Li (Springer New York, New York, NY, 2013) pp. 81–110.

[130] S. Kuhn, B. A. Stickler, A. Kosloff, F. Patolsky, K. Hornberger, M. Arndt, and J. Millen, Nature Communications **8**, 1 (2017).

[131] A. M. Zaitsev, *Optical properties of diamond: a data handbook* (Springer Science & Business Media, 2013).

[132] J. R. Maze, A. Gali, E. Togan, Y. Chu, A. Trifonov, E. Kaxiras, and M. D. Lukin, New Journal of Physics **13**, 025025 (2011).

[133] M. W. Doherty, F. Dolde, H. Fedder, F. Jelezko, J. Wrachtrup, N. B. Manson, and L. C. L. Hollenberg, Physical Review B **85**, 205203 (2012).

[134] P. Siyushev, H. Pinto, M. Vörös, A. Gali, F. Jelezko, and J. Wrachtrup, Physical Review Letters **110**, 167402 (2013).

[135] Y. Mita, Physical Review B **53**, 11360 (1996).

[136] L. Robledo, L. Childress, H. Bernien, B. Hensen, P. F. A. Alkemade, and R. Hanson, Nature **477**, 574 (2011).

[137] S. Haziza, N. Mohan, Y. Loe-Mie, A.-M. Lepagnol-Bestel, S. Massou, M.-P. Adam, X. L. Le, J. Viard, C. Plancon, R. Daudin, P. Koebel, E. Dorard, C. Rose, F.-J. Hsieh, C.-C. Wu, B. Potier, Y. Herault, C. Sala, A. Corvin, B. Allinquant, H.-C. Chang, F. Treussart, and M. Simonneau, Nature Nanotechnology **12**, 322 (2017).

[138] G. Balasubramanian, A. Lazariev, S. R. Arumugam, and D.-w. Duan, Current Opinion in Chemical Biology Molecular imaging, **20**, 69 (2014).

[139] A. Batalov, V. Jacques, F. Kaiser, P. Siyushev, P. Neumann, L. J. Rogers, R. L. McMurtrie, N. B. Manson, F. Jelezko, and J. Wrachtrup, Physical Review Letters **102**, 195506 (2009).

[140] K.-M. C. Fu, C. Santori, P. E. Barclay, L. J. Rogers, N. B. Manson, and R. G. Beausoleil, Physical Review Letters **103**, 256404 (2009).

[141] V. M. Acosta, A. Jarmola, E. Bauch, and D. Budker, Physical Review B **82**, 201202 (2010).

[142] L. Robledo, H. Bernien, T. v. d. Sar, and R. Hanson, New Journal of Physics **13**, 025013 (2011).

[143] J.-P. Tetienne, L. Rondin, P. Spinicelli, M. Chipaux, T. Debuisschert, J.-F. Roch, and V. Jacques, New Journal of Physics **14**, 103033 (2012).

[144] L. J. Rogers, S. Armstrong, M. J. Sellars, and N. B. Manson, New Journal of Physics **10**, 103024 (2008).

[145] P. Neumann, R. Kolesov, V. Jacques, J. Beck, J. Tisler, A. Batalov, L. Rogers, N. B. Manson, G. Balasubramanian, F. Jelezko, and J. Wrachtrup, New Journal of Physics **11**, 013017 (2009).

[146] A. Dréau, J.-R. Maze, M. Lesik, J.-F. Roch, and V. Jacques, Physical Review B **85**, 134107 (2012).

[147] A. Dréau, *Spins individuels dans le diamant pour l'information quantique*, phdthesis, École normale supérieure de Cachan - ENS Cachan (2013).

[148] B. Smeltzer, J. McIntyre, and L. Childress, Physical Review A **80**, 050302 (2009).

[149] S. Felton, A. M. Edmonds, M. E. Newton, P. M. Martineau, D. Fisher, D. J. Twitchen, and J. M. Baker, Physical Review B **79**, 075203 (2009).

[150] A. Jarmola, V. M. Acosta, K. Jensen, S. Chemerisov, and D. Budker, Physical Review Letters **108**, 197601 (2012).

[151] J.-P. Tetienne, T. Hingant, L. Rondin, A. Cavaillès, L. Mayer, G. Dantelle, T. Gacoin, J. Wrachtrup, J.-F. Roch, and V. Jacques, Physical Review B **87**, 235436 (2013).

[152] E. I. Baibekov, JETP Letters **93**, 292 (2011).

[153] V. V. Dobrovitski, A. E. Feiguin, R. Hanson, and D. D. Awschalom, Physical Review Letters **102** (2009), 10.1103/PhysRevLett.102.237601.

[154] V. V. Dobrovitski, A. E. Feiguin, D. D. Awschalom, and R. Hanson, Physical Review B **77** (2008), 10.1103/PhysRevB.77.245212.

[155] S. Meiboom and D. Gill, Review of Scientific Instruments **29**, 688 (1958).

[156] N. Bar-Gill, L. M. Pham, A. Jarmola, D. Budker, and R. L. Walsworth, Nature Communications **4**, 1743 (2013).

[157] E. D. Ostroff and J. S. Waugh, Physical Review Letters **16**, 1097 (1966).

[158] G. de Lange, Z. H. Wang, D. Riste, V. V. Dobrovitski, and R. Hanson, Science **330**, 60 (2010).

[159] P. C. Humphreys, N. Kalb, J. P. J. Morits, R. N. Schouten, R. F. L. Vermeulen, D. J. Twitchen, M. Markham, and R. Hanson, Nature **558**, 268 (2018).

[160] D. V. Seletskiy, S. D. Melgaard, S. Bigotta, A. Di Lieto, M. Tonelli, and M. Sheik-Bahae, Nature Photonics **4**, 161 (2010).

[161] N. Mizuochi, P. Neumann, F. Rempp, J. Beck, V. Jacques, P. Siyushev, K. Nakamura, D. J. Twitchen, H. Watanabe, S. Yamasaki, F. Jelezko, and J. Wrachtrup, Physical Review B **80**, 041201 (2009).

[162] J. R. Maze, J. M. Taylor, and M. D. Lukin, Physical Review B **78**, 094303 (2008).

[163] G. Balasubramanian, P. Neumann, D. Twitchen, M. Markham, R. Kolesov, N. Mizuochi, J. Isoya, J. Achard, J. Beck, J. Tissler, V. Jacques, P. R. Hemmer, F. Jelezko, and J. Wrachtrup, Nature Materials **8**, 383 (2009).

[164] T. Rosskopf, A. Dussaux, K. Ohashi, M. Loretz, R. Schirhagl, H. Watanabe, S. Shikata, K. Itoh, and C. Degen, Physical Review Letters **112**, 147602 (2014).

[165] K. Ohno, F. Joseph Heremans, L. C. Bassett, B. A. Myers, D. M. Toyli, A. C. Bleszynski Jayich, C. J. Palmstrøm, and D. D. Awschalom, Applied Physics Letters **101**, 082413 (2012).

[166] D. Bluvstein, Z. Zhang, C. A. McLellan, N. R. Williams, and A. C. B. Jayich, arXiv:1905.06405 [cond-mat, physics:quant-ph] (2019), arXiv: 1905.06405.

[167] M. E. Trusheim, L. Li, A. Laraoui, E. H. Chen, H. Bakhru, T. Schröder, O. Gaathon, C. A. Meriles, and D. Englund, Nano Letters **14**, 32 (2014).

[168] A. M. Edmonds, U. F. S. D'Haenens-Johansson, R. J. Cruddace, M. E. Newton, K.-M. Fu, C. Santori, R. G. Beausoleil, D. J. Twitchen, and M. L. Markham, Physical Review B **86**, 035201 (2012).

[169] J. M. Smith, S. A. Meynell, A. C. B. Jayich, and J. Meijer, Nanophotonics **8**, 1889 (2019).

[170] V. M. Acosta, E. Bauch, M. P. Ledbetter, A. Waxman, L.-S. Bouchard, and D. Budker, Physical Review Letters **104**, 070801 (2010).

[171] D. M. Toyli, D. J. Christle, A. Alkauskas, B. B. Buckley, C. G. Van de Walle, and D. D. Awschalom, Physical Review X **2**, 031001 (2012).

[172] M. Aspelmeyer, T. J. Kippenberg, and F. Marquardt, Reviews of Modern Physics **86**, 1391 (2014).

[173] K. Vahala, M. Herrmann, S. Knünz, V. Batteiger, G. Saathoff, T. W. Hänsch, and T. Udem, Nature Physics **5**, 682 (2009).

[174] R. M. Pettit, W. Ge, P. Kumar, D. R. Luntz-Martin, J. T. Schultz, L. P. Neukirch, M. Bhattacharya, and A. N. Vamivakas, Nature Photonics **13**, 402 (2019).

[175] G. D. Fuchs, V. V. Dobrovitski, D. M. Toyli, F. J. Heremans, and D. D. Awschalom, Science **326**, 1520 (2009).

[176] B. A. Stickler, B. Papendell, and K. Hornberger, Physical Review A **94**, 033828 (2016).

[177] C. Zhong and F. Robicheaux, Physical Review A **94**, 052109 (2016).

[178] B. A. Stickler, B. Schrinski, and K. Hornberger, Physical Review Letters **121**, 040401 (2018).

[179] J. Fremerey, Vacuum **32**, 685 (1982).

[180] J. I. Cirac, R. Blatt, P. Zoller, and W. D. Phillips, Physical Review A **46**, 2668 (1992).

[181] M. D. Simon and A. K. Geim, Journal of Applied Physics **87**, 6200 (2000).

[182] C. Pigot, *La lévitation Diamagnétique à l'Echelle Micrométrique: Applications et Possibilités*, Ph.D. thesis (2009).

[183] M. C. O'Brien, S. Dunn, J. E. Downes, and J. Twamley, Applied Physics Letters **114**, 053103 (2019).

[184] J.-F. Hsu, P. Ji, C. W. Lewandowski, and B. D'Urso, Scientific Reports **6**, 30125 (2016).

[185] B. R. Slezak, C. W. Lewandowski, J.-F. Hsu, and B. D'Urso, New Journal of Physics **20**, 063028 (2018).

[186] T. Wang, S. Lourette, S. R. O'Kelley, M. Kayci, Y. Band, D. F. J. Kimball, A. O. Sushkov, and D. Budker, Physical Review Applied **11**, 044041 (2019).

[187] J. J. Abbott, O. Ergeneman, M. P. Kummer, A. M. Hirt, and B. J. Nelson, IEEE Transactions on Robotics **23**, 1247 (2007).

[188] J. A. Osborn, Physical Review **67**, 351 (1945).

[189] D. J. Wineland, J. C. Bergquist, W. M. Itano, J. J. Bollinger, and C. H. Manney, Physical Review Letters **59**, 2935 (1987).

[190] X.-Y. Chen and Z.-q. Yin, Physical Review A **99**, 022319 (2019).

[191] K. Mølmer and A. Sørensen, Physical Review Letters **82**, 1835 (1999).

RÉSUMÉ

Inspirée des expériences d'atomes froids ou d'ions piégés, l'opto-mécanique a réalisé d'importants progrès vers des expériences de mécanique quantique avec un oscillateur mécanique macroscopique. Une autre approche prometteuse est l'utilisation de systèmes hybrides ou le couplage entre un atome et un oscillateur mécanique permet le contrôle cohérent de ce dernier. Dans ce travail, les modes de librations (oscillation angulaire) de micro-diamants en lévitation constituent l'oscillateur mécanique. Celui-ci est couplé *via* un champ magnétique aux spins de centres azote-lacune (NV) contenus dans le micro-diamant. Ce couplage permet alors le refroidissement du mouvement du micro-diamant, similairement au refroidissement Doppler d'ions ou d'atomes piégés.
La lévitation est réalisée à l'aide d'un piège de Paul qui confine le centre de masse mais également les degrés de liberté angulaires d'un micro-diamant chargé. Lors des premières expériences, nous utilisons les centres NV pour démontrer la stabilité angulaire et montrons que leurs propriétés de spin (cohérence, temps de vie) ne sont pas affectées par le piège. Nous faisons ensuite léviter des diamants hautement dopés contenant un grand nombre de centres NV et utilisons leur spin pour exercer un couple sur le micro-diamant en lévitation. L'observation de ce couple ouvre de nombreuses perspectives telles que le contrôle de l'oscillateur mécanique dans le régime quantique, le couplage spin-spin et dans la limite du spin unique, la mesure non-destructive d'un spin NV à température ambiante. Ici l'application la plus directe de cet effet est l'utilisation de ces ensembles de spins pour exercer une rétroaction non-conservative sur le mouvement angulaire du diamant. Cela résulte en un refroidissement ou une amplification du mode de libration du diamant.
La principale limitation de ce système est la faiblesse des fréquences de l'oscillateur mécanique comparées au taux de décohérence des spins des centres NV. Pour résoudre ce problème, nous utilisons des particules ferromagnétiques ainsi que des particules composites ferromagnétique-diamant en lévitation. Nous montrons que le moment magnétique de ces particules peut être utilisé pour augmenter le confinement angulaire de deux ordres de grandeur, plaçant ainsi les fréquences de l'oscillateur mécanique au-delà des taux de décohérences typiques de centres NV dans des diamants ultra-pures.

MOTS CLÉS

Diamant, lévitation, spin, centre NV, piège de Paul, spin-mécanique.

ABSTRACT

Inspired by experiments on cold atoms and ions, the field optomechanics has made major steps towards realizing quantum mechanical experiments with macroscopic mechanical oscillators. Hybrid systems such as the spin of Nitrogen Vacancy (NV) centers coupled to a mechanical oscillator levitating under vacuum offer another promising approach. In this work, we levitate microdiamonds with ensembles of embedded NV spins and explore effects related to the coupling between the NV spins and the libration (angular oscillations) of the micro-diamonds.
Levitation is carried out by a Paul trap, which confines both the center of mass and angular degrees of freedom of a charged micro-diamond. In a first set of experiments, we demonstrate angular stability using NV spins and perform spin echoes with levitating diamonds, showing no detectable impact of the trapping mechanism on the NV spin coherence and lifetime. We then use highly doped diamonds with large NV spin ensembles to exert a spin-dependent torque on a levitating micro-diamond. The observation of an NV spin-induced torque on a mechanical oscillator offers many prospects, such as controlling the mechanical oscillator in the quantum regime, spin-spin coupling or room temperature quantum non-destructive read-out, in the single spin limit. Here the most direct application is the use of these ensembles to apply a non-conservative back-action on the angular motion of the diamond. This results in cooling or amplification of the librational modes of the diamond.
The main limitation of the current system is the low mechanical frequencies compared to the NV spin decoherence rate. To leverage this issue we levitate both ferromagnetic and composite ferromagnetic-diamond particles. We show one can use the magnetic moment of these particles to gain two order of magnitude in confinement for the angular degree of freedom, putting the mechanical frequencies higher than NV spin decoherence rates in high-purity diamond samples.

KEYWORDS

Diamond, levitation, spin, NV center, Paul trap, spin-mechanics.